# Conceptual Design of Hydrogen Fuel Cell Aircraft

## Flying on hydrogen for a more sustainable future

by

G. L. M. Vonhoff

to obtain the degree of Master of Science
at the Delft University of Technology,
to be defended publicly on Tuesday February 25, 2021 at 1:30 PM.

| | | |
|---|---|---|
| Student number: | 4351207 | |
| Project duration: | May 15, 2020 – February 25, 2021 | |
| Thesis committee: | Prof. Dr. Ir. L. L. M. Veldhuis, | TU Delft, Chair |
| | Dr. F. Oliviero, | TU Delft, Supervisor |
| | Ir. R. C. van Benthem, | NLR, Supervisor |
| | Ir. P. C. Roling, | TU Delft, Examiner |

An electronic version of this thesis is available at http://repository.tudelft.nl/.

TU Delft

# Abstract

The demand for air travel is increasing as more people gain access to commercial aviation. As the current generation of aircraft makes use of fossil fuel combustion, this growth results in an increase in the global emissions. This is at odds with the worldwide efforts of reducing the adverse effects of climate change. Therefore, advanced propulsion systems must be developed to limit the emissions caused by the commercial aerospace industry. Using hydrogen fuel cells for propulsion is a promising technology to potentially get the sector to zero emissions. It is of interest to explore the capabilities and feasibility of aircraft with a hydrogen fuel cell powertrain. To determine the feasibility for a wide range of aircraft, a general design methodology is required.

Current research efforts focus on component level performance, however system level design research, while present, didn't introduce a general methodology. The most pressing challenge was found to be related to the system level design of a CS-23 category hydrogen fuel cell aircraft. The CS-23 category aircraft class has been identified as the most suitable focus for research efforts, due to the lower technical and certification requirements placed on the components to reach a feasible design. A general methodology for the design of CS-23 category aircraft was therefore found to be a useful contribution to the state of the art. This additionally provides a deeper understanding into the most important parameters of the power and propulsion systems design.

In this report, a general methodology for the conceptual design of hydrogen fuel cell powered CS-23 category aircraft is presented. The methodology makes use of a modified class 1 weight estimation for initial sizing according to customer requirements and component technology levels. The generated aircraft is refined using further aerodynamic analysis, which results in a feasible aircraft concept, as well as component level specifications for important aircraft components.

The methodology is implemented in a software tool, HAPPIE (Hydrogen Aircraft Power & Propulsion Initial Estimator), which allows for rapid sizing of different hydrogen fuel cell concepts. This makes the methodology accessible, and additionally provides feedback on the effects of individual design choices and technology levels on system level performance. SUAVE is used to perform the refined aerodynamic analysis.

The methodology is validated using existing conventionally powered aircraft, by comparing the sizing results from the methodology with publicly available data. The methodology's ability to analyse conventional as well as hydrogen fuel cell powertrains, furthermore allows for performance comparison between current and future technologies.

The results of the sizing methodology demonstrate the viability of hydrogen fuel cell aircraft in the CS-23 category. A conceptual design is generated, which serves as a baseline for the sensitivity analyses. It is found that hydrogen fuel cell aircraft are generally heavier than conventional aircraft, using current technology levels. Liquid hydrogen is identified as the best hydrogen storage method. Compressed hydrogen storage is also possible, however this results in a heavier aircraft with limited range. The current methodology does not predict thermal behaviour to have a significant effect on the mass of the aircraft. A component sensitivity analysis determined that the fuel cell efficiency, fuel cell specific power and hydrogen storage efficiency are the most important parameters. The ideal cruising altitude for fuel cell aircraft is at an intermediate altitude, due to the fact that the fuel cell powertrain performance decreases at increasing altitude, which balances with the lower drag in lower density air.

The research demonstrates that hydrogen powered CS-23 aircraft are viable for current technology levels, and are a suitable way in reducing carbon emissions in this category.

# Acknowledgements

The thesis is the last step in my TU Delft career as a student. I feel I can look back on a very interesting and educational time. Not only through studying and academia, but also important life lessons and meeting lifelong friends. To mark this final milestone, I would like to thank several people who made a difference to me during my thesis.

First of all I would like to thank Roel van Benthem for his support throughout my internship and graduation project at NLR. It was very interesting to be able to participate in NLR's activities in the field of hydrogen in aviation, first as an intern working alongside active groundbreaking projects, and later as a graduate student. Thank you for providing the tools and knowledge to research this highly dynamic and interesting field.

Furthermore, I would like to thank Fabrizio Oliviero, who was also instrumental as my supervisor from the TU Delft. Thank you for your fruitful discussions during the entire thesis process, providing useful feedback to take into the next stages. Having discussions on the coding and thesis was extremely insightful, especially in this corona time when normal in-person contact at TU Delft was not possible.

To that end I would also like to thank both NLR and TU Delft for the opportunity of working together during this project, and reaching a goal higher than would have been possible with only one of them. I had the chance to talk to experts from both TU Delft and NLR on the subject of aircraft design. Roelof Vos, Edwin Bloem, Wim Lammen and Jos Vankan were all inspiring conversation partners from whom I was able to determine useful implementations for the methodology.

Finally I would like to thank my friends and family for their enduring support and love, which motivated me throughout this unusual period. In particular Alex and Turhan, for the entertaining Discord and Zoom sessions.

And of course my girlfriend Susana, who kept me sane and provided endless support and motivation. I'm sure she is now an expert on this topic as a result of listening to me practicing my presentation.

This past year has been a wild ride, but so much fun and now I look forward to the next step in my career!

*G.L.M. Vonhoff*
*Delft, February 2021*

# Contents

# List of Figures

# List of Tables

# Nomenclature

| | | |
|---|---|---|
| **Latin Symbols** | | |
| $\dot{m}$ | Mass flow | $[kg/s]$ |
| $C_D$ | Drag coefficient | $[-]$ |
| $C_L$ | Lift coefficient | $[-]$ |
| b | Span | $[m]$ |
| C | Chord | $[m]$ |
| C | Coefficient | $[m]$ |
| D | Diameter | $[m]$ |
| d | Diameter | $[m]$ |
| E | Energy | $[J]$ |
| g | Gravitational constant | $[m/s^2]$ |
| HFC | Hydrogen Fuel Cell | |
| k | Lift-induced drag constant | $[-]$ |
| l | Length | $[m]$ |
| L/D | Lift to Drag ratio | |
| N | Number | [-] |
| n | Load factor | [-] |
| P | Power | $[W]$ |
| P | Pressure | $[Pa]$ |
| P/W | Power to Weight | $[W/m^2]$ |
| PR | Pressure Ratio | $[-]$ |
| R | Range | $[km]$ |
| S | Takeoff distance | $[m]$ |
| S | Wing area | $[m^2]$ |
| T | Temperature | $[C]$ |
| T | Thrust | $[N]$ |
| t | Time | $[s]$ |
| U | Voltage | $[V]$ |
| V | Velocity | $[m/s]$ |
| V | Volume | $[m^3]$ |
| W | Weight | $[N]$ |
| W/S | Wing loading | $[N/m^2]$ |
| **Greek Symbols** | | |
| $\eta$ | Efficiency | [-] |
| $\gamma$ | Ratio of specific heats | [-] |
| $\hat{\rho}$ | Specific power | $[W/kg]$ |
| $\Lambda$ | Sweep | [-] |
| $\lambda$ | Stoichiometric Ratio | [-] |
| $\lambda$ | Taper Ratio | [-] |
| $\mu$ | Ground friction constant | [-] |
| $\rho$ | Density | $[kg/m^3]$ |
| **Subscripts** | | |
| $C/4$ | Quarter chord | |

| | |
|---|---|
| air | Air |
| airfield | Airfield |
| alt | Altitude |
| ceiling | Ceiling |
| climb | Climb |
| comp | Compressor |
| cooling | Cooling |
| cooling,system | Cooling System |
| coolthrust | Cooling thrust |
| crew | Crew |
| cruise | Cruise |
| D | Drag |
| electric | Electric |
| extra | Extra |
| FC | Fuel Cell |
| frac | Fraction |
| FS | Fuselage Structure |
| fuel | Fuel |
| fus | Fuselage |
| fuselage | Fuselage |
| G | Ground run |
| heat,rejected | Heat Rejected |
| HT | Horizontal Tail |
| kerosene | Kerosene |
| L | Lift |
| LHV | Lower Heating Value |
| max | Maximum |
| max,alt | Maximum Altitude |
| min | Minimum |
| misc | miscellaneous |
| motor | Electric Motor |
| net | Net |
| nose | Nose |
| oper | Operating |
| oversize | Oversize |
| pass | Passengers |
| payload | Payload |
| PMAD | Power Management And Distribution |
| prop | propulsive |
| props | Propellers |
| pt | Powertrain |
| ratio | Ratio |
| ref | reference |
| req | Required |
| safety | Safety |
| seat | Seat |
| seat,abrest | Seats Abrest |
| shaft | Shaft |
| SL | Sea Level |

| | |
|---|---|
| stall | dive |
| storage | Storage |
| t | Total |
| tail | Tail |
| tank | Fuel tank |
| temp,corr | Corrected Temperature |
| TO | Takeoff |
| tot | Total |
| turn | Turn |
| v | Vertical |
| vol | Volumetric |
| VT | Vertical Tail |
| wing | Wing |

# 1

# Introduction

In this introductory chapter, a short overview of the thesis as a whole is presented, along with the motivation for research on the topic of hydrogen fuel cells in aviation. In Section 1.1 the problem is defined, as well as the necessity for this research. Section 1.2 contains the research objective and research approach, while Section 1.3 states the research questions and the scope of the thesis. Finally, Section 1.4 gives the overall structure of the report.

## 1.1. Problem definition

There is a strong need for reducing global emissions in order to limit the effects of climate change. There has been growing interest in reducing emissions within the commercial aerospace industry in the last few years. At the moment, the commercial aviation sector is contributing about 3% to the global $CO_2$ emissions [1]. This number might seem small but the growth of the aviation sector is projected to be 4.3% per year [2]. Due to the current pandemic, this growth may drop significantly or reverse for a number of years. Nonetheless, aviation emissions are projected to increase in the medium and long term future. To offset this increase in emissions, aircraft and engine manufacturers are working together to improve the energy efficiency of the aircraft and reduce the fuel consumption of the propulsion systems. The improved energy efficiency is achieved through a combination of improved aerodynamic configurations, as well as improved propulsion systems. Fuel constitutes a major expenditure for airlines at around 25% of total costs [3], and thus the drive to reduce operating costs also aligns with the goal of greater efficiency. The foreseen incremental improvements of conventional propulsion systems result in reduced emissions and increased efficiency, that are projected to be 2.5% per year, with no explicit guarantee [1]. The most frequently used propulsion system for commercial aviation is the gas turbine, a technology that has undergone continuous improvements, but now may be approaching the maximum possible fuel efficiency. This could result in increased aviation emissions despite improving propulsive technology levels for individual aircraft.

To stimulate reduced emissions, the European Union has created a number of incentives, some of which are relevant to the aviation sector. These are known as Flightpath 2050 and few the goals are shown below:

- 75% reduction in $CO_2$ emissions per passenger kilometre
- 90% reduction in $NO_x$ emissions per passenger kilometre
- 65% reduction in perceived noise of flying aircraft.

These requirements are relative to the capabilities of new aircraft from 2000 [4].

To reach the ambitious Flightpath 2050 goals, more radical and advanced propulsion systems should be developed. The incremental improvements to gas turbines will not be enough to offset the growth of the commercial aviation sector as a whole, let alone reduce to zero-emission. There are several proposed propulsion systems that would be able to significantly increase efficiency and reduce emissions. In Flightpath 2050, the considered emissions are $CO_2$, $NO_x$ and noise.

The main propulsion system options are:

- Gas turbines combusting sustainable aviation fuel
- Gas turbines combusting hydrogen
- Fuel cells using hydrogen
- Fully electric battery powered
- Fuel cell battery hybrid electric

All of these options have the potential to become carbon neutral on a global level. However, this depends on the way the fuel/energy is produced. For example, in the case of the gas turbines using sustainable aviation fuel (bio- or synthetic fuel), the emissions in flight are offset by the sustainable production of the fuel on the ground. Similarly, the environmental impact of hydrogen production is highly dependent on how it is produced. Grey hydrogen is currently the most prevalent, and involves the steam reforming of methane. A by-product of this process is $CO_2$. If a large part (80-90%) of these $CO_2$ emissions is captured, the process produces blue hydrogen. The most sustainable way to produce hydrogen is through electrolysis using renewable energy, as this does not produce $CO_2$. This is known as green hydrogen [1]. Even the production of batteries will emit $CO_2$, as well the energy production if it is not renewable, for example if the electricity is produced using fossil fuels. This demonstrates that as far as global emissions are concerned, the emissions of a certain technology are highly dependent on the specific implementation.

However, the local emissions of these options greatly differ. Gas turbines combusting sustainable aviation fuel will emit a similar amount of emissions in flight when compared to current fossil fuelled gas turbines. Gas turbines burning hydrogen will not emit any $CO_2$ in flight. Nonetheless, the high operating temperatures in the combustion chamber will still create $NO_x$ emissions. These $NO_x$ emissions however, are projected to be lower than using conventional fuels. This is due to the wide flammability limits of hydrogen, which make a stable lean burn possible, thereby limiting $NO_x$ formation [5]. Noise emissions will also be similar.

Both gas turbines and fuel cells using hydrogen will produce water as a result of the chemical reaction of hydrogen with oxygen. These water vapour emissions are currently being researched as they may lead to radiative forcing, potentially contributing to climate change. However, the altitude at which this waste water is emitted is critical. It is generally believed that only water vapour emitted in the stratosphere is likely to contribute to the radiative forcing effect [6]. Therefore, this effect is most relevant for high altitude operation of aircraft in large aircraft categories.

Fuel cells on hydrogen, the fully electric and hybrid options do not have local $CO_2$ and $NO_x$ emissions. In addition to this, their electric powertrains allow for novel aircraft designs which may further increase efficiency and lower noise, such as distributed electric propulsion. However, fully electric powertrains are bound by battery energy density and volume, currently a severely limiting factor. Therefore hydrogen fuel cells have emerged as an interesting option for enabling fully sustainable air travel.

Summarizing, using hydrogen fuel cells for propulsion is a promising technology to get the commercial aerospace sector to zero emissions, provided that the hydrogen is produced in a sustainable manner [1] [5]. Hydrogen has already found niche applications in the aerospace industry, most notably as a high performance rocket fuel [2]. Applications for commercial aviation have, so far, not been possible.

When considering hydrogen fuel cell powertrains for aviation, there are several research topics which are relevant. These can be broadly categorized into component level and system level research. Component level research concerns topics such as hydrogen storage or fuel cell power generation. Meanwhile, system level research explores the influence of the novel powertrain.

To address the component level performance challenges, a detailed analysis of the individual components of the power system is required. For example, to improve the power density of fuel cell stacks, it is necessary to investigate molecular transport, among many other physical and chemical phenomena. These issues are highly detailed and focused on the individual parts of stack design which should be addressed by the fuel cell manufacturers to improve performance. Several current research efforts

[1] https://www.tno.nl/en/focus-areas/energy-transition/roadmaps/towards-co2-neutral-fuels-and-feedstock/hydrogen-for-a-sustainable-energy-supply/ten-things-you-need-to-know-about-hydrogen/ [Accessed 23-01-2021]

[2] https://www.nasa.gov/topics/technology/hydrogen/hydrogen_fuel_of_choice.html [Accessed 23-01-2021]

focus on component level performance, as this is not specific to aviation and can have benefits for other mobility sectors as well.

The system level performance is also an active topic of research. From an engineering perspective, to design a hydrogen fuel cell powered aircraft, the body of literature highlights the research efforts, but doesn't provide concrete guidelines. Rather, literature contains preliminary designs for hydrogen fuel cell aircraft. These designs range from modified 2-seater aircraft [7] [8] to completely novel aircraft concepts [7] [9]. Prototype hydrogen fuel cell aircraft are furthermore in development, such as ZeroAvia and H2FLY [10] [11]. However, these research efforts concern single point designs, and do not present general methodologies for the design of hydrogen fuel cell aircraft. As such, they are unsuitable for providing guidelines for the design of hydrogen fuel cell aircraft in general.

For conventionally powered aircraft, making use of piston or gas turbine engines, design methodologies exists [12] [13]. However, a general methodology for the preliminary design of hydrogen fuel cell powered CS-23 style aircraft is not presented in literature. The unique characteristics of a hydrogen fuel cell powertrain and its influence on aircraft design is not straightforward, compared to kerosene powered aircraft.

A general design methodology for the design of aircraft was therefore found to be a useful contribution to the state of the art. Additionally, this will provide a deeper understanding into the most important parameters of the power and propulsion systems design.

It was chosen to focus the design methodology on the CS-23 (Certification Specification) aircraft category, as defined by EASA (European Union Aviation Safety Agency). Starting the development of novel propulsion systems using smaller aircraft has several advantages. First of all, the technological requirements necessary to create a working prototype are lower, such as the specific power of the fuel cells. The power requirements for these aircraft are also in line with the power capabilities of current fuel cells. Creating a viable design is possible using short to medium term technology levels. Smaller aircraft require lower capital investment and thus are more attainable for development. In addition to this, the efficiency and performance of conventional propulsion systems in this category are relatively low, especially when compared to larger aircraft. For conventional powertrains, larger generally means more efficient. In contrast, in fuel cells, which are around 50% efficient, the efficiency is not scale dependant. Thus, for the CS-23 category, the increase in efficiency through use of fuel cells will be greater than for larger propulsion systems. The CS-23 aircraft category is ideally suited for the above mentioned developments. A recent amendment removes design limitations, allowing for new and revolutionary designs to be certified. New propulsion technologies are able to be certified under the CS-23 category [14]. The conclusion is that research into hydrogen fuel cell aircraft in the CS-23 category is a good starting point for hydrogen fuel cell powered aviation. The development efforts into this aircraft category will lead to more knowledge and technology improvements, which will allow for larger aircraft to be converted to hydrogen powertrains as well.

## 1.2. Research objective and approach

To guide the research efforts into a system level design methodology for hydrogen fuel cell powered aircraft, research framework is needed. This framework consists of a research objective, coupled with research questions. These have been formulated in the sections below.

The research objective is formulated as follows:

**"Development of a design methodology for conceptual design of hydrogen fuel cell powered CS-23 category aircraft"**

To achieve this research objective, several steps are required. These include a literature study on the relevant components and background information on the hydrogen fuel cell powertrain. This information is then used to construct relevant component level models of the power system. This power system model is implemented into a modified sizing methodology, which is able to take into account the peculiarities of the novel hydrogen fuel cell powertrain. This sizing methodology must be validated against existing aircraft to ensure the results are correct.

To support this research objective, several research questions have also been formulated.

## 1.3. Research scope and questions

To complete the research objective, the research has been split into two distinct directions. These research questions summarize the two main parts of this research. The first aim of the research is

to develop a conceptual design method for sizing hydrogen fuel cell aircraft. The second goal of the research is to determine the most important aspects of hydrogen fuel cell aircraft design. This includes the influence of component level performance as well as mission specifications. Sensitivity analysis on these parameters using a baseline aircraft will provide answers to these questions. The research questions are shown below.

- **What are the capabilities and feasibility of hydrogen fuel cell aircraft?**
    1. What are the main steps in creating a conceptual design for hydrogen fuel cell aircraft?
    2. What are the main parameters influencing the performance of hydrogen fuel cell aircraft?
    3. How does the payload range diagram of hydrogen fuel cell aircraft differ from kerosene powered aircraft?
    4. What future component level performance improvement has the largest effect on aircraft performance?

To achieve the overarching goal of determining the capabilities of hydrogen fuel cell aircraft, 4 main sub-questions have been formulated. To answer research question 1, it is necessary to identify the relevant steps in designing a hydrogen fuel cell aircraft. Using these steps, a general design methodology is developed. This methodology is implemented into a software tool in Python, the Hydrogen Aircraft Power & Propulsion Initial Estimator (HAPPIE). This tool guides the design process of new aircraft concepts, and allows for the accessibility of the methodology and its results.

To answer research questions 2, 3 and 4, the developed methodology and software tool are used to create a conceptual hydrogen powered aircraft design. This conceptual design and associated performance modeling are used to answer the questions relating to aircraft performance. The methodology and resulting aircraft designs are validated using existing aircraft.

This report aims to assist in improving the knowledge of hydrogen fuel cell aircraft, and paving a way for future research into this topic. This is done by developing the general design methodology and applying it to determine the feasibility of CS-23 hydrogen fuel cell powered aircraft. The tool will be developed in Python, partly because this allows for wide applicability. It also allows for the use of SUAVE (Stanford University Aerospace Vehicle Environment), a Stanford open source mission analysis tool written in Python [15] [16]. This capability can then be used as a basis for further development of hydrogen fuel cell aircraft concepts, guiding the future of hydrogen in aviation.

## 1.4. Thesis structure

This thesis is structured as follows: First, a background on hydrogen fuel cell technology is given in Chapter 2. From this background information, the most relevant performance parameters are extracted to construct the component models. In Chapter 3, the developed methodology for the sizing of hydrogen fuel cell aircraft is discussed. The implementation of this methodology in the HAPPIE software tool is described in Chapter 4. Chapter 5 describes the validation of the methodology using existing aircraft data for conventionally powered aircraft. Chapter 6 contains the results of the methodology and analysis, and discusses those results. The results contain the answers to the research questions. Chapter 7 contains a reflection and discussion on the results and methodology and its limitations. In Chapter 8 conclusions are drawn. Finally, Chapter 9 contains recommendations for further research.

# 2

# Background

In this chapter, the necessary background information for the conceptual design of hydrogen fuel cell aircraft is presented. First of all, in Section 2.1, the topic of aircraft conceptual design is introduced. The relevant system and component models are discussed, and the hydrogen fuel cell technologies are introduced. In Section 2.2 the hydrogen storage options are discussed, and in Section 2.3 the considered fuel cell technologies are presented. The additional components necessary in the hydrogen fuel cell powertrain are discussed in Section 2.4. An overview of the relevant technologies is given in Section 2.5.

## 2.1. Conceptual aircraft design

The process of designing an aircraft has several stages. Conceptual aircraft design is the first step in the design of aircraft. In this first stage, the major capabilities of the aircraft are determined, and the first estimates for the most important components are determined. These estimations are further refined in further design stages, such as the preliminary design phase, until there is a final design that can be manufactured and flown.

Conceptual aircraft design methodologies are presented by several authors [12] [13]. The first step of such methodologies is generally to determine the mass of the aircraft, without the determination of specific geometries or specifications. This is known as class 1 analysis. Important aspects for this stage of the analysis are the maximum take off mass $MTOM$ and the operating empty mass ($OEM$). The $MTOM$ represents the maximum mass of the fully loaded aircraft, while the $OEM$ is the mass of the aircraft without any fuel or payload on board.

For conventionally powered aircraft, both the $MTOM$ and $OEM$ can be determined using empirical correlations from a database of existing aircraft. This empirical data can be used to estimate the $MTOM$ and $OEM$ for different types of aircraft. Raymer details the procedure for estimation the MTOM using the payload mass ($m_{payload}$), fuel fraction ($\frac{m_{fuel}}{MTOM}$) and empty mass fraction($\frac{OEM}{MTOM}$), as shown in Equation 2.1 [13].

$$MTOM = \frac{m_{payload}}{1 - \frac{m_{fuel}}{MTOM} - \frac{OEM}{MTOM}} \tag{2.1}$$

The fuel fraction can be estimated using the mission of the aircraft and the Breguet range equation, while the empty mass fraction can be determined using the empirical aircraft data. So far, this process describes the conceptual design for conventionally powered aircraft. However, it cannot be directly used for the conceptual design for hydrogen fuel cell powered aircraft.

This is because there is no historical database of hydrogen fuel cell powered aircraft, from which the relations of fuel fraction and empty mass fraction can be obtained. Therefore, a modified class 1 mass estimation must be used. This involves the sizing of the most important components, resulting in their top level requirements. These can include mass, as well as volume and power. To conduct this more detailed class 2 estimation of the components, it is necessary to determine which components must be modeled.

There are several main aircraft components which need to be taken into account when differentiating between the conventional and hydrogen fuel cell aircraft. The wing may be different, as the wing loading and aircraft mass for a given aircraft might be different. The fuselage geometry and mass will also be different, due to the incorporation of the hydrogen fuel cell powertrain. Finally, the powertrain and fuel tank will be different as well. Regarding the hydrogen fuel cell powertrain, the two most important components are the hydrogen tank and the fuel cell. There are several other relevant powertrain components auxiliary components which are also discussed at the end of this chapter. By sizing all of these components, the final sizing result of the aircraft will provide details on the component level, instead of only on a system level.

## 2.2. Hydrogen storage

Hydrogen storage is a challenging problem, quite unlike the storage of conventional liquid fuels such as kerosene. This section will explore the relevant properties of both hydrogen itself and hydrogen storage options.

### 2.2.1. Hydrogen properties

Hydrogen is the lightest element on the periodic table, and the most abundant element in the universe. It has unique chemical properties, and these properties underline the challenges and opportunities that exist when considering it's use. These properties are best highlighted when compared to a conventional liquid fuel, kerosene.

Hydrogen has the highest energy content per unit mass of all chemical fuels. It has a lower heating value (LHV) of 120 $MJ/kg$, while kerosene has a LHV of around 43 $MJ/kg$. Hydrogen's very high energy content per unit mass is in contrast with its very low density. Hydrogen is the lightest element, and thus the least dense. At ambient temperature and pressure, the density of gaseous hydrogen is only 0.089 $kg/m^3$. By comparison, air has a density of 1.225 $kg/m^3$ at the same conditions, while kerosene has a density of around 800 $kg/m^3$. This means that storing a meaningful amount of hydrogen requires very large volumes under ambient conditions.

The main challenge for storing hydrogen is increasing its density, storing as much hydrogen as possible in a reasonable volume. In order to obtain satisfactory densities, the hydrogen can either be cooled down to a liquid state, or pressurized. Figure 2.1 shows hydrogen density under a range of pressures and temperatures. As can be seen, hydrogen density increases under high pressures and at (very) low temperatures, close to absolute zero.

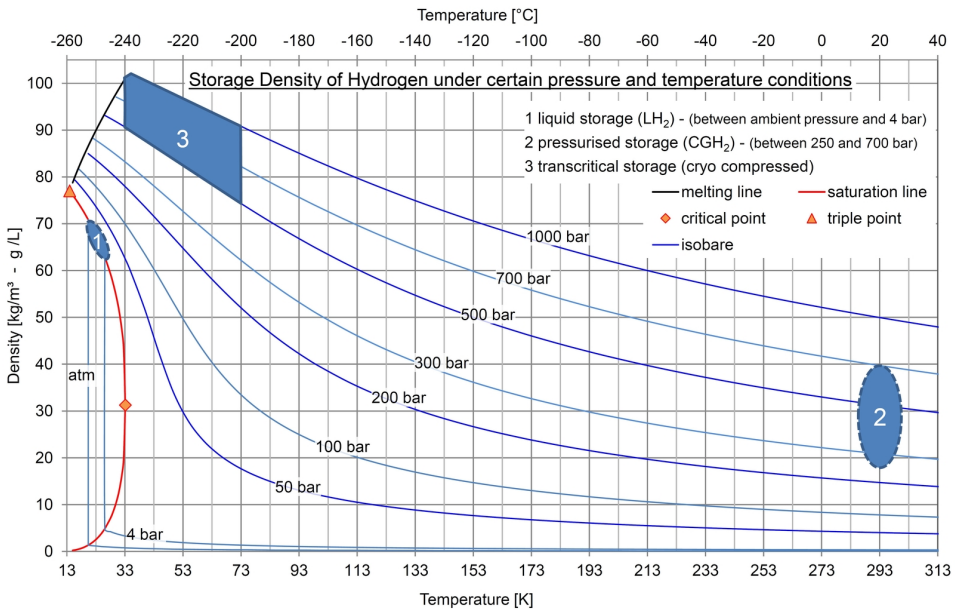


Figure 2.1: Net Storage Density of Hydrogen under a range of pressures and temperatures [1]

Both hydrogen storage methods discussed in subsequent sections rely on either low temperatures or high pressures to achieve this increased hydrogen density.

### 2.2.2. Hydrogen storage methods

The two main hydrogen storage methods that are relevant for aviation are compressed and cryogenic hydrogen storage. Other hydrogen storage methods such as metal and chemical hydrides are not suitable for aviation yet due to their low technology readiness levels[17]. These options are explored in detail in the following sections.

#### Compressed hydrogen storage

Compressed hydrogen storage works on the principle of increasing density by increasing pressure. As the hydrogen is simply compressed and stored in a pressure tank, compressed hydrogen storage is one of the simplest ways of storing hydrogen. There are four categories of compressed hydrogen storage vessels [17].

1. Type I: Fully metal pressure vessels.
2. Type II: Load bearing metallic liner wrapped in composite.
3. Type III: Non load bearing metallic liner wrapped in composite.
4. Type IV: Fully composite liner and composite wrapping.

An overview of these four types of compressed hydrogen storage is shown in Figure 2.2.

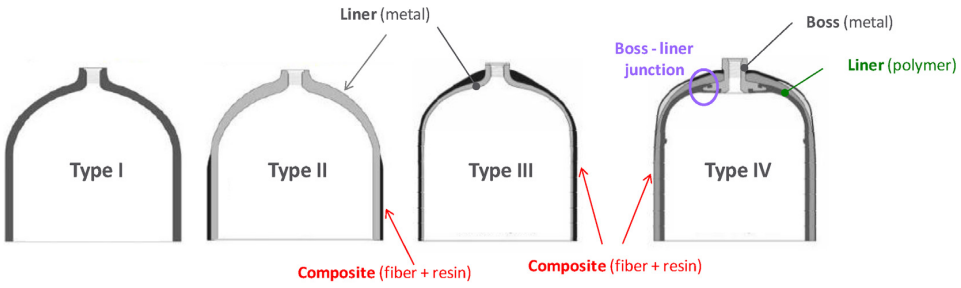


Figure 2.2: Compressed hydrogen storage types [17]

Generally, the type IV tanks are the highest performance (=lightest) tanks which are suitable for mobility applications. Type I tanks are more suitable for stationary storage and bulk transportation due to their lower cost. Hydrogen is commonly stored at either 300 bar or 700 bar for mobility applications.

Compressed hydrogen storage at 300 bar is the simplest of the storage methods. Even though 300 bar is a high pressure, its use requires only limited infrastructure (Type I hydrogen cylinder + pressure booster). At 300 bar the storage efficiency of the best tanks (Type IV) is around 5%. A higher storage efficiency means a lighter tank. The storage efficiency will be elaborated on in Section 2.2.3. Meanwhile the hydrogen density at 300 bars is around 20 $kg/m^3$. 300 bar hydrogen tanks are commercially available [2].

In current commercial hydrogen powered vehicles, 700 bar compressed hydrogen tanks are increasingly used. The hydrogen storage efficiency of current 700 bar tanks is higher than 300 bar tanks at around 10% [3]. The hydrogen density at 700 bars is 40 $kg/m^3$.

The main disadvantage of 700 bar tanks with respect to 300 bar tanks the increased infrastructure necessary to boost the hydrogen gas to such high pressures. In addition, the boosting of the hydrogen to higher pressures entails a larger loss of energy. The theoretical energy requirements for 700 bar hydrogen compression are only 4% of its LHV. However, in practice, compressing hydrogen requires between 5-20% of its LHV, depending on the specific process and the start and end pressure of the hydrogen

[1] https://www.ilkdresden.de/fileadmin/_processed_/2/f/csm_Storage_Density_of_Hydrogen_b71cedc151.jpg [Accessed 23-01-2021]
[2] http://www.ctscyl.com/prodotti/h2/?lang=en [Accessed 28-01-2021]
[3] https://www.toyota.com/mirai/ [Accessed 23-01-2021]

The main disadvantage of both the 300 and 700 bar pressure tanks is their relatively low storage efficiency, which lead to heavy tanks This is caused by the high strength of the tank required to hold the high pressures. This reduces the specific energy of the total pressurized hydrogen storage system. The substantial tank volume due to the low hydrogen density also increases the size of the total tank system. [18].

**Cryogenic liquid hydrogen storage**

The other physical way of storing hydrogen is to cool it down into a liquid state. For hydrogen this means cooling it down to around $20K$ (-$253C$). Cryogenic liquid hydrogen storage is used in the space industry and has been for the last several decades. For example, it has been used in the Saturn V upper stage as well as for the Space Shuttle. This is due to the fact that cryogenic liquid hydrogen has a relatively high density. The hydrogen density at $20K$ is around 70 $kg/m^3$. The handling of a liquid at this cryogenic temperature requires extraordinary caution and highly advanced insulation to prevent excessive boiling off of the hydrogen.

Due to the large temperature difference between the cryogenic hydrogen and the surrounding ambient, heat will flow from the environment into the hydrogen. This will in turn heat up the hydrogen, causing it to boil and revert to a gaseous state. As more gaseous hydrogen is formed in the tank, the pressure will gradually increase, until it exceeds the maximum allowable pressure for the tank. At this point the excess hydrogen will have to be vented from the tank. This boiled off hydrogen cannot be used and is lost, and thus undesirable. To reduce this boil off, thicker insulation can be used, which will delay the build-up of pressure. This comes at the cost of added weight and volume. If the hydrogen is gradually used up from the tank, this will compensate for the increased gaseous hydrogen volume in the tank. The drawback of more insulation is higher weight and larger volume. For applications where periods of inactivity are part of the mission, such as for road vehicles, the required insulation will be greater than for applications with a short mission duration, such as rockets. As such, the mass and volume of the tank depend strongly on the particular application and required insulation. For example, the storage efficiency of the space shuttle main tank was around 80%, because the hydrogen use during ascent was so much larger than the boil off rate. Because of this balance between boil off rate and tank mass and volume, the ideal insulation thickness will depend on the particular application.

The hydrogen boil off rate is related to the insulation thickness and the intended mission. If an aircraft is at low power outputs for a considerable amount of time, the boil off rate of the hydrogen might become larger than the power consumption and losses will occur. This effect is relevant for cases where the aircraft is stationary on the ground or taxiing. Therefore, when optimizing the tank insulation, the full mission of the aircraft should be taken into account [19]. However, during flight segments, the hydrogen necessary for propulsion exceeds the boil off rate. This means that if the hydrogen demand for propulsion is higher than the boil off rate, no hydrogen boil off will occur. For the conceptual design phase, the boil off is not directly taken into account. Instead the specified liquid hydrogen tank is assumed to have sufficient insulation to prevent boil off during the flight mission.

Meanwhile, liquefying hydrogen can require between 30-40% of its LHV, thus being very significant. The theoretical energy requirement for liquefying hydrogen are around 10% of it's LHV [18]. However, this concerns the production of the liquid hydrogen, and not the conversion to useful power, and as such doesn't directly affect the technical merits of liquid hydrogen storage on board aircraft.

Due to the very large volume taken up by liquid hydrogen tanks, they are usually placed in the fuselage of conventional aircraft. This also lowers the surface area that the cryogenic liquid is exposed to, limiting the insulation necessary to counter the boil off. However, placing the tanks in the fuselage limits the internal volume available for passengers and cargo. To allow for alternative placement of hydrogen tanks in aircraft, Winnefeld, Kadyk et al. explored the influence of changing the shape of cryogenic tanks on the storage efficiency. This has the added benefit of foresight when looking at future unconventional aircraft concepts. A tank in the shape of a sphere is the most efficient as it has the lowest possible surface area for a given volume. Storage efficiencies in excess of 70% appear possible when using currently available materials for aircraft.

This storage efficiency only slightly reduces for cylindrical tanks, but quickly drops when elliptical tanks are analysed. This is because when the tank shape differs significantly from the spherical or cylindrical tanks, there is an increased surface to volume ratio. This means that there must be more insulation to achieve the same boil off rate, and thus the storage efficiency reduces. Storage in wings does therefor not allow for the highest storage efficiencies [19]. Instead hydrogen is stored in the

fuselage itself in a cylindrical tank matching the dimensions of the fuselage. The total installed hydrogen tank mass is the lowest if it is made to be load bearing, thus being an integral structural part of the fuselage.

### 2.2.3. Hydrogen storage performance characteristics

Now that the relevant types of hydrogen storage have been discussed, it is useful to define the performance metrics by which they can be compared and modeled. The two main metrics by which hydrogen tank performance can be measured are the tank mass and the tank volume. The metrics are independent of tank shape, and can thus be used to describe any type of hydrogen tank.

**Tank mass / storage efficiency**

The tank mass is particularly relevant for hydrogen concepts, as storing hydrogen is not a trivial matter, requiring high pressures or low temperatures. Both of these methods required either thick insulation or strong tank walls. These can add considerable mass to the total tank and hydrogen system. In contrast, kerosene can usually be stored in the wing boxes without extensive extra structures. To describe the tank mass as a function of the hydrogen mass contained within it, the concept of storage efficiency is introduced. This is defined as the ratio of fuel mass ($m_{fuel}$) to total filled tank mass ($m_{fuel} + m_{tank}$), shown in Equation 2.2:

$$\eta_{storage} = \frac{m_{fuel}}{m_{fuel} + m_{tank}} \tag{2.2}$$

This storage efficiency $\eta_{storage}$ characterizes the mass of the tank in relation to the mass of the fuel. By rewriting Equation 2.2, it is possible to use the storage efficiency to calculate the tank mass for a certain fuel mass. For example, if the storage efficiency is 50%, that means that the tank mass is the same as the fuel mass it holds.

**Tank volume / volumetric efficiency**

Similarly, the volume of the tank is a relevant parameter, as this will influence the way the tank can be stored in the aircraft. First of all, the volume taken up by the fuel can be calculated using Equation 2.3, which relates the fuel mass and density to the total fuel volume.

$$V_{fuel} = \frac{m_{fuel}}{\rho_{fuel}} \tag{2.3}$$

To take into account the extra volume of the tank, consisting of the tank walls and auxiliary components such as valves and tubing, the concept of volumetric storage efficiency is introduced. This difference in volume consists of the tank walls, the insulation required for liquid hydrogen or the strong walls for compressed hydrogen tanks. The volumetric storage efficiency is defined in Equation 2.4, where $V_{fuel}$ is the internal fuel volume and $V_{tank}$ is the external tank volume.

$$\eta_{vol} = \frac{V_{fuel}}{V_{tank}} \tag{2.4}$$

By rewriting Equation 2.4, the external volume of the tank can be determined from the volumetric efficiency and the fuel volume. The volumetric efficiency can describe any tank shape, as it only relates the internal volume of the tank to the external volume. The internal and external shape of this volume are not determined, and can thus be used for any shape.

### 2.2.4. Hydrogen storage performance overview

This section will provide an overview of the considerations that are relevant for the hydrogen storage options as discussed above and in the context of the current research. These are shown in the list below:

- Hydrogen storage efficiency $\eta_{storage}$, which describes the mass of the hydrogen tank: Equation 2.2
- Tank volumetric efficiency $\eta_{vol}$, which describes the volume of the hydrogen tank: Equation 2.4
- Hydrogen density $\rho_{H_2}$, dictated by the type of hydrogen storage Figure 2.1

- Hydrogen energy content $LHV_{H_2}$: 120 MJ/kg

Storage efficiencies for current hydrogen storage techniques are around 5-10% for compressed hydrogen storage and 20% for liquid hydrogen storage. It is projected that liquid storage will be able to reach storage efficiencies of around 50%, due to the less stringent requirements on insulation as opposed to stationary hydrogen storage [7]. The volumetric efficiency is not predicted to strongly differ between current and future concepts, as very low temperatures and high pressures will still require a significant tank thickness. The range of storage efficiencies is caused by uncertainty in the application and manufacturing process [20].

A summary of the previously discussed parameters is shown in the tables below. These parameters can also be adapted to characterize kerosene and it's tank, and have been included for reference. Table 2.1 describes the energy storage parameters for current state of the art systems, while Table 2.2 details the energy storage parameters for near future technology levels.

Table 2.1: State of the art energy storage parameters

| | **Kerosene** | **300 bar** $H_2$ | **700 bar** $H_2$ | $LH_2$ |
|---|---|---|---|---|
| $\rho_{fuel}$ $[kg/m^3]$ | 800 | 20 | 40 | 70 |
| $LHV_{fuel}$ $[MJ/kg]$ | 43 | 120 | 120 | 120 |
| $\eta_{storage}$ [-] | 0.95 | 0.05 | 0.10 | 0.20 |
| $\eta_{vol}$ [-] | 0.95 | 0.50 | 0.50 | 0.50 |

Table 2.2: Future energy storage parameters

| | **Kerosene** | **300 bar** $H_2$ | **700 bar** $H_2$ | $LH_2$ |
|---|---|---|---|---|
| $\rho_{fuel}$ $[kg/m^3]$ | 800 | 20 | 40 | 70 |
| $LHV_{fuel}$ $[MJ/kg]$ | 43 | 120 | 120 | 120 |
| $\eta_{storage}$ [-] | 0.95 | 0.10 | 0.20 | 0.50 |
| $\eta_{vol}$ [-] | 0.95 | 0.50 | 0.50 | 0.50 |

## 2.3. Fuel cells

Fuel cells are energy converters, able to convert chemical energy stored in a fuel into useful energy, just like conventional (combustion) engines. However, fuel cells operate in a different way from conventional engines. Conventional heat engines such as a gas turbine or piston engine combust their fuel to create heat, which is then used to do work. Fuel cells on the other hand convert fuel through an electrochemical reaction which produces electricity, reaction products and waste heat. The basic components of any hydrogen fuel cell are an anode, cathode and membrane/electrolyte. Instead of allowing the hydrogen fuel to combust with oxygen directly, a fuel cell allows the reaction to happen electrochemically. The hydrogen fuel is supplied to the anode, while the required oxygen is supplied to the cathode. These are separated by an membrane. This membrane prohibits the flow of electrons, but allows the flow of ions. Depending on the type of fuel cell, different kinds of ions cross the membrane. Meanwhile, the anode and the cathode are connected through an external circuit, through which electrons can flow. The flow of electrons through the external circuit provides the electrical power produced by the fuel cell. The ion and the electron combine on the other side of the membrane to complete the reaction.

In all hydrogen fuel cells, the by-product of the reaction is water. The total reaction is the same as the combustion reaction, as shown in Equation 2.5.

$$H_2 + 1/2\ O_2 = H_2O \tag{2.5}$$

The voltage of an individual fuel cell is around $1V$, which is too low to provide useful power. Therefore, a number of cells are arranged in parallel and series configuration to form a fuel cell stack. The fuel cell stack is the core of the fuel cell system [21]. Figure 2.3 shows the schematic lay-out of a single proton conducting fuel cell.

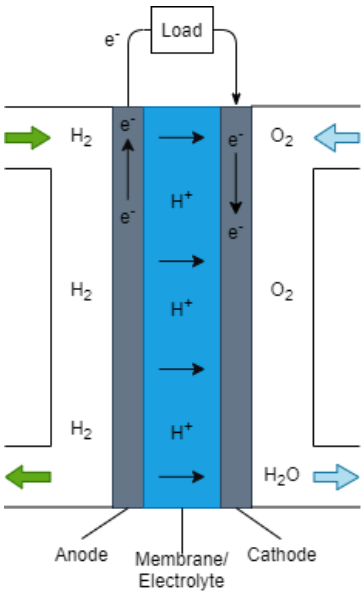


Figure 2.3: Diagram of a proton conducting fuel cell [adapted from [4]]

To allow for the optimal operation of the fuel cell stack, several auxiliary components are required. These are referred to as the balance of plant (BoP). The required balance of plant depends on the type of fuel cell. It can include compressors, humidifiers and cooling loops among other systems. The most relevant components are explored in Section 2.4. First, the relevant fuel cell types are discussed.

### 2.3.1. Fuel cell types

There are three main fuel cell types which are relevant for the aerospace industry:

- **LT-PEMFC** Low Temperature Proton Exchange Membrane Fuel Cell
- **HT-PEMFC** High Temperature Proton Exchange Membrane Fuel Cell

[4] https://commons.wikimedia.org/wiki/File:Solid_oxide_fuel_cell_protonic.svg [Accessed 23-01-2021]

- **SOFC** Solid Oxide Fuel Cell

**LT-PEMFC**
The most mature and prevalent type of hydrogen fuel cell at the moment is the low temperature proton exchange membrane fuel cell. This type of fuel cell typically uses a Nafion membrane that acts as the electrolyte, allowing protons to flow freely while blocking electrons. It is able to do this by including pockets of liquid water in the membrane through which the protons can travel. The membrane must be kept properly humidified using a humidifier, otherwise the water will evaporate and leave the membrane, drying out it out and limiting performance. The presence of liquid water in the membrane limits the temperatures that can be utilized by this type of fuel cell to around 60 - 95 $C$. Higher temperatures lead to the drying out of the membrane, even when properly humidified. This relatively low operating temperature, especially when compared to combustion engines, results in low quality heat, which can make it harder to keep the fuel cell cool. LT-PEMFC's also require a platinum catalyst which makes the fuel cell reaction possible. This contributes significantly to the cost. The catalyst is also sensitive to impurities in the hydrogen supply, particularly $CO$ which can poison the catalyst, severely limiting performance [22]. The advantages of this type of fuel cell include its high technology readiness level [23], as it is in commercial use. Furthermore, the low operating temperature allows for good load following characteristics and a fast startup time.

**HT-PEMFC**
High temperature proton exchange membrane fuel cells operate in the same way as low temperature PEMFC's, however they feature a different type of proton conducting membrane. Instead of relying on water for transporting the protons, a type of solid acid is used. This allows for this type of fuel cell to operate at temperatures above the boiling temperature of water, commonly around 200 $C$. This would dry out the Nafion membrane of the LT-PEMFC, but this is not the case for the acid based membrane of the HT-PEMFC. The higher operating temperatures allow for efficient operation as the membrane resistance at higher temperatures is lower. In addition to this, the higher operating temperature means that cooling should be easier due to the larger temperature gradient. Drawbacks of this type of fuel cell are the fact that it needs to heat evenly before being used, making the start-up time potentially long at around 30 minutes. In addition, the higher temperatures create a corrosive environment which limits durability and reliability. These factors culminate in the fact that the TRL (Technology Readiness Level) of the HT-PEMFC is lower than the LT-PEMFC [24].

**SOFC**
Solid oxide fuel cells operate in a different way from PEMFC's. Instead of allowing proton transport through the membrane, they operate at sufficiently high temperatures to allow for oxide ions to pass through a solid oxide material, hence their name. The high operating temperature (600-1100 degrees $C$) allows them to be used in a combined cycle with a gas turbine, and even allows for the use of light hydrocarbon fuels such as propane, which are internally reformed in the fuel cell stack. As with the HT-PEMFC, the high operating temperature can lead to long start-up times up to 30 minutes. Solid oxide fuel cells have mostly been used for backup power and stationary power applications, but have recently been used in UAS (Unmanned Aerial Systems) instead of small internal combustion engines, due to their low noise, flexible fuel and electric power capabilities. The limiting factor is the thermal stress that is caused by uneven heating [25].

### 2.3.2. Fuel cell characteristics
To model the fuel cells described in the previous sections, some models must be developed. Fuel cells have several defining characteristics, the most important of which are the fuel cell efficiency $\eta_{FC}$, specific power $\hat{\rho}_{FC}$ and operating temperature $T_{oper}$. The characteristics reported here are valid for all hydrogen fuel cells.

**Fuel cell efficiency**
Since fuel cells do not operate as heat engines, they are not bound by the Carnot efficiency like combustion engines. The maximum theoretical fuel cell efficiency is 83%, however due to real world effects fuel cells cannot reach this high efficiency [26]. A fuel cell is generally not designed to operate around the maximum possible power, party due to the lower efficiency at high power levels, and party due to

lower durability. Fuel cells typically are designed to have 50% efficiency at nominal power. At maximum power, a given fuel cell's efficiency might only be 30%. As opposed to combustion engines, fuel cells have their highest efficiency at the lowest load. Due to real world effects such as losses in the proton transport and internal current losses, at extremely low power settings the efficiency of the fuel cell system is lower, however these power levels are so low that they are not relevant. The voltage of an individual fuel cell is directly related to it's efficiency, as shown in Equation 2.6 for the LHV of hydrogen [21].

$$\eta_{FC_{LHV}} = \frac{V_{cell}}{1.254} \tag{2.6}$$

The fuel cell behaviour is commonly represented by a polarization curve, relating the voltage of the fuel cell to the current drawn per unit area. This allows for the comparison of fuel cells of different sizes and configurations.

Figure 2.4 shows the general shape of such a polarization curve. As the fuel cell voltage is directly related to the efficiency of the fuel cell, the curve can also be interpreted as efficiency as a function of current density.

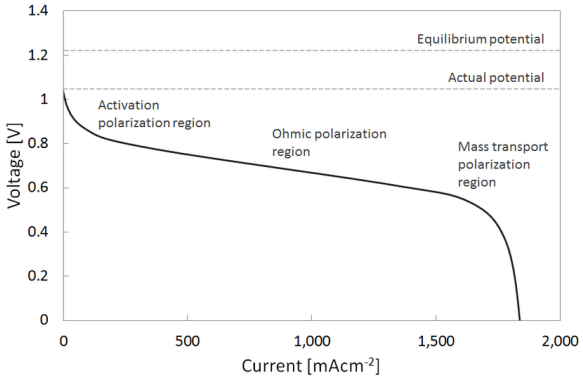


Figure 2.4: Example Fuel Cell Polarization Curve [5]

This polarization curve is the same general shape for all fuel cell types, but is also influenced by operating pressure and temperature.

To model this behaviour of the fuel cell, several models exist. For this report, an empirical set of correlations is used [27]. This allows for the characterization of the generalized behaviour of a fuel cell stack, without requiring more detailed component characteristics, such as voltage, current density and membrane resistances [21].

The polarization curve as specified by the empirical model is shown in Figure 2.5. This is the polarization curve of a single cell. However, by normalizing the behaviour of one fuel cell to its power and efficiency, the behaviour of an entire stack can be determined. As mentioned earlier, fuel cells can be placed in series or in parallel. The specific arrangement determines how much power is produced, and what the voltage and current ranges are for this power output. The normalization of the fuel cell behaviour allows for the analysis of all types of fuel cells, independent of their specific arrangement.

This polarization curve can be used to determine the power as a function of current density. This procedure is shown in Equation 2.7. $A_{FC}$ is the fuel cells active area, which when multiplied with the current density $i$ results in the current through the fuel cell. This current multiplied by the voltage $V$ results in the power produced by the fuel cell.

$$P_{FC} = V\ i\ A_{FC} \tag{2.7}$$

The result of this calculation for an example fuel cell is shown in Figure 2.6

This power can be normalized, and plotted on the x-axis. Thus, the normalized power will correspond to a specific voltage of the fuel cell. The voltage each cell produces is directly related to the efficiency of the fuel cell, as shown in Equation 2.6.

[5] https://www.researchgate.net/figure/Typical-polarization-curve-for-PEM-fuel-cells-Activation-ohmic-and-mass-tr fig2_281647856 [Accessed 23-01-2021]

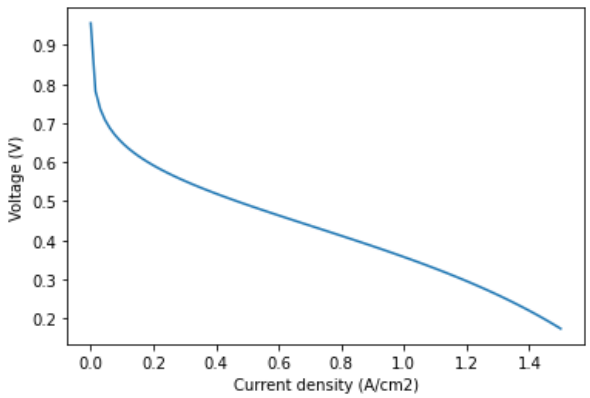


Figure 2.5: Fuel cell Polarization Curve

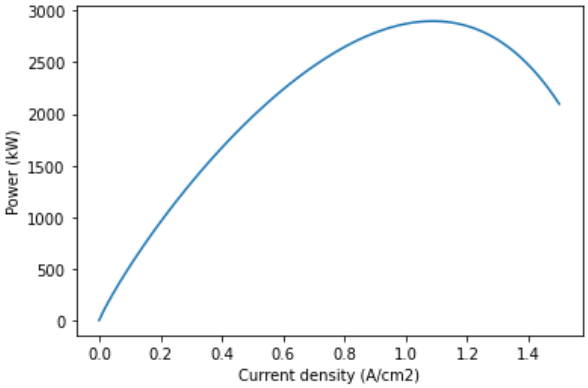


Figure 2.6: Fuel cell Power curve

This allows for the plotting of efficiency as a function of normalized power. The normalized polynomial which describes fuel cell efficiency as a function of normalized power demand of the fuel cell is shown in Figure 2.7.

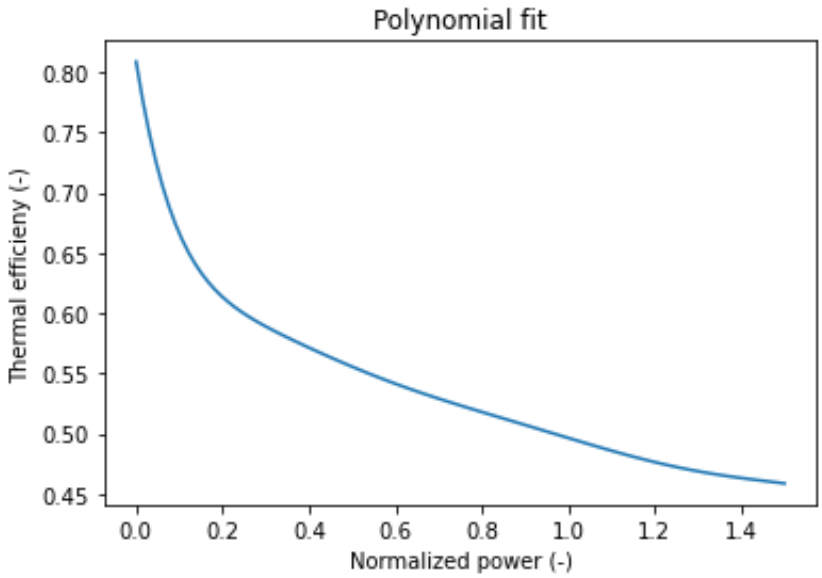


Figure 2.7: Fuel cell stack polynomial fit

Using this polynomial, depending on the amount of power the fuel cell must produce, the fuel cell efficiency can be predicted. This efficiency has an influence on the hydrogen fuel mass flow, which influences the aircraft sizing and performance.

**Fuel cell specific power**

Another relevant characteristic for fuel cells is the specific power. It represents the mass of the fuel cell for a given power output. It is expressed as $[W/kg]$, as shown in Equation 2.8

$$\rho_{\hat{FC}} = \frac{P_{FC}}{m_{FC}} \tag{2.8}$$

Using the fuel cell power required and the fuel cell specific power, the mass of the fuel cell can be estimated. This mass does not take into account the auxiliary components required for fuel cell operation, and as such these must be determined separately. For current fuel cell technologies, 2000 $[W/kg]$ on a stack level is considered to be a reasonable assumption, based on publicly available data [6].

[6] https://www.datocms-assets.com/36080/1611437833-p-stack.pdf [Accessed 10-02-2021]

As for the hydrogen storage, the exact value depends on the particular application and implementation. For future technology levels, a conservative 3000 [$W/kg$] is chosen.

**Fuel cell operating temperature**
The final important fuel cell characteristic is the operating temperature. This is mainly dictated by the type of fuel cell, and the balance of plant for that specific fuel cell architecture. The three main fuel cell types for aviation are discussed in the previous section. The fuel cell operating temperature mainly influences the design of the cooling system, which is discussed in Section 2.4

### 2.3.3. Fuel cell performance overview
This section provides an overview with the parameters that are relevant for the fuel cells discussed above and in the context of the current research.

- FC efficiency $\eta_{FC}$, which influences the mass of fuel required for a given mission. The fuel cell efficiency is dictated by the
- FC specific power $\hat{\rho}_{FC}$, which influences the mass of the fuel cell stack. It is dictated by the technology level of the fuel cell.
- Operating temperature $T_{oper}$, which influences the size of the cooling system. It is determined by the type of fuel cell.

An overview of these parameters for the current technology levels are shown in Table 2.3, while the future technology levels are shown in Table 2.4. The efficiency of 50% represents the average efficiency at the nominal load. As explained earlier, the fuel cell is not modeled with a fixed efficiency.

Table 2.3: State of the art fuel cell performance comparison

| | LT-PEMFC | HT-PEMFC | SOFC |
|---|---|---|---|
| $\eta_{FC}$ [-] | 0.50 | 0.50 | 0.50 |
| $\hat{\rho}_{FC}$ [$W/kg$] | 2000 | 2000 | 2000 |
| $T_{oper}$ [$C$] | 80 | 200 | 600 |

Table 2.4: Future fuel cell performance comparison

| | LT-PEMFC | HT-PEMFC | SOFC |
|---|---|---|---|
| $\eta_{FC}$ [-] | 0.50 | 0.50 | 0.50 |
| $\hat{\rho}_{FC}$ [$W/kg$] | 3000 | 3000 | 3000 |
| $T_{oper}$ [$C$] | 80 | 200 | 600 |

## 2.4. Additional relevant powertrain components
As explained in the previous section, fuel cells required extra components to function properly. These are known as the balance of plant. In addition to this, the fuel cell produces electric power, which cannot be directly used to propel the aircraft. The hydrogen fuel cell powertrain must transform this electrical power to shaft power to turn propellers and finally produce thrust.

### 2.4.1. Fuel cell balance of plant
The balance of plant components ensure that the fuel cell can operate optimally. The two components that are relevant to be modeled in the conceptual design phase are the turbo-normalizing compressor and the cooling system.

**Turbo-Normalizing compressor**
Fuel cells have the capability to operate at different operating pressures. Generally, the research into the topic indicates that fuel cells have increased efficiency and performance at elevated pressure levels. However, this is offset by the necessity to use fuel cell power to compress the incoming air. Thus, it is not feasible to simply maximize the pressure of the incoming air. This would reduce the net output power

of the fuel cell, because the compressor must be powered using power produced by the fuel cell. On the other hand, reducing the operating pressure below ambient pressures also has a detrimental effect on fuel cell performance. Research indicates that fuel cells lose performance faster than combustion engines [28] at increased altitudes, due to low pressures, densities and temperatures. Low pressure fuel cell operation is an active topic of research, and currently does not lend itself to be included in this analysis.

Thus a compressor is generally used to provide a certain pressure to the fuel cell. This is generally between ambient pressure, and maximally around 2 bar gauge pressure [21]. This also ensures airflow through the fuel cell, as the fuel cell itself doesn't have any moving components to cause an active replenishment of new air/oxygen.

A turbo-normalizing compressor provides sea level pressure air to the fuel cell, even when the fuel cell is operating at higher altitudes where the air density is lower. The pressure ratio of the compressor is dictated by the pressure altitude, while the air mass flow is dictated by the fuel cells power level.

The relevant performance characteristics for a turbo normalizing compressor are its polytropic efficiency $\eta_{comp}$ and its specific power $\hat{\rho}_{comp}$.

**Cooling system**

Fuel cells have thermal efficiencies around 50% at their nominal power output. This means that a 100kW fuel cell will reject 100kW of waste heat. The cooling of fuel cells has several differences with the cooling of conventional combustion engines. The efficiency of fuel cells is higher than internal combustion engines, however the operating temperatures are generally lower (LT-PEMFC's operate around 60 - 95°C). This is similar to the heat of combustion engines, but there is a large difference in the exhaust heat. The exhaust heat of the LT-PEMFC fuel cell is much lower, and thus despite being more efficient, there is more heat to be rejected to the cooling system [29]. This combined with the lower temperature difference to ambient, results in low quality heat which is harder to reject or use in a combined cycle. This heat must be rejected by a cooling system, as otherwise the fuel cell would overheat. There is not forced airflow through the fuel cell stack, as there are no moving components. Therefore a compressor is necessary as mentioned earlier to reject the waste air. Furthermore, this waste air does not contain the bulk of the heat, because the reaction takes place in the fuel cell itself, and not in a combustion chamber heating the air.

For the cooling of fuel cells there are several options. These include air cooling, liquid cooling and evaporative cooling. Air cooling is used for smaller fuel cell stacks, in which the power output is low enough to allow for passive cooling solutions. Once the power output is higher than around 5 kW, it is necessary to adopt either liquid cooling or evaporative cooling to allow for a compact design [29]. Fly et al. compared evaporative cooling versus liquid cooling. The conclusion is that the use of evaporative cooling results in a 27% reduction in radiator frontal area. This is supports aircraft drag reduction [29]. For high temperature fuel cells, cooling is also investigated for use in aviation. Barroso et al. researched the heat transfer for HT-PEMFC in UAV's [30] . This study looked at a high temperature fuel cell being air cooled at a high altitude. In a continuation of this study [31], a feasible design was made for the cooling of the stack. The power output of the stack in was around 1 $kW$ and therefor did not require a dedicated cooling loop. This demonstrates the different cooling needs for different power outputs. Power outputs under 5 $kW$ are generally air-cooled, while higher power outputs have dedicated liquid and evaporative cooling loops.

The design of cooling systems is non trivial, and as such it is necessary to determine a generalized solution for use in a design routine. A NASA paper on thermal design for electric aircraft [32] explored the design and optimization of such cooling systems for electric aircraft, and the methods can also be extended for use with hydrogen fuel cell powertrains. The result of the optimization performed in the cited NASA paper is a relation between the heat power and temperature to be rejected, and thrust/drag, mass, power demands of the cooling system. These relations are explored in the methodology in the next chapter.

### 2.4.2. Additional powertrain components

For use in aircraft, the fuel cell power system requires several extra components. Besides the fuel cell power generation itself, this power must also be distributed and transformed into useful thrust for aircraft propulsion. This is done using a power management and distribution system, electric motors and propellers.

**Power Management And Distribution**
The fuel cells produce direct current (DC), however, due to efficiency and power considerations, the electric motors are driven by alternating current (AC). To change from direct to alternating current, an inverter is needed. Furthermore, as the power demanded from a fuel cell increased, the voltage decreases. This is opposite to how an electric motor is commonly driven, by increasing the supply voltage to allow the motor to produce more power. Once the electric power has been generated in the fuel cell stack, it must be distributed to the electric motors to produce the shaft power necessary to turn the propellers and produce thrust to ultimately propel the aircraft. All these tasks are done using a Power Management and Distribution system. This system of cables, inverters, converters and other electrical equipment transports the electric power produced by the fuel cell to the electric motors. The mass and efficiency of such a system must be taken into account when designing an aircraft. The relevant parameters for the PMAD system are the specific power $\hat{\rho}_{PMAD}$ and efficiency $\eta_{PMAD}$.

**Electric motors**
Finally, the electric motors convert the electric power to shaft power to turn the propellers. The relevant parameters for modeling the electric motors are the specific power $\hat{\rho}_{em}$ and the efficiency $\eta_{em}$.

**Propellers**
The propellers finally transform the shaft power produced by the electric motors into thrust, which is used to propel the aircraft. The propellers have an associated propulsive efficiency. The propulsive efficiency of well optimized propellers have values of around 0.8. Equation 2.9 shows how the propulsive efficiency is used to relate the thrust to the shaft power.

$$T = \frac{P_{shaft}}{V_{aircraft}} * \eta_{prop} \tag{2.9}$$

The relevant performance parameter for the propellers is the propulsive efficiency $\eta_{prop}$

### 2.4.3. Other powertrain components
There are a couple of powertrain components that have not been directly considered in this definition of the hydrogen fuel cell powertrain. The humidifier is the main one, which is required for LT-PEMFC operation to keep the membrane humidified. However, it is not an active component, and it is not present in the other fuel cell types. An extra mass budget is therefore considered. This mass budget also includes other powertrain components, such as cables, tubing and mounting structures. Since this contribution is unsure, it is taken to add an extra 20% to the total mass of the powertrain.

For the current methodology, the use of batteries in conjunction with the fuel cell is not considered. This is done for several reasons. First of all, by considering an exclusively hydrogen fuel cell powertrain, the characteristics and viability of such a system are explored. By considering a battery hybrid power system, the necessary battery sizing and power control strategies of the hybrid powertrain would perhaps obscure some behaviour. Secondly, literature indicates that oversizing the fuel cell for a given mission can be beneficial due to increased efficiency [33]. If an aircraft is sized for a fuel cell to provide all the required power, as is done in the proposed methodology, batteries are not necessary for peak power. They would still be useful for power smoothing for transient power control strategies, however this is not appropriate for the conceptual design phase. Finally, several past and current hydrogen fuel cell aircraft do not make use of hybrid battery powertrains, thus demonstrating that it is not an invaluable component.

However, this does not imply that hybrid electric battery fuel cell powertrains are not viable or beneficial. They have been included as an important recommendation in Chapter 9.

## 2.5. Overview of hydrogen fuel cell powertrain
In section, an overview of the entire hydrogen fuel cell powertrain is given. The hydrogen fuel cell power system is shown in Figure 3.7.

Following the airflow, the turbo-normalizing compressor compresses the ambient air and leads this into the fuel cell. In the fuel cell, the hydrogen from the hydrogen tank and the oxygen in the air combine electrochemically to produce water, electricity and waste heat. The water and unused oxygen are vented through an exit nozzle to the ambient air. The electricity is led through the PMAD to the

electric motors, which produce shaft power to turn the propellers, producing thrust for flight. The fuel cell waste heat is rejected through the cooling system, which has a separate inlet, heat exchanger, and puller fan to ensure adequate airflow, as well as an exit nozzle. The green boxes represent parts of the powertrain that have been modeled, including their masses, efficiencies and powers. The red boxes represent the heat exchanger, whose mass is taken into account. The blue box is the hydrogen supply, which is discussed in Section 3.4.2. Lastly, the grey boxes represent parts of the powertrain that have not been modeled explicitly.

The assumed technology levels for each of the most important powertrain components are shown in Table 2.5. They are shown for a conventional gas turbine, state of the art liquid hydrogen fuel cell system, as well as a future liquid hydrogen fuel cell system, with technology levels assumed to be available around 2035.

Table 2.5: Current and future powertrain parameters

| **Parameter** | **GT** | **HFC SOA** | **HFC Future** |
|---|---|---|---|
| Power generation specific power: $\hat{\rho}_{FC}$ $[W/kg]$ | 3000.0 | 2000.0 | 3000.0 |
| Power delivery specific power: $\hat{\rho}_{PMAD}$ $[W/kg]$ | - | 10000.0 | 15000.0 |
| Power conversion specific power: $\hat{\rho}_{em}$ $[W/kg]$ | - | 5000.0 | 10000.0 |
| Power generation efficiency: $\eta_{FC}$ [-] | 0.25 | 0.5 | 0.5 |
| Power delivery efficiency: $\eta_{PMAD}$ [-] | 0.95 | 0.9 | 0.95 |
| Power conversion efficiency: $\eta_{em}$ [-] | 0.95 | 0.9 | 0.95 |
| Energy source storage efficiency: $\eta_{storage}$ [-] | 0.95 | 0.2 | 0.5 |
| Energy source volumetric efficiency: $\eta_{vol}$ [-] | 0.95 | 0.5 | 0.5 |
| Energy source density: $\rho_{fuel}$ $[kg/m^3]$ | 800 | 70 | 70 |
| Specific energy: $LHV_{fuel}$ $[MJ/kg]$ | 43 | 120 | 120 |

Now that the background on hydrogen fuel cell powertrains has been presented, the conceptual design methodology for these novel powertrains is discussed in the next chapter, Chapter 3.

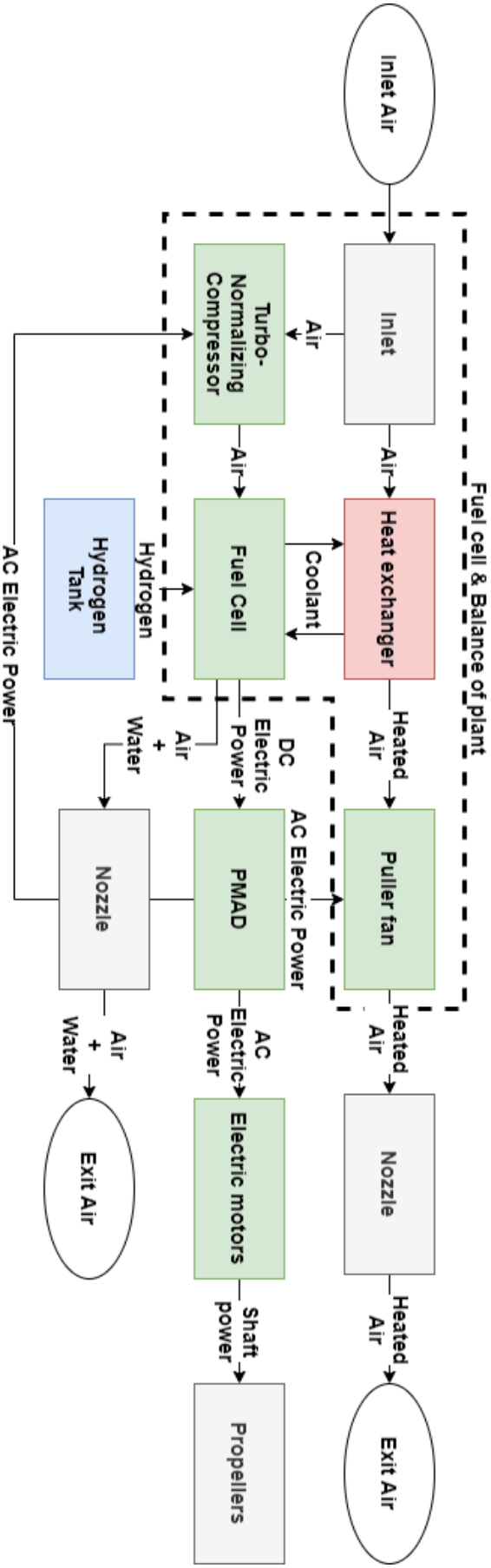


Figure 2.8: Hydrogen fuel cell powertrain diagram

# 3

# Methodology

The methodology that has been developed combines top-level mission requirements for a hydrogen fuel cell aircraft and translates them into a conceptual aircraft design. This methodology consists of several steps, each of which will be discussed in the sections below. An overview of the methodology is shown in Figure 3.1.

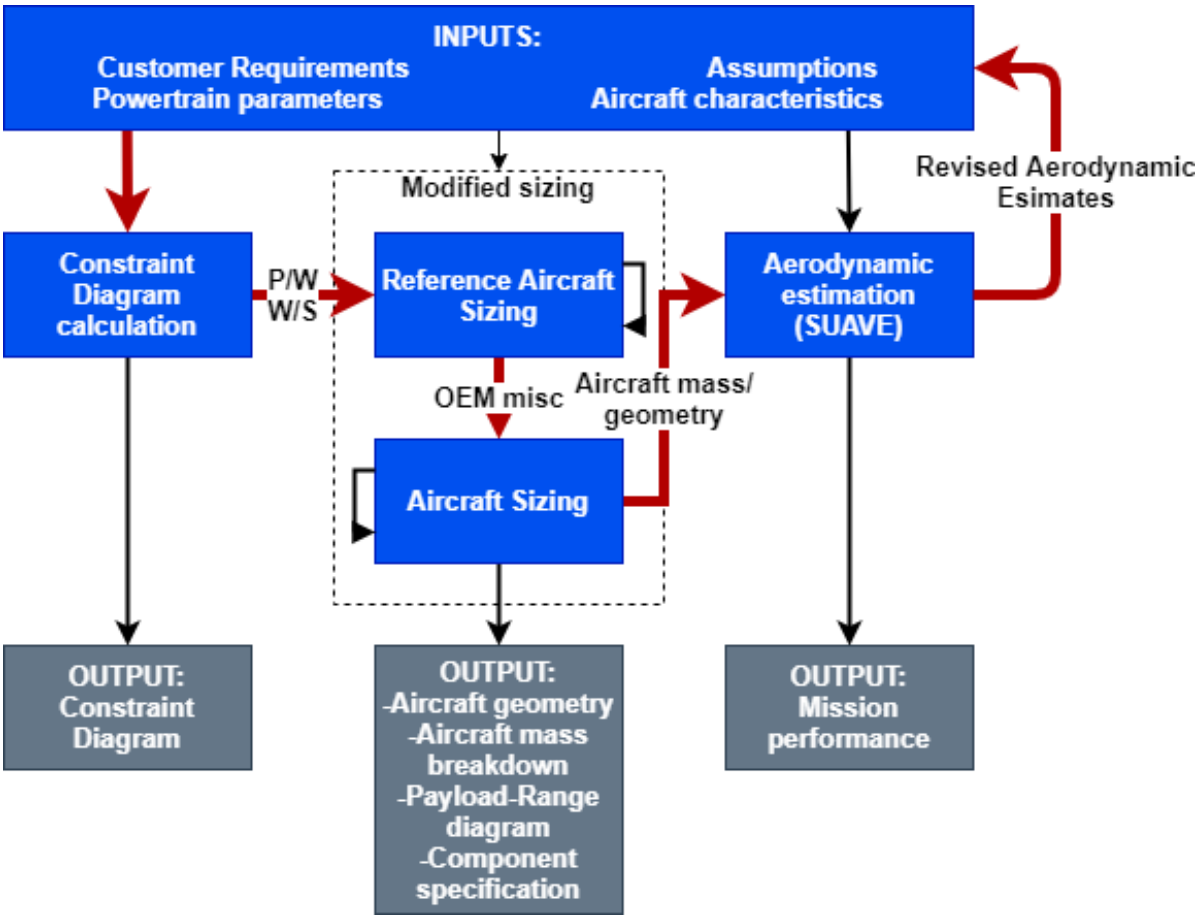


Figure 3.1: Methodology Flowchart

The methodology consists of several distinct steps.

1. The customer requirements and other performance parameters are used to construct a constraint diagram, which results in a requirement for the P/W (Power to Weight) and W/S (Wing loading)

ratio's. These ratio's will be used later on in the sizing routine to determine the required power output and wing area for a given aircraft weight.

2. A reference aircraft is sized for the harmonic mission using conventional (kerosene) values in a convergence loop. Once the reference aircraft is sized, the mass of the wing, fuselage, powertrain and tank are determined using class 2 methods. These masses are subtracted from the $OEM_{ref}$, resulting in the $OEM_{misc}$ (Miscellaneous Operating Empty Mass). This $OEM_{misc}$ represents the mass of the aircraft, excluding the wing, fuselage, powertrain and tank masses. This follows the methodology by [34].

3. Using the obtained $OEM_{misc}$, the mass of the hydrogen fuel cell aircraft can be built up by considering the masses for the wing, fuselage, fuel cell powertrain and hydrogen tank. The sizing routine for the harmonic mission consists of several iterative loops. The main loop converges on the mass of the entire aircraft. A smaller loop converges on the power required from the fuel cell, based on the power required for flight, along with compressor and cooling system power requirements. This procedure is shown in Figure 3.6. The result of this sizing are aircraft component masses and geometries. These results can be used to construct the payload range and planform diagrams.

4. To improve the validity of the results, higher order aerodynamic methods are used to revise the estimates for the minimum drag coefficient ($C_{D_{min}}$), lift induced drag constant ($k$) and the Lift to Drag ($L/D$) ratio. This is done using SUAVE, which will be elaborated on in Chapter 4. This mission analysis in SUAVE also generates mission performance results for the harmonic mission.

5. These revised aerodynamic estimations are fed back into the assumptions, and used go through the sizing routine again. This iterative loop is run until there is convergence on the sizing of the aircraft. After this final round of fidelity improvements, a feasible aircraft design is obtained.

## 3.1. Inputs to the methodology

The inputs to the methodology are split into 4 different categories.

- Customer requirements
- Assumptions
- Powertrain parameters
- Aircraft characteristics

In Sections 3.1.1 to 3.1.4, example values are shown for each of these categories. These values do not represent the limits of the CS-23 category, but rather of a relevant example aircraft. In this case the values belong to a hydrogen fuel cell powered aircraft, based on the Cessna 208. The results of these inputs are discussed in Section 6.1.

### 3.1.1. Customer requirements

The customer requirements input category mainly determines the mission performance requirements for the aircraft. These include the harmonic range of the aircraft, the cruising altitude, cruise speed and payload capacity. A full list with example inputs is shown in Table 3.1.

The harmonic range represents the range the aircraft can travel with its maximum design payload. Next, several important velocities are introduced. These are used to determine the performance requirements of the aircraft in different scenarios. The stall speed and takeoff ground roll distance largely determine the way the aircraft can be used and from which airfields it can operate. The service ceiling is the maximum altitude that the aircraft can fly at, while the cruise altitude is the altitude at which the cruise phase is conducted. The aircraft considered in this category are unpressurized, thus limiting the operational altitude to around 3km. However, no such limitation is present within the CS-23 certification category, as pressurized aircraft and/or oxygen masks are present on some aircraft.

The number of passengers combined with the payload mass determine the total payload carried by the aircraft. Finally, the energy source oversizing factor accounts for the extra fuel able to be taken on board the aircraft, past what is necessary for the harmonic mission. If this input is 1, the tank is designed to carry exactly the fuel required for the harmonic mission.

The inputs that are shown here are all from the customer requirements. Since the aircraft considered are part of the CS-23 category, there are also some certification requirements that must be met for this type of aircraft. However, the newest set of CS-23 category requirements have been written in such a way as to be flexible. There are no fixed regulations on the performance and design of the aircraft, other than a limit of 19 passengers and a maximum takeoff mass of 8618 kg. The other guidelines for the performance of the aircraft are not fixed, but rather must be reported to comply with the certification requirements [1].

Table 3.1: Example Customer Requirements

| Parameter | Value |
|---|---|
| Harmonic range: $R$ $[km]$ | 317.0 |
| Sustained turning speed: $V_{turn}$ $[m/s]$ | 75.0 |
| Climb speed: $V_{climb}$ $[m/s]$ | 70.0 |
| Takeoff speed: $V_{TO}$ $[m/s]$ | 50.0 |
| Cruise speed: $V_{cruise}$ $[m/s]$ | 93.0 |
| Sea Level rate of climb: $V_v$ $[m/s]$ | 6.27 |
| Service ceiling rate of climb: $V_{v_{ceiling}}$ $[m/s]$ | 0.51 |
| Stall speed: $V_{stall}$ $[m/s]$ | 30.0 |
| Maximum dive speed: $V_{dive}$ $[m/s]$ | 150.0 |
| Takeoff ground roll distance: $S_G$ $[m]$ | 800.0 |
| Service ceiling: $h_{ceiling}$ $[m]$ | 7620.0 |
| Cruise altitude: $h_{cruise}$ $[m]$ | 3000.0 |
| Design airfield altitude: $h_{TO}$ $[m]$ | 0.0 |
| Load factor/Sustained G's in turn: $n$ [-] | 1.41 |
| Number of passengers: $N_{pass}$ [-] | 10 |
| Payload mass: $m_{payload}$ $[kg]$ | 300.0 |
| Energy source oversizing factor: $C_{oversize}$ [-] | 4.5 |

### 3.1.2. Assumptions

The assumptions input category include preliminary assumptions about the aircraft's aerodynamics. The assumptions are based on empirical data reflecting values typical for CS-23 category aircraft [12]. The full list is shown in table 3.2. The minimum drag coefficient ($C_{D_{min}}$), lift induced drag constant ($k$) and the Lift to Drag ratio ($L/D$) are **bold** to highlight that these parameters are revised using refined aerodynamic estimations. The reference empty mass fraction ($(OEM/MTOM)_{ref}$) is used to describe the empty mass fraction for the reference aircraft, and is dependant on the specific type of aircraft.

Table 3.2: Example Assumptions

| Parameter | Value |
|---|---|
| **Minimum drag coefficient:** $C_{D_{min}}$ [-] | 0.028 |
| Takeoff drag coefficient: $C_{D_{TO}}$ [-] | 0.05 |
| Takeoff lift coefficient: $C_{L_{TO}}$ [-] | 0.7 |
| Maximum lift coefficient: $C_{L_{max}}$ [-] | 2.2 |
| **Lift induced drag constant:** $k$ [-] | 0.058 |
| Ground friction constant: $\mu$ [-] | 0.04 |
| **Lift to Drag ratio:** $L/D$ [-] | 12.38 |
| Passenger mass: $m_{pass}$ [kg] | 93 |
| Safety factor: $C_{safety}$ [-] | 1.5 |
| Reference empty mass fraction: $(OEM/MTOM)_{ref}$ [-] | 0.6 |

[1] https://www.easa.europa.eu/newsroom-and-events/press-releases/easas-re-written-cs-23-revolutionary-paves-way-n [Accessed 06-02-2021]

### 3.1.3. Powertrain parameters

The powertrain parameters define the most important aspects of the powertrain, as discussed in Chapter 2. These include the choice of fuel, but also the specific power and efficiency of several parts of the powertrain. These inputs also specify the powertrain performance level. The powertrain definition has been generalized to allow for the analysis of kerosene and hydrogen fuel cell powertrains. The parameters are shown in Table 3.3. In the case of the hydrogen fuel cell powertrain, the power generation represents the fuel cell, the power delivery represents the PMAD and the power conversion represents the electric motors. For the kerosene powertrain, the power generation is assumed to be the engine itself, while the power deliver and power conversion represent the gearbox and bearings. The energy source density represents the density of the fuel, either hydrogen or kerosene. The specific energy is the LHV of the fuel. The propulsive efficiency takes into account the efficiency of converting shaft power to propulsive thrust power. The number and diameter of the propellers is used for visualization only in this methodology. The operating temperature of the powertrain is used for the cooling system design and depends on the powertrain. The cooling thrust correction factor is not integrated into the main methodology but rather discussed in Section 3.7. Finally, the compressor specifications are also recorded.

Table 3.3: Example Powertrain parameters

| Parameter | Value |
|---|---|
| Power generation specific power: $\hat{\rho}_{FC}$ $[W/kg]$ | 2000.0 |
| Power delivery specific power: $\hat{\rho}_{PMAD}$ $[W/kg]$ | 10000.0 |
| Power conversion specific power: $\hat{\rho}_{em}$ $[W/kg]$ | 5000.0 |
| Power generation efficiency: $\eta_{FC}$ [-] | 0.5 |
| Power delivery efficiency: $\eta_{PMAD}$ [-] | 0.9 |
| Power conversion efficiency: $\eta_{em}$ [-] | 0.9 |
| Energy source storage efficiency: $\eta_{storage}$ [-] | 0.2 |
| Energy source volumetric efficiency: $\eta_{volumetric}$ [-] | 0.5 |
| Energy source density: $\rho_{fuel}$ $[kg/m^3]$ | 70.0 |
| Specific energy: $LHV_{fuel}$ $[MJ/kg]$ | 120.0 |
| Propulsive efficiency: $\eta_{prop}$ [-] | 0.8 |
| Number of propellers: $N_{props}$ [-] | 1 |
| Propeller diameter: $D_{prop}$ $[m]$ | 3.0 |
| Powertrain operating temperature: $T_{oper}$ $[C]$ | 80.0 |
| Cooling thrust correction: $C_{coolthrust}$ [-] | 0.0 |
| Compressor specific power: $\hat{\rho}_{comp}$ $[W/kg]$ | 2000.0 |
| Compressor efficiency: $\eta_{comp}$ [-] | 0.7 |

### 3.1.4. Aircraft characteristics

The aircraft characteristics describe aircraft design choices which are made by the designer. These include choices related to the seating arrangement, wing aspect ratio, and other settings which influence the geometry of the aircraft. These parameters are shown in Table 3.4.

Table 3.4: Example Aircraft Characteristics

| Parameter | Value |
|---|---|
| Wing aspect ratio: $AR_{wing}$ [-] | 9.7 |
| Sweep Quarter chord: $\Lambda_{C/4}$ [-] | 0.0 |
| Thickness to chord ratio: $t/c$ [-] | 0.2 |
| Taper Ratio: $\lambda$ [-] | 0.8 |
| Seats abreast: $N_{seat,abreast}$ [-] | 2 |
| Nose fineness ratio: $F_{nose}$ [-] | 1.5 |
| Tail fineness ratio: $F_{tail}$ [-] | 2.0 |
| Seat pitch: $l_{seat}$ [m] | 0.8 |
| Door length: $l_{door}$ [m] | 1.0 |
| Horizontal tail Aspect Ratio: $AR_{HT}$ [-] | 5.0 |
| Vertical tail Aspect Ratio: $AR_{VT}$ [-] | 5.0 |

## 3.2. Constraint diagram

The first step of the conceptual design methodology is to determine the aircraft **power to weight ratio** ($P/W$) and **wing loading** ($W/S$). $P/W$ describes the power the aircraft can produce divided by the aircraft weight. Meanwhile, the wing loading relates the weight of the aircraft to the area of the wing. These parameters are calculated using a constraint diagram.

The constraint diagram is generated using the methods and equations as presented by Gudmundsson in his book General Aviation Aircraft Design [12]. There are six different flight conditions used to construct the constraint diagram, from which suitable $P/W$ and $W/S$ are determined. These flight conditions place performance constraints on the aircraft. These performance characteristics have been rewritten so the power to weight ratio is a function of the wing loading, into the form $P/W = f(W/S)$. This allows them to be plotted on the constraint diagram, with wing loading on the x-axis and power to weight ratio on the y-axis.

### 3.2.1. Flight conditions

The six flight conditions that are used to determine the constraint diagram are discussed in the list below. These equations specify a thrust to weight ratio ($T/W$), which will be transformed into the required power to weight ratio in subsequent sections. In these Equations, $q$ is the dynamic pressure at the specified condition and $k$ is the lift induced drag constant.

1. **Level flight constant velocity turn**
   The constant velocity turn specifies the amount of thrust to weight ratio required to perform a constant velocity turn, without losing altitude or airspeed. It is shown in Equation 3.1.

$$\frac{T}{W}_{turn} = q_{turn}\left[\frac{C_{D_{min}}}{(W/S)} + k\left(\frac{n}{q_{turn}}\right)^2\left(\frac{W}{S}\right)\right] \tag{3.1}$$

2. **Rate of climb at sea level**
   The rate of climb at sea level determines how fast the aircraft can climb. Equation 3.2 shows the relation. $V_v$ is the rate of climb, while $V_{climb}$ is the best climb speed.

$$\frac{T}{W}_{climb} = \frac{V_v}{V_{climb}} + \frac{q_{climb}}{(W/S)}C_{D_{min}} + \frac{k}{q_{climb}}\left(\frac{W}{S}\right) \tag{3.2}$$

3. **Takeoff ground roll distance**
   The ground roll takeoff distance directly constrains which airfields the aircraft can operate from. Equation 3.3 shows the correlation. $S_G$ is the ground roll distance, and $\mu$ is the ground friction constant.

$$\frac{T}{W}_{TO} = \frac{V_{TO}^2}{2g \cdot S_G} + \frac{q_{TO} \cdot C_{D_{TO}}}{W/S} + \mu\left(1 - \frac{q_{TO} \cdot C_{L_{TO}}}{W/S}\right) \tag{3.3}$$

4. **Cruise Airspeed**
   The cruise airspeed is an important constraint, determining how fast the aircraft can cover the mission cruise distance. It is shown in Equation 3.4.

$$\frac{T}{W}_{cruise} = q_{cruise}C_{D_{min}}\left(\frac{1}{W/S}\right) + k\left(\frac{1}{q_{cruise}}\right)\left(\frac{W}{S}\right) \tag{3.4}$$

5. **Service ceiling**
   The service ceiling of the aircraft determines the maximum operational altitude of the aircraft. Equation 3.5 shows this expression.

$$\frac{T}{W}_{ceiling} = \frac{V_{v_{ceiling}}}{\sqrt{\frac{2}{\rho_{ceiling}}\left(\frac{W}{S}\right)\sqrt{\frac{k}{3 \cdot C_{D_{min}}}}}} + 4\sqrt{\frac{k \cdot C_{D_{min}}}{3}} \tag{3.5}$$

6. **Stall speed**
   An important aircraft performance constraint is the minimum speed at which flight can be maintained. This final flight constraint determines the wing loading for a certain stall speed, shown in Equation 3.6. This is determined using the maximum lift coefficient $C_{L_{max}}$, and the required minimum stall speed, incorporated in $q_{stall}$. Equation 3.6 shows the procedure.

$$\frac{W}{S}_{stall} = q_{stall} * C_{L_{max}} \tag{3.6}$$

### 3.2.2. Shaft power to weight ratio

For aircraft making use of jet propulsion, the thrust to weight ratio is the appropriate metric for engine selection. However, for aircraft using propellers for propulsion, the power to weight ratio is a more useful metric for engine and power selection. As each of the equations shown above express the relationship in terms of thrust to weight, it is necessary to transform them to power to weight. This is done using the known flight speed at each of these flight conditions $V$ $[m/s]$ and dividing by the propulsive efficiency $\eta_{prop}$ [-]. This results in the shaft power to weight ratio required, shown in Equation 3.7.

$$\frac{P_{shaft}}{W} = \frac{T}{W}\frac{V}{\eta_{prop}} \tag{3.7}$$

$\eta_{prop}$ represents the propulsive efficiency of the propeller, thus converting the propulsive power required to the shaft power of the aircraft.

For conventional sizing methodologies, it is common practice at this stage to normalize the constraint diagram to S-L (Sea Level) conditions, to aid in engine selection. In these conventional methodologies, this is done using engine performance maps for gas turbines or the Gagg-Ferrar model for piston-engine power plants [12].

However, when analysing unconventional powertrains, these types of performance maps are not available, As such the constraint diagram will **not** be normalized in this methodology. This means that the power to weight ratio that is calculated using the constraint diagram equations represents the shaft power to weight ratio required ($P_{shaft}/W$) to sustain flight in each flight condition. In the rest of the report, $P/W$ represents the shaft power to weight ratio unless otherwise specified.

### 3.2.3. Result of the constraint diagram

Each of these flight constraints is plotted on the constraint diagram, as shown in Figure 3.2. The constraint diagram represents each of the flight conditions as a line. Each line represents the minimum power to weight ratio required for a given wing loading which will allow the aircraft to perform the specified maneuver. Furthermore, the stall speed constraint is a vertical line, indicating the maximum allowable wing loading.

Once the lines are drawn on the constraint diagram, a combination of $P/W$ and corresponding $W/S$ is chosen which satisfies all of the specified constraints. This chosen point must lie above all the lines. If the chosen point falls below one or more lines, it will not satisfy the flight performance requirements of those specific flight conditions. Furthermore, a wing loading lower or equal to the stall speed constraint must be chosen. Thus, using the constraint diagram, the lowest P/W is chosen which satisfies all constraints. This is represented by the red dot in Figure 3.2.

The results of the constraint diagram calculation are the $P/W$ and corresponding $W/S$ required for the aircraft. Furthermore, because the constraint diagram also shows the $P/W$ requirement for specific flight segments, such as cruise and climb, these power to weight ratios can be used for refined power estimations in later steps of the methodology.

For reference, several CS-23 category aircraft are also included in the constraint diagram as black dots. The list of aircraft is shown in Table 3.5. The inclusion of the reference aircraft provides context for the validity of the selected $P/W$ and $W/S$. The general trend that can be observed with these reference aircraft is that both the power to weight ratio and the wing loading increase with increasing $MTOM$. Thus, the lightest and smallest aircraft are situated on the bottom left, while the larger aircraft are found in the top right of the constraint diagram. Finally, the red dot represents the design point which satisfies all of the constraints. The $P/W$ and $W/S$ are used to size the aircraft in the following steps.

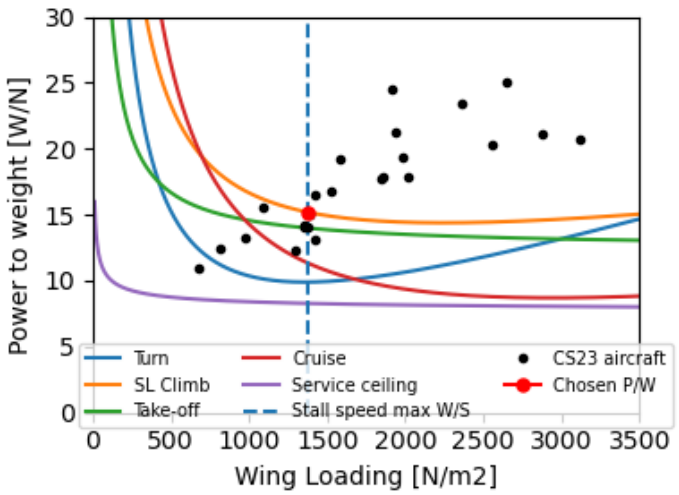


Figure 3.2: Example Constraint diagram

Table 3.5: Reference CS-23 aircraft [2]

| | |
|---|---|
| Cessna 172 | DHC-6 Twin otter 300 |
| Tecnam P2006T | Short Skyvan |
| Piper PA-34 seneca | EMB-110 |
| BN-2 Islander | DH114 Heron |
| Cessna 208 Caravan | Dornier 228 |
| Piaggio P-166 | Let L-420 |
| Do 28D-2 | IAI Arava |
| GAF N24A | Beechcraft Super King air 350 |
| BN-2A MK3 | British Aerospace Jetstream 31 |
| Gulfstream Jetprop 1000 | Fairchild Metro 23 III |
| Beech C99 | CASA C212 Aviocar series 400 |
| Mitsubishi MU-2 | Beechcraft 1900D |

## 3.3. Reference aircraft sizing

After the calculation of the required $P/W$ and $W/S$, the next step in the methodology is to size the aircraft. This is done using a modified class 1 mass estimation. The modified class 1 mass estimation is based on the modified method proposed by Roelof Vos, Reynard de Vries and Malcom Brown in their paper: Preliminary Sizing for Hybrid Electric Distributed Propulsion aircraft [35]. The challenge of sizing conceptual aircraft is shared for both hybrid electric and hydrogen fuel cell aircraft. The problem is that there is no empirical database available for these type of aircraft with which to perform a class 1 mass estimation. As there are currently only prototype hydrogen fuel cell aircraft, it is not possible to extract enough empirical data to directly perform a class 1 mass estimation.

The solution to this problem is to size a reference aircraft for same mission. This conventional reference aircraft can be sized using conventional class 1 methods. Once the reference aircraft has been sized, the most important component mass contributions are determined. These are the mass of the wing, fuselage, powertrain and tank, and are determined using class 2 methods. These masses are subtracted from the $OEM$ of the reference aircraft, resulting in the $OEM_{misc}$ (Miscellaneous Operating Empty Mass). This $OEM_{misc}$ represents the mass of the aircraft, excluding the wing, fuselage, powertrain and tank masses. The hydrogen fuel cell aircraft can then be sized using the reverse process, building up the $OEM$ from the $OEM_{misc}$. This procedure is shown in the next section.

This reference aircraft is sized using conventional powertrain values. These are shown in Table 3.6.

[2] Compiled from Jane's All the World's Aircraft and `https://www.airliners.net/aircraft-data` [Accessed 09-02-2021]

Table 3.6: Reference Aircraft powertrain values

| Parameter | Value |
|---|---|
| Total powertrain efficiency: $\eta_{pt_{ref}}$ [-] | 0.20 |
| Powertrain specific power: $\hat{\rho}_{pt_{ref}}$ $[W/kg]$ | 3000 |
| Fuel storage efficiency: $\eta_{storage_{ref}}$ [-] | 0.95 |
| Fuel volumetric efficiency: $\eta_{vol_{ref}}$ [-] | 0.95 |
| Fuel density: $\rho_{kerosene}$ $[kg/m^3]$ | 800 |
| Fuel energy content: $LHV_{kerosene}$ $[MJ/kg]$ | 43 |
| Empty mass fraction: $OEM/MTOM_{ref}$ [-] | 0.6 |

### 3.3.1. Estimation of reference aircraft MTOM

The first step in the sizing of the reference aircraft, is to determine the $MTOM$. This is done using Equation 3.8, adapted from Raymer [13].

$$MTOM_{ref} = \frac{m_{payload}}{1 - (\frac{m_{fuel}}{MTOM})_{ref} - (\frac{OEM}{MTOM})_{ref}} \tag{3.8}$$

The payload mass ($m_{payload}$) is extracted directly from the inputs. The empty mass fraction ($(\frac{OEM}{MTOM})_{ref}$) is estimated from empirical data. Gudmundsson presents empty mass fraction trends for different CS-23 category aircraft, which are shown in Figure 3.3 [12]. Based on this, 0.6 has been chosen to be a representative baseline value. For this methodology, this value of 0.6 is constant as an initial assumption for the general methodology. For more refined sizing results, this empty mass fraction should be matched to the specific aircraft type.

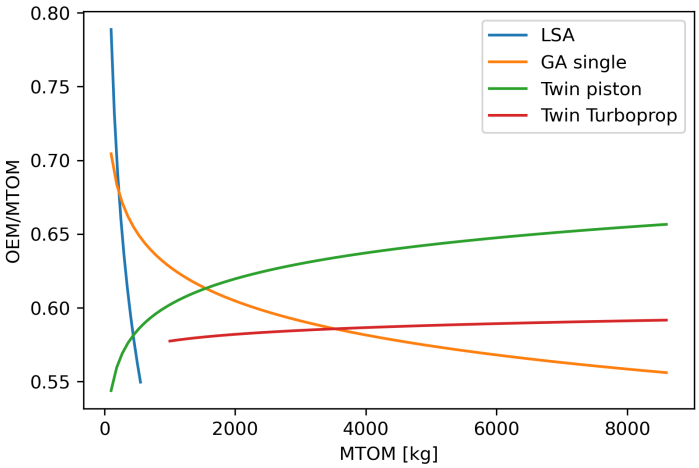


Figure 3.3: Empty mass fraction vs MTOM

To calculate fuel mass fraction $\frac{m_{fuel}}{MTOM}_{ref}$ of the aircraft, the fuel mass required for the mission must be determined.

#### Cruise fuel mass fraction

The main contributor to fuel mass is the cruise segment of the flight. The cruise segment of the flight can be described by the Breguet range equation, as shown in Equation 3.9 for propeller aircraft. $M_{ff_{cruise}}$ is the cruise mass fraction.

$$R_{cruise} = \frac{LHV_{fuel}}{g} \eta_{prop} \eta_{pt} L/D \ ln(M_{ff_{cruise}}) \tag{3.9}$$

To determine the range for which the Breguet range equation is valid, the cruise range must be estimated. This can be done using Equation 3.10. The total range $R_{total}$ is obtained from the customer requirements.

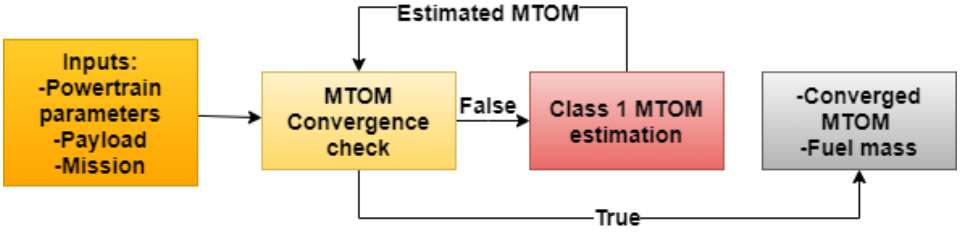


Figure 3.4: Reference aircraft MTOM iterative loop

$$R_{cruise} = R_{total} - R_{climb} - R_{descent} \tag{3.10}$$

The climb range is determined by the time to climb to cruise altitude, and the climb speed maintained during that segment. Equation 3.11 shows the time to climb to altitude, while Equation 3.12 shows the distance covered during the climb. A constant rate of climb and climb speed is assumed throughout the climb segment.

$$t_{climb} = \frac{h_{cruise} - h_{TO}}{V_v} \tag{3.11}$$

$$R_{climb} = V_{climb}\ t_{climb} \tag{3.12}$$

The descent segment is assumed to cover the same range as the climb segment.

To estimate this cruise mass fraction, the Breguet range equation is rewritten, as shown in Equation 3.13.

$$M_{ff_{cruise}} = exp(\frac{R_{cruise}\ g}{LHV_{kerosene}\ \eta_{prop}\ \eta_{pt_{ref}}\ (L/D)}) \tag{3.13}$$

In addition to the fuel consumed during the cruise segment, fuel is also required for takeoff, climb and descent. To take this fuel into account, the fuel mass fraction for these segments must also be estimated. Since these calculations depend on the $MTOM_{ref}$ of the aircraft, an iterative loop must be used to converge on the final $MTOM_{ref}$. The iterative loop is shown in Figure 3.4.

**Takeoff fuel mass fraction**

To take into account the fuel mass required for takeoff, it is common to use empirical data on the mass fraction for the takeoff segment. However, a more detailed approach is adopted here, which is also suitable for hydrogen fuel cell powertrains. Thus, instead of determining a mass fraction, first an energy requirement is determined.

To take into account the energy required to takeoff, it is assumed that 1 minute of full power is required, as shown in Equation 3.14.

$$E_{TO_{ref}} = 60\ (P/W)_{ref}\ MTOM_{ref}\ g \tag{3.14}$$

This energy requirement will be added to the energy requirement for the climb segment, and used to calculate a fuel requirement for these segments.

**Climb fuel mass fraction**

To estimate the energy required for the climb segment, first the power required for the climb segment is extracted from the constraint diagram $(P/W)_{climb}$, as shown in Equation 3.15.

$$P_{climb_{ref}} = (P/W)_{climb}\ MTOM_{ref}\ g \tag{3.15}$$

To estimate the energy needed for climb, this climb power is assumed to be required during the entire climb segment. The time required for the climb segment is shown in Equation 3.11. Constant rate of climb and climb speed are assumed.

The total energy required for the climb segment is calculated by Equation 3.16

$$E_{climb_{ref}} = P_{climb_{ref}}\ t_{climb} \tag{3.16}$$

The energy requirements for the descent segment are assumed to be insignificant when compared to the takeoff, climb and cruise segments, and are thus not taken into account. These extra energy contributions must be lumped together, and translated into an extra fuel mass requirement, shown in Equation 3.17.

$$m_{fuel_{extra_{ref}}} = \frac{E_{climb_{ref}} + E_{TO_{ref}}}{LHV_{kerosene} * \eta_{pt_{ref}}} \tag{3.17}$$

The mass fraction for the takeoff and climb segment $M_{ff_{extra}}$ is therefore given in Equation 3.18.

$$M_{ff_{extra_{ref}}} = \frac{MTOM_{ref} - m_{fuel_{extra_{ref}}}}{MTOM_{ref}} \tag{3.18}$$

Thus the total mass fraction for the entire flight is given by Equation 3.19.

$$M_{ff_{total_{ref}}} = M_{ff_{cruise}}\ M_{ff_{extra}} \tag{3.19}$$

The fuel mass can be determined using equation 3.20.

$$m_{fuel_{ref}} = MTOM_{ref} - \frac{MTOM_{ref}}{M_{ff_{total_{ref}}}} \tag{3.20}$$

This fuel mass can be used to determine the fuel mass fraction of the aircraft.

$$(\frac{m_{fuel}}{MTOM})_{ref} = \frac{m_{fuel_{ref}}}{MTOM_{ref}} \tag{3.21}$$

This fuel mass fraction is subsequently used in Equation 3.8 to determine a new estimate of the $MTOM_{ref}$. This iterative loop is performed until there is convergence on the final $MTOM_{ref}$, as shown in Figure 3.4.

After the $MTOM_{ref}$ has been calculated, the $OEM_{ref}$ is calculated using Equation 3.22.

$$OEM_{ref} = MTOM_{ref}\ (\frac{OEM}{MTOM})_{ref} \tag{3.22}$$

### 3.3.2. Estimation of reference aircraft components

The second step in the procedure for sizing the reference aircraft is shown in Figure 3.5. After the $MTOM$ and $OEM$ have been determined, the $OEM$ is further split into the major components. Class 2 mass estimation techniques are used to determine the masses of these aircraft components. These are the powertrain, fuel tank, wing and fuselage mass.

The goal of sizing these components is to estimate the Miscellaneous Operating Empty Mass $OEM_{misc}$, which is used in the next step of the methodology to conduct the hydrogen fuel cell aircraft sizing.

#### Reference powertrain mass

The powertrain mass for the reference aircraft is determined using the specific power of the powertrain, as specified in Table 3.6. The mass of the powertrain depends on the power required. This power requirement is a function of the mass of the aircraft and the required power to weight ratio as determined by the constraint diagram, as shown in Equation 3.23.

$$P_{req_{ref}} = P/W_{shaft}\ MTOM_{ref}\ g \tag{3.23}$$

Once the power requirement has been determined, Equation 3.24 calculates the powertrain mass, relating the power required to the specific power of the powertrain $\hat{\rho}_{pt_{ref}}$.

$$m_{pt_{ref}} = \frac{P_{req_{ref}}}{\hat{\rho}_{pt_{ref}}} \tag{3.24}$$

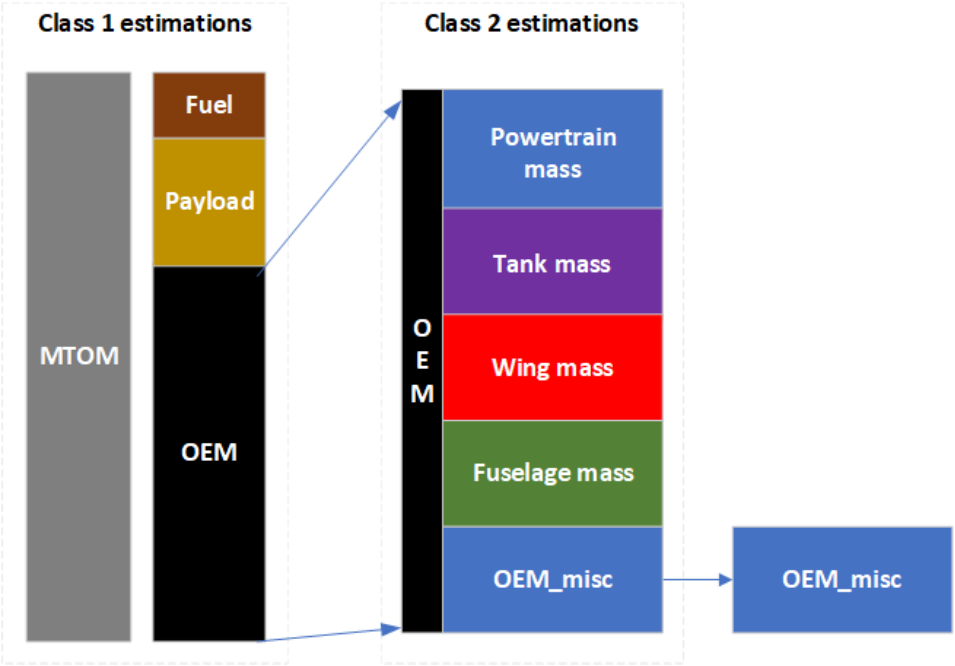


Figure 3.5: Reference Aircraft mass breakdown

**Reference tank mass**

The mass of the fuel tank is determined using the storage efficiency, as explained in Section 2.2. For the reference kerosene powered aircraft, the storage efficiency is relatively high (0.95), since the fuel can be stored in the wing structure without many additional components. Equation 3.59 shows how the tank mass is determined. $C_{oversize}$ represents an oversizing factor of the fuel mass the tank can hold. This determines the amount of extra fuel that can be taken past what is required for the harmonic mission. This cannot exceed the amount of wing tank volume available, otherwise additional fuel tanks would be required. $C_{oversize}$ is part of the customer requirements.

$$m_{tank} = \frac{m_{fuel}\, C_{oversize}}{\eta_{storage}} - (m_{fuel}\, C_{oversize}) \tag{3.25}$$

**Reference wing mass**

The mass of the wing is determined by its geometry. The wing geometry is defined using the wing loading, along with user inputted parameters. From the constraint diagram, a certain wing loading $W/S$ is specified. This relates the $MTOM$ of the aircraft to the required wing area $S$. The wing area is calculated by equation 3.26.

$$S_{wing} = \frac{MTOM\ g}{W/S} \tag{3.26}$$

Once the wing area has been determined, the wingspan is determined in Equation 3.27 using the specified aspect ratio.

$$b_{wing} = \sqrt{AR_{wing}\, S_{wing}} \tag{3.27}$$

The other geometrical characteristics, such as taper ratio ($\lambda$), thickness to chord ($t/c$) and wing sweep quarter chord ($\Lambda_{C/4}$) are obtained from the inputs directly. These can be used to construct a planform view of the wing.

The weight of the wing is estimated using these geometrical characteristics, according to Equation 3.28 by Raymer [12]. It is given in imperial units, and thus must be converted to metric units before it can be used in the sizing routine.

$$W_{wing}(lbs) = 0.036 \cdot {S_{wing_{FT}}}^{0.758} \cdot (\frac{AR_{wing}}{cos^2\Lambda_{C/4}})^{0.6} \cdot q^{0.006} \cdot \lambda^{0.04} \cdot (\frac{100 \cdot t/c}{cos\Lambda_{C/4}})^{-0.3} \cdot (n_z W_O)^{0.49} \quad (3.28)$$

**Reference fuselage mass**

The fuselage mass can be estimated using class 2 correlations, relating the geometry of the fuselage to its weight. The fuselage geometry is mainly determined by the seating arrangement and number of passengers. For the reference aircraft, the fuel tank volume does not influence the size of the fuselage, since the fuel is assumed to be stored in the wing. The fuselage in this methodology is assumed to be a tubular fuselage. Table 3.7 shows the relation between the fuselage diameter and the number of seats abreast [36].

Table 3.7: Fuselage diameter

| Seats abreast [-] | Fuselage diameter $D_{fus}$[m] |
|---|---|
| 2 | 1.85 |
| 3 | 2.19 |
| 4 | 2.7 |

Once the fuselage diameter has been specified by the seating arrangement, the length of the fuselage is determined by 3 different factors; the nose, tail and cabin lengths.

Equation 3.29 shows the relation between the fuselage diameter and the length of the nose through the fineness ratio. Equation 3.30 shows the same procedure for the length of the tail.

$$L_{nose} = D_{fus}\, F_{nose} \quad (3.29)$$

$$L_{tail} = D_{fus}\, F_{tail} \quad (3.30)$$

The length of the passenger cabin section is given by Equation 3.31. $N_{pass}$ is the number of passengers, $N_{seat,abreast}$ is the number of seats abreast. These are multiplied by the seat pitch $L_{seat}$. Finally, the length of the door $L_{door}$ is added to make up the total length of the cabin $L_{cabin}$.

$$L_{cabin} = \frac{N_{pass}}{N_{seat,abreast}}\, L_{seat} + L_{door} \quad (3.31)$$

Finally, putting it all together, the total fuselage length is given by Equation 3.32.

$$L_{fuselage} = L_{nose} + L_{cabin} + L_{tail} \quad (3.32)$$

Following the geometrical definition, the weight of the fuselage can be estimated using Equation 3.33 by Raymer [13]. $S_{fus}$ is the fuselage wetted area, $n_z$ is the ultimate load factor, $W_O$ is the $MTOM$ in (lbs), $l_{HT}$ is the distance between the main and horizontal tail, $l_{FS}$ is the length of the fuselage structure and $d_{FS}$ is the fuselage structure diameter.

$$W_{fus}(lbs) = 0.052 \cdot S_{fus}^{1.086} \cdot (n_z \cdot W_O)^{0.177} \cdot l_{HT}^{-0.051} \cdot (\frac{l_{FS}}{d_{FS}})^{-0.072} \cdot q_{cruise}^{0.241} \quad (3.33)$$

It is given in imperial units, and must be converted to metric units before it can be used in the sizing routine.

**Miscellaneous OEM**

After the major reference component masses have been determined, the $OEM_{misc}$ is calculated using Equation 3.34.

$$OEM_{misc} = OEM_{ref} - m_{wing_{ref}} - m_{pt_{ref}} - m_{fus_{ref}} - m_{tank_{ref}} \quad (3.34)$$

This miscellaneous operating empty mass represents components such as landing gear, tail structures and internal furnishings which will be similar for the hydrogen fuel cell aircraft. This furthermore takes into account the empirical behaviour captured using class 1 aircraft sizing. Once this $OEM_{misc}$ has been determined, the sizing routine for the hydrogen fuel cell aircraft is performed.

## 3.4. Hydrogen fuel cell aircraft sizing

After the determination of the $OEM_{misc}$, it is possible to size the hydrogen fuel cell aircraft. This is done using the reverse process, building up the masses of the aircraft from the $OEM_{misc}$ using class 2 estimations for the essential aircraft components.

Within this sizing routine, there are two iterative procedures for calculating the finally sized aircraft and the corresponding component masses. The routine is shown as a flowchart in Figure 3.6.

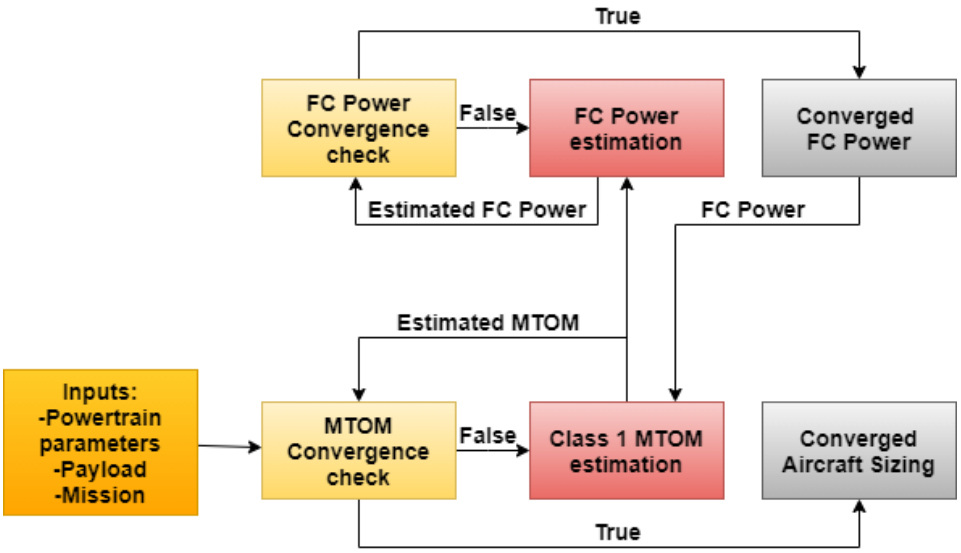


Figure 3.6: Hydrogen fuel cell aircraft sizing flowchart

In the outer iterative loop, an assumption of the $MTOM$ is used to determine the component weights of major components, such as the wing and fuselage mass. In the inner loop, this $MTOM$ is used to determine the power requirements of the power system. The power system is sized according to the highest power requirement, as specified by the constraint diagram. This powertrain power will determine the mass of the powertrain, which will influence the $MTOM$ of the aircraft. The iteration loops are run until there is convergence on both the hydrogen powertrain power and the MTOM.

The iterative loop for the $MTOM$ is required because an increase in powertrain mass influences the sizing of all other components as well.

The iterative loop for the fuel cell powertrain is required because the fuel cell must also produce power to drive the cooling and compressor system, whose power demand depends on the fuel cell power.

### 3.4.1. Fuel cell powertrain sizing

The sizing of the hydrogen fuel cell powertrain consists of sizing the power system according to the power requirements, and then extracting the mass of the powertrain using specific power estimates as inputted. The powertrain mass depends on the power system specific power. In this case, the powertrain mass includes all components that transform the fuel energy into useful propulsion energy.

As explained in Chapter 2, the fuel cell powertrain consists of several essential components. The heart of the fuel cell is the fuel cell stack, in which the hydrogen and oxygen electrochemically react and produce useful power and heat. However, to operate efficiently, additional components are required, the Balance of Plant (BoP). The balance of plant includes compressors, heat exchangers and auxiliary components to ensure proper fuel cell condition and operation.

In addition, an electric power distribution system is required, as well as electric motors to transform the electrical energy produced by the fuel cell into shaft power for the propellers. Choosing a higher technology level allows for the evaluation of future fuel cell aircraft concepts and their viability.

The hydrogen fuel cell power system is shown in Figure 3.7. In this Figure, the green boxes represent parts of the powertrain that have been modeled, including their masses, efficiencies and powers. The red box represents the heat exchanger, whose mass is taken into account. The blue box is the

hydrogen supply, which is discussed in Section 3.4.2. Lastly, the grey boxes represent parts of the powertrain that have not been modeled explicitly. The fuel cell and balance of plant have been highlighted by the dotted line.

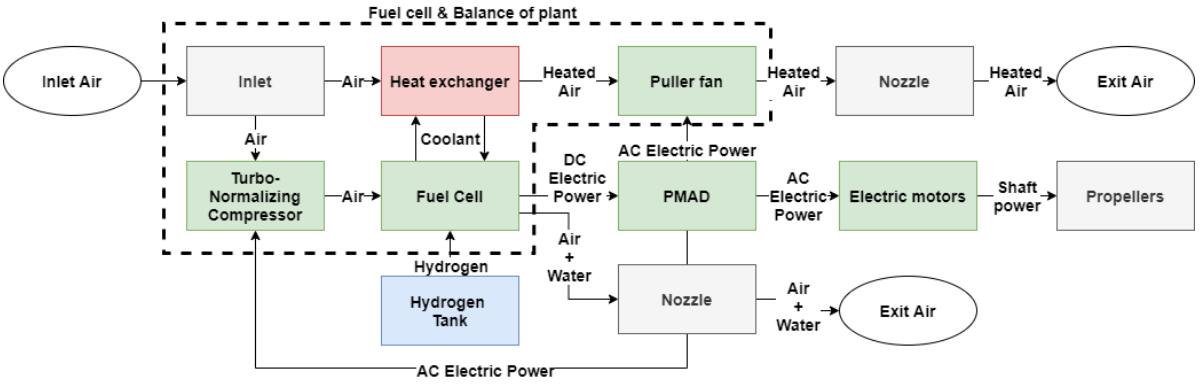


Figure 3.7: Hydrogen fuel cell powertrain diagram

To size the powertrain, the power, the mass and the geometry of the relevant components is estimated and discussed in the following sections.

**Fuel cell powertrain power**

To estimate the power of the entire powertrain, the shaft power for flight required is determined from the constraint diagram and the $MTOM$ estimate. This is the power that the propulsion system must produce, as shown in Equation 3.35.

$$P_{shaft} = MTOM \cdot g \cdot P/W \tag{3.35}$$

The propulsive efficiency $\eta_{prop}$ has already been taken into account when defining the constraint diagram, and as such is not necessary for determining the power requirements of the aircraft in the rest of the methodology.

As the fuel cell produces power electrically, this power must be converted to shaft power. To do this, the electric power passes through the power management and distribution system (PMAD) and the electric motors, where the electric power is converted to mechanical shaft power to turn the propellers. Taking into account the efficiencies of both the PMAD and electric motors, the net electrical output power that the fuel cell power system must produce is given by Equation 3.36.

$$P_{electric_{net}} = \frac{P_{shaft}}{\eta_{PMAD} \cdot \eta_{em}} \tag{3.36}$$

The efficiencies of the PMAD and electric motors are inputs to this analysis and are assumed to be constant. Using Equation 3.36, the net electrical output of the fuel cell to drive the propellers is determined. However, the fuel cell also needs to produce power for two other purposes: the cooling system (fan and pump) and the turbo normalizing compressor. To account for the difference in net and gross power the fuel cell must produce, Equation 3.37 is used:

$$P_{FC} = P_{electric_{net}} + P_{comp} + P_{cooling} \tag{3.37}$$

The power for the cooling system consists of two sources. The cooling system fan is used to draw air through the fuel cell heat exchanger, always ensuring adequate cooling, while the coolant pump ensures the coolant is circulated between the heat exchanger and the fuel cell.

The compressor normalizes the entering air pressure at altitude, allowing the fuel cell to operate at atmospheric conditions throughout the flight envelope. Both the compressor and cooling power depend on the fuel cell power, and thus the iterative loop as shown in Figure 3.6 is used to converge on the final fuel cell power. Both of these power contributions are discussed in the next paragraphs.

**Turbo-normalizing compressor power** The compressor is used to ensure the fuel cell operates under sea level pressure conditions throughout the flight. As reduced operating pressure has a detrimental effect on fuel cell performance, a compressor is used to supply it with 1 bar atmospheric pressure. This is known as a turbo-normalizing compressor.

The compressor power is determined by the temperature rise caused by the compression of the air, and the amount of airflow through the compressor. The temperature rise is calculated using the pressure ratio (PR) the compressor must produce. As this compressor is meant to be turbo-normalizing, the pressure ratio is related to altitude directly. Furthermore, it is assumed that there is an added 5% pressure drop through the fuel cell. This is shown in Equation 3.38, where $PR_{comp}$ is the compressor pressure ratio, $P_{SL}$ is the pressure at sea level and $P_{alt}$ is the pressure at the given altitude.

$$PR_{comp} = \frac{P_{SL}}{P_{alt}} \cdot 1.05 \tag{3.38}$$

This pressure ratio, along with the compressor polytropic efficiency $\eta_{comp}$, is used to determine the temperature rise of the incoming air. In Equation 3.39, $T_{t_2}$ is the total temperature after the compressor, $T_{t_1}$ is the total temperature before the compressor, $\eta_{comp}$ is the compressor polytropic efficiency, $PR_{comp}$ is the compressor pressure ratio and $\gamma$ is the ratio of specific heats for air (heat capacity ratio).

$$T_{t_2} = T_{t_1} \cdot (1 + (\frac{1}{\eta_{comp}}) \cdot (PR_{comp})^{(\frac{\gamma-1}{\gamma}-1)} \tag{3.39}$$

The next step towards calculating the compressor power is determining the mass flow of the air. This can be calculated from the power the fuel cell must produce, along with its efficiency and stoichiometric ratio ($\lambda_{O_2}$). $\lambda_{O_2}$ is the ratio of oxygen supplied versus the oxygen necessary for the electrochemical reaction with hydrogen. This is commonly between 1.5 and 2.0 to ensure the entire fuel cell has sufficient oxygen partial pressure, resulting in optimal performance [21]. The calculation of the air mass flow is shown in Equation 3.40.

$$\dot{m}_{air} = 2.856 \times 10^{-7} \cdot \lambda_{O_2} \cdot \frac{P_{FC}}{\eta_{FC}} \tag{3.40}$$

Finally, Equation 3.41 shows the power required to drive the compressor. $C_{p,air}$ is the heat capacity of the air. Since the compressor is driven by an electric motor, the electric motor efficiency $\eta_{em}$ is also included.

$$P_{comp} = \dot{m}_{air} \cdot C_{p,air} \cdot (T_{t_2} - T_{t_1})/\eta_{em} \tag{3.41}$$

The compressor is sized for the most demanding part of the mission, the top of the climb segment, where the pressure ratio of the turbo-normalizing compressor is the highest, and the airflow is maximum due to the power demand of the fuel cell.

**Cooling system power** The cooling system power requirement is determined by two factors, the cooling fan and the coolant pump. The cooling fan draws air through the heat exchanger to provide cooling, while the coolant pump ensures the cooling fluid is circulated between the heat exchanger and the fuel cell. First of all, the waste heat power rejected by the fuel cell is given by Equation 3.42.

$$P_{heat,rejected} = (\frac{1}{\eta_{FC}} - 1) \cdot P_{FC} \tag{3.42}$$

The cooling system is sized to dissipate this waste heat to the atmosphere. The cooling system power is determined by the optimized values obtained by NASA [32]. In the cited NASA paper, an optimization was performed which resulted in a relationship between the heat power to be rejected by the cooling system, and the cooling system power, mass and thrust. An important assumption is that the cooling fan always ensures positive pressure at the exit of the cooling channel, thus preventing backwards flow and even producing thrust. The influence of this cooling thrust is explored in Section 3.7. However, for the main methodology, the cooling system is assumed to add zero net drag/thrust.

The equations are reproduced here for clarity. Equation 3.43 calculates the power required for the cooling system. This includes the power demand for both the cooling fan and the coolant pump. To

account for other temperature differences than the one used in the original optimization, a correction factor is introduced, shown in Equation 3.44.

$$P_{cooling,system} = (0.371 \cdot P_{heat,rejected} + 1.33) \cdot f(dT) \tag{3.43}$$

$$f(dT) = 0.0038 * (\frac{T_{air}}{dT})^2 + 0.0352 * \frac{T_{air}}{dT} + 0.1817 \tag{3.44}$$

The cooling of the PMAD and electric motors is assumed to be incorporated in their respective specific powers. As mentioned earlier, the cooling system is assumed to produce net zero thrust/drag due to the action of the cooling fan pulling the air through the radiator.

**PMAD and Electric motor power** The power the PMAD must distribute is the same as the fuel cell power, as shown in Equation 3.45.

$$P_{PMAD} = P_{FC} \tag{3.45}$$

The power requirement for the electric motors is lower than the PMAD, due to the power requirements of the cooling system and turbo-normalizing compressor. and due to the imperfect efficiency of the PMAD system. This is reflected in Equation 3.46, where the electric motor power is determined using the net electric power required and the PMAD efficiency

$$P_{em} = P_{electric_{net}} \cdot \eta_{PMAD} \tag{3.46}$$

It is also possible to determine the electric motor power using Equation 3.47, in which it is calculated using the shaft power required and the electric motor efficiency. The results from both equations are analogous.

$$P_{em} = \frac{P_{shaft}}{\eta_{em}} \tag{3.47}$$

**Iterative loop fuel cell power**
As can be seen, the fuel cell gross power, turbo-normalizing compressor power and cooling system power demands are all dependant on one another. Due to this, an iterative loop is required, in which convergence on a suitable fuel cell gross power is determined. Once this loop is converged, the individual power contributions for all powertrain components can be determined in the next steps. The iterative loop is shown as the top loop in Figure 3.6.

**Fuel cell powertrain geometry**
The sizing methodology is meant for the conceptual design stage. As such, it is assumed that the size of the fuel cell powertrain takes up a similar volume to the conventional powertrain of a kerosene powered aircraft. This means that the powertrain fits into the volume of a conventional nacelle and wing, and as such no extra considerations in relation to powertrain volume and geometry are presented. However, the volume and geometry of the hydrogen tank itself are explored, as that does add a significant volume when compared to conventional power systems. In conventional aircraft, the wing is filled with fuel. However, for hydrogen powered aircraft the hydrogen fuel is stored in the fuselage. Thus, the wing box is empty, and the volume taken up by the fuel cells can be placed here, in addition to the volume available in the standard engine nacelle.

**Fuel cell powertrain mass**
Once the power requirement for each component of the fuel cell powertrain has been determined, the masses of the components are calculated using the equations below. For the fuel cell stack itself, the mass is determined using the specific power from the powertrain input parameters ($\hat{\rho}_{FC}$), as shown in Equation 3.48.

$$m_{FC} = \frac{P_{FC}}{\hat{\rho}_{FC}} \tag{3.48}$$

The turbo normalizing compressor mass is determined using Equation 3.49, making use of the specific power input $\hat{\rho}_{comp}$.

$$m_{comp} = \frac{P_{comp}}{\hat{\rho}_{comp}} \tag{3.49}$$

The cooling system mass is determined using Equation 3.50, as adapted from the cited NASA study[32]. Equation 3.42 and Equation 3.44 are used to determine $P_{heat,rejected}$ and $f(dT)$ respectively.

$$m_{coolingsystem} = (0.194 * P_{heat,rejected} + 1.39) * f(dT) \tag{3.50}$$

The PMAD mass is determined using Equation 3.51, relating the power that the PMAD must distribute to the specific power $\hat{\rho}_{PMAD}$.

$$m_{PMAD} = \frac{P_{PMAD}}{\hat{\rho}_{PMAD}} \tag{3.51}$$

Finally, the electric motor mass is calculated by Equation 3.52, relating the electric motor power to the specific power of the electric motors.

$$m_{em} = \frac{P_{em}}{\hat{\rho}_{em}} \tag{3.52}$$

The total mass of the powertrain is determined by the addition of the individual powertrain component masses. To take into account auxiliary components, mounting and cables, 20% extra is added to make up the total powertrain mass. This is shown in Equation 3.53.

$$m_{pt} = (m_{FC} + m_{comp} + m_{coolingsystem} + m_{PMAD} + m_{em}) \cdot 1.2 \tag{3.53}$$

This concludes the sizing of the fuel cell powertrain, now the hydrogen tank and other aircraft components must be sized.

### 3.4.2. Hydrogen tank sizing

For sizing the tank, first the fuel mass must be determined. After this, the tank geometry and mass can be estimated.

#### Hydrogen fuel mass

Take into account fuel cell powertrain efficiency, all the efficiencies that transform the hydrogen chemical energy to useful shaft power must be taken into account.

$\eta_{FC}$ describes the fuel cell efficiency, when generating the electrical power. As explained in Chapter 2, the fuel cell is more efficient at lower power levels. In the previous steps, the fuel cell has been sized for the maximum power demand. However, this maximum power demand is not required throughout the flight. Therefore, when lower power levels are required, for example during the cruise phase, the fuel cell efficiency increases. The power demand during the cruise phase can be determined using the constraint diagram $(P/W)_{cruise}$. The empirical model, which represents efficiency as a function of normalized power, presented in Section 2.3 in Figure 2.7, is used to characterize the influence of this reduced power demand on the fuel cell efficiency $\eta_{FC}$.

$\eta_{elec}$ takes into account the difference between the fuel cell output power and the electrical net power, as the compressor and cooling system reduce the net power available. This is shown in Equation 3.54.

$$\eta_{elec} = \frac{P_{electric_{net}}}{P_{FC}} \tag{3.54}$$

Finally, $\eta_{PMAD}$ and $\eta_{EM}$ describe the efficiencies of the PMAD and electric motors respectively.

$$\eta_{pt} = \eta_{FC}\, \eta_{elec}\, \eta_{PMAD}\, \eta_{em} \tag{3.55}$$

Once this powertrain efficiency $\eta_{pt}$ has been determined, the hydrogen fuel mass is calculated according to the same procedure as described in Section 3.3.1, but instead with the values appropriate for the hydrogen fuel cell powertrain. The fuel mass is used for calculating the tank volume and mass, as well as the aircraft mass breakdown. This will be explained in the the following section.

**Hydrogen tank geometry**

The geometry of the tank is determined using the volumetric storage efficiency $\eta_{vol}$. First of all, the volume of the hydrogen is determined according the fuel density and maximum fuel load in Equation 3.56. The mass of the hydrogen to be stored has been determined in the previous section, while the hydrogen density is determined by the storage method. The customer requirement energy source oversizing factor ($C_{oversize}$) describes the extra fuel possible to be carried in the tank, past the harmonic mission range.

$$V_{H_2} = \frac{m_{H_2} \cdot C_{oversize}}{\rho_{H_2}} \tag{3.56}$$

The hydrogen tank internal volume is equal to the volume of the hydrogen. The external tank volume is determined in Equation 3.57 using the volumetric storage efficiency $\eta_{vol}$ and the hydrogen volume $V_{H_2}$. The volumetric storage efficiency takes into account the thickness of the tank walls, caused by insulation and/or strong and lost volume from other components such as pumps and piping.

$$V_{tank_{ex}} = \frac{V_{H_2}}{\eta_{vol}} \tag{3.57}$$

The tank is assumed to be cylindrical, to be an integral part of the fuselage structure. Thus, the outer diameter of the tank structure will be the same as the fuselage. Equation 3.58 is used to determine the length of the hydrogen tank system. This length is taken into account when determining the geometry of the fuselage. $D_{fus}$ is the fuselage diameter.

$$L_{tank} = \frac{V_{tank_{ex}}}{\pi \cdot (\frac{D_{fus}}{2})^2} \tag{3.58}$$

This extra length is taken into account when sizing the fuselage, as will be explained in Section 3.4.4.

**Hydrogen tank mass**

To determine the mass of the hydrogen tank, Equation 2.2 is rewritten to solve for for the tank mass, shown in Equation 3.59. $m_{H_2}$ is the hydrogen required for the harmonic mission, and to allow for extra fuel to be stored in the tank, the tank size must be larger to reflect this choice.

$$m_{tank} = \frac{m_{H_2} \cdot C_{oversize}}{\eta_{storage}} - (m_{H_2} \cdot C_{oversize}) \tag{3.59}$$

### 3.4.3. Wing sizing

For the wing, both the geometry and the mass are determined using the methods described in the reference aircraft sizing, in Section 3.3.2

### 3.4.4. Fuselage sizing

The fuselage is sized to hold the passengers, cargo and the hydrogen tank.

**Fuselage geometry**

The sizing of the fuselage geometry follows the same steps as explained for the reference aircraft. However, as opposed to the reference aircraft sizing, the geometry of the hydrogen tank is taken into account. The length of the fuselage is increased by the inclusion of the hydrogen tank. The cylindrical hydrogen fuel tank is assumed to have the same diameter as the fuselage, and as such the tank cannot be specified to have a larger or smaller diameter.

The tank length $L_{tank}$ has been determined using Equation 3.58. Finally, putting it all together, the total fuselage length is given by Equation 3.60.

$$L_{fuselage} = L_{nose} + L_{cabin} + L_{tank} + L_{tail} \tag{3.60}$$

**Fuselage mass**

The mass of the fuselage is determined using the same equations as described in Section 3.3.2. As opposed to the reference conventional aircraft, the fuselage mass will be larger because of the elongated fuselage, caused by the need to house the voluminous hydrogen tank. The hydrogen tank is assumed to be an integral part of the fuselage, and thus load bearing. The mass of the fuselage is therefore only related to the geometry, and can be estimated using conventional formulas, such as Equation 3.33.

### 3.4.5. Aircraft mass

After the sizing of the components of the hydrogen fuel cell aircraft, the total aircraft mass can be determined. Equation 3.61 shows how the $OEM$ is determined from $OEM_{misc}$, as well as using class 2 mass estimation methods for the other mass contributions. Once again, the four main aircraft component groups are the powertrain, tank, wing and fuselage.

$$OEM = OEM_{misc} + m_{pt} + m_{tank} + m_{wing} + m_{fus} \tag{3.61}$$

Finally, Equation 3.62 shows the buildup of the aircraft $MTOM$, adding the payload and fuel masses to arrive at the final aircraft $MTOM$.

$$MTOM = OEM + m_{H_2} + m_{payload} \tag{3.62}$$

This $MTOM$ is used in the iterative loop shown in Figure 3.6 until there is convergence on both the $MTOM$ and the $P_{FC}$

## 3.5. Aerodynamic estimation

The last step in the methodology is to refine a set of important aerodynamic characteristics. These aerodynamic characteristics are used throughout the previous steps of the methodology for determining the constraint diagram and sizing of the aircraft. The resulting aircraft's aerodynamic characteristics must be consistent with the assumptions made throughout the methodology. Thus, an estimation of the most important aerodynamic coefficients is made. These are split into lift and drag estimations.

### 3.5.1. Lift estimation

For the estimation of the lift of the aircraft, the vortex lattice method is used. The vortex lattice method is a panel method which allows for the determination of the lift and lift induced drag for an arbitrary wing geometry. The vortex lattice method that is implemented is based on the methodologies as described in literature [37] [38] [39]

In the vortex lattice method, the wing is replaced with a lattice of panels, which follow the mean camber of the underlying airfoil. The panels are aligned with the the geometrical definition of each wing, taking into account features such as aspect ratio, sweep and taper ratio.

The vortex lattice layout for an example wing is shown in Figure 3.8. Each panel is assumed to have a bound vortex at its quarter chord line, while the control point is at the three quarter chord in the middle of the panel. The two trailing vortices extend along the free stream.

The strengths of the vortices on each panel can be used to determine the pressure distribution on the wing, which is used to determine the lift and induced drag coefficients.

To solve for the strengths of the vortices, several boundary conditions are imposed. The boundary conditions for the vortex lattice method are that no flow may pass through the panels, and that the airflow velocities at the trailing edge must be the same, the Kutta condition. Equation 3.63 shows the boundary condition describing the no flow condition through the panel. $V_\infty$ is the free stream velocity, $\theta$ is the angle of attack for the specific panel, taking into account airfoil camber if present, and $w_i$ is the induced flow component caused by the vorticity of the surrounding vortices.

$$V_n = 0 = V_\infty \, sin(\theta) + w_i \tag{3.63}$$

The induced flow component of panel i ($w_i$) is a function of the vorticity strength of panel j ($\Gamma_j$) and an influence coefficient $A_{i,j}$.

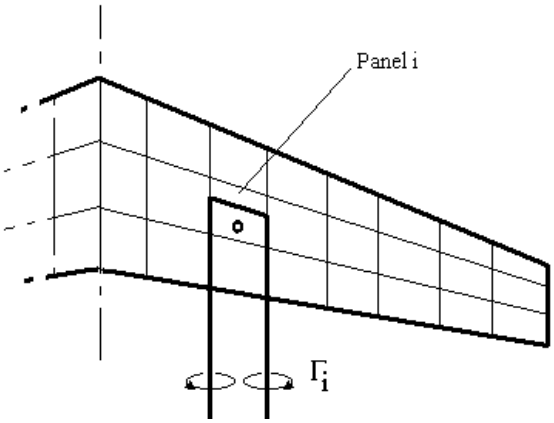


Figure 3.8: Vortex lattice [3]

$$w_i = \sum_{j=1}^{N} A_{i,j}\Gamma_j \tag{3.64}$$

Using these boundary conditions, the strength of each of the vortices in the lattice can be calculated.

Once the vortex strengths have been solved for, they can be used to extract the pressure distribution around the wings. These can be rewritten to describe the most important aerodynamic parameters, including the lift coefficient, induced drag coefficient and moment coefficients.

The total aircraft lift is estimated using a correction factor on the lift coefficient which is calculated for the wings. This correction factor mainly takes into account the extra lift produced by the fuselage. $k_{fuselage}$ is assumed to be 1.14 for these preliminary calculations [15].

$$C_{L_{total}} = C_{L_{wings}}\, k_{fuselage} \tag{3.65}$$

Once the vortex panels have been aligned with the aircraft wing definition, they can be visualized. The vortex panels for an example aircraft are shown in Figure 3.9.

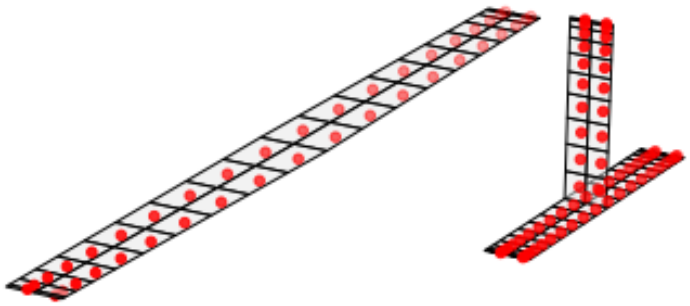

Figure 3.9: Example vortex lattice panels

As can be seen, only the main wing and tail surfaces are considered for this analysis. The contribution of the fuselage and to the lift of the aircraft is taken into account by a correction factor.

For each wing, there are 10 panels in the span-wise direction and 2 panels in the chord-wise direction. For a symmetrical wing there are thus 40 panels to consider. This is the case for the main wing and the horizontal tail, while the vertical tail is non symmetric, and thus has 20 panels. This is a relatively low amount of panels, however for conceptual analysis it is deemed to be sufficient.

[3] http://www.aerodynamics4students.com/subsonic-aerofoil-and-wing-theory/3d-vortex-lattice-method.php [Accessed 09-02-2021]

The vortex lattice method makes use of several important assumptions and limitations, which must be taken into account when considering the validity of the results.

- The effect of airfoil thickness is not taken into account, as the airfoil is assumed to be infinitely thin.
- The vortex lattice method is able to consider an airfoil with camber, however as used in this methodology, a symmetrical airfoil is considered.
- The flow field assumed to be incompressible. As such it is only suitable for subsonic aircraft under approximately M < 0.4.
- The flow is assumed to be inviscid. As such there is no modeling of boundary layer or boundary layer effects. This limits the applicability of this model to moderate angles of attack, away from the stall condition.
- The vortex lattice method as utilized here does not take into account the presence of the propellers wash over the wings. The influence of the fuselage on the lift is also not taken into account directly, but rather through a correction factor.

### 3.5.2. Drag estimation

The drag of the aircraft is made up of several components. For the subsonic aircraft considered in this methodology, the lift induced and parasite drag are the most important contributors to aircraft drag.

The parasite drag of the aircraft is calculated by estimating the wetted area of the aircraft. This includes the fuselage, main wing, tail and propulsion elements. These can be constructed from the geometrical definition as described earlier using the inputs and preliminary results of the methodology. The parasite drag is calculated using Equation 3.66.

$$C_{D_p} = k\ C_f\ S_{ref} \tag{3.66}$$

In Equation 3.66, $C_{D_p}$ is the parasite drag, $k$ is the form factor, $C_f$ is the skin friction coefficient and $S_{ref}$ is the reference area. The form factor $k$ is specific to the specific component, for example the wing or fuselage. The contributions from all exposed surfaces are grouped to result in the final parasite drag coefficient.

The lift induced drag can be calculated using the vortex lattice method as described in the previous section.

Once these calculations have been performed, the aerodynamic parameters of interest, the minimum drag coefficient $C_{D_{min}}$ the lift to drag ratio $L/D$ and the lift induced drag constant $k$, can be extracted. These aerodynamic coefficients are led back into the first step of the methodology, and used for a more refined sizing estimate.

## 3.6. Full loop tool integration

These three aerodynamic parameters are essential in determining the aircraft sizing during the earlier steps of the methodology. For example, the lift to drag ratio is used to determine the amount of fuel required for the mission through the Breguet range equation (Example: Equation 3.9), while the minimum drag coefficient and lift induced drag constant are used in the constraint diagram calculation (Example: Equation 3.2).

The revised estimations are thus used to determine a more accurate estimate for the aircraft sizing and performance. This process is repeated in a loop, until there is convergence on these aerodynamic parameters, and the $MTOM$ of the entire aircraft. This ensures that the final aircraft design is feasible and consistent.

To show how the methodology converges on a final aircraft design, Figure 3.10 shows the convergence on the $MTOM$ of an example aircraft.

## 3.7. Cooling thrust influence

In the current methodology, the cooling thrust produced by the cooling system is assumed to be zero, even though additional power is required to drive the fan. Due to the large amount of heat power that is

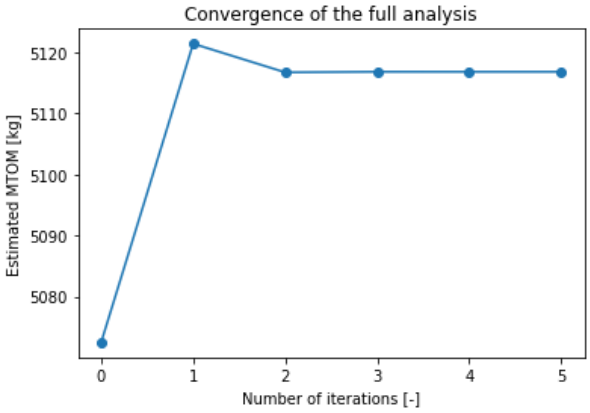


Figure 3.10: Example Convergence graph

rejected through the cooling system in combination with the cooling fan pulling air through the radiator, a certain thrust is predicted by the cited NASA report [32].

This section explores the influence that such an extra thrust contribution would have on the sizing methodology.

In the first step of the methodology, the shaft power to weight and wing loading requirements are determined. However, this does not take into account multiple sources of thrust or power. The constraint diagram calculation must be altered to take into account both the thrust from the main propulsion system and the cooling system thrust. If the cooling system produces a significant amount of thrust (more than 10% for example), this thrust does not need to be generated by the main powertrain. Thus, the powertrain can be sized for a lower power, reducing powertrain mass.

The equations that govern the cooling thrust must be rewritten in a form that allows for the integration with the $T/W$ or $P/W$ ratio as a function of wing loading. This procedure will be shown below for the cruise condition. The other flight conditions would follow a similar strategy. This procedure will first determine the $T/W$ contribution of the cooling system.

The cruise condition thrust to weight ratio is given by equation 3.67 [12].

$$\frac{T}{W} = qC_{D_{min}}\left(\frac{1}{W/S}\right) + k\left(\frac{1}{q}\right)\left(\frac{W}{S}\right) \tag{3.67}$$

The equation that describes the cooling thrust as a function of rejected heat power is Equation 3.68 [32].

$$T_{uncorrected} = 5.878 * P_{heat,rejected} + 27.58 \tag{3.68}$$

These values represent the heat exchanger design for a particular temperature difference between the ambient and the rejected heat. To compensate for differences in this temperature gradient, a temperature correction factor is introduced in Equation 3.69 [32].

$$f(dT) = 0.0038 * \left(\frac{T_{air}}{dT}\right)^2 + 0.0352 * \frac{T_{air}}{dT} + 0.1817 \tag{3.69}$$

Now that the basic equations have been introduced, the first step is to rewrite equation 3.68 to result in $T/W$, by dividing both sides by the weight. This step is shown in Equation 3.70.

$$\frac{T_{cooling}}{W} = \left(5.878 * \frac{P_{heat,rejected}}{W} + \frac{27.58}{W}\right) * f(dT) \tag{3.70}$$

The term $\frac{27.58}{W}$ can be disregarded because of its small contribution. To determine $\frac{P_{heat,rejected}}{W}$, it is necessary to determine the $P_{heat,rejected}$. This is done using Equation 3.71, where $\eta_{FC}$ is the fuel cell efficiency and $P_{FC}$ is the fuel cell power.

$$P_{heat,rejected} = \left(\frac{1}{\eta_{FC}} - 1\right) P_{FC} \tag{3.71}$$

By dividing both sides of Equation 3.71 by the weight $W$, the $\frac{P_{heat,rejected}}{W}$ can be solved for using equation 3.72,

$$\frac{P_{heat,rejected}}{W} = (\frac{1}{\eta_{FC}} - 1)\frac{P_{FC}}{W} \tag{3.72}$$

The fuel cell efficiency $\eta_{FC}$ is assumed to be a fixed input. The fuel cell power to weight ratio $\frac{P_{FC}}{W}$ can be solved for by determining what power the fuel cell must produce. As discussed earlier in this chapter, the fuel cell produces the shaft power for flight, the compressor power to provide ambient pressure to the fuel cell, and the cooling system power.

As in the main methodology, Equation 3.73 shows how the thrust to weight ratio can be transformed to a power to weight ratio by taking into account the velocity $V$ and propulsive efficiency $\eta_{prop}$:

$$\frac{P_{shaft}}{W} = \frac{T}{W}\frac{V}{\eta_{prop}} \tag{3.73}$$

$$\frac{P_{FC}}{W} = (\frac{P_{shaft}}{W}/\eta_{PMAD}/\eta_{em}) + \frac{P_{comp}}{W} + \frac{P_{cooling}}{W} \tag{3.74}$$

$\frac{P_{comp}}{W}$ is assumed to be 5% of the total fuel cell power as a first assumption. $\frac{P_{cooling}}{W}$ can be determined with equation 3.75 [32].

$$\frac{P_{cooling}}{W} = 0.371 * \frac{P_{heat,rejected}}{W} + \frac{1.33}{W} \tag{3.75}$$

The term $\frac{1.33}{W}$ can be disregarded because of its small contribution. The above mentioned formulas need to be solved in an iterative loop, as the cooling fan power, the heat rejected and the fuel cell power are all dependant on each other. In addition to that, another loop is required to account for the correct $\frac{P_{shaft}}{W}$. The iterative loops are shown in Figure 3.11.

Once the cooling system thrust contribution $\frac{T_{cooling}}{W}$ has been calculated, the remainder of the required $\frac{T_{original}}{W}$ is determined. This is the remaining thrust to weight fraction $\frac{T}{W}$ that must be produced by the main propulsion system. From this, the shaft power thrust contribution can be determined. Equation 3.76 shows how the $\frac{T_{shaft}}{W}$

$$\frac{T_{shaft}}{W} = \frac{T_{original}}{W} - \frac{T_{cooling}}{W} \tag{3.76}$$

In Equation 3.77, the $\frac{T_{shaft}}{W}$ is transformed to the $\frac{P_{shaft}}{W}$.

$$\frac{P_{shaft}}{W} = \frac{T_{shaft}}{W} * \frac{V}{\eta_{prop}} \tag{3.77}$$

This new $\frac{P_{shaft}}{W}$ can be inputted to the loop to calculate a new value until both loops converge on a new required $\frac{P_{shaft}}{W}$. Figure 3.11 shows the calculation procedure as a flowchart.

The influence of this cooling thrust on the constraint diagram is shown the results in Chapter 6.

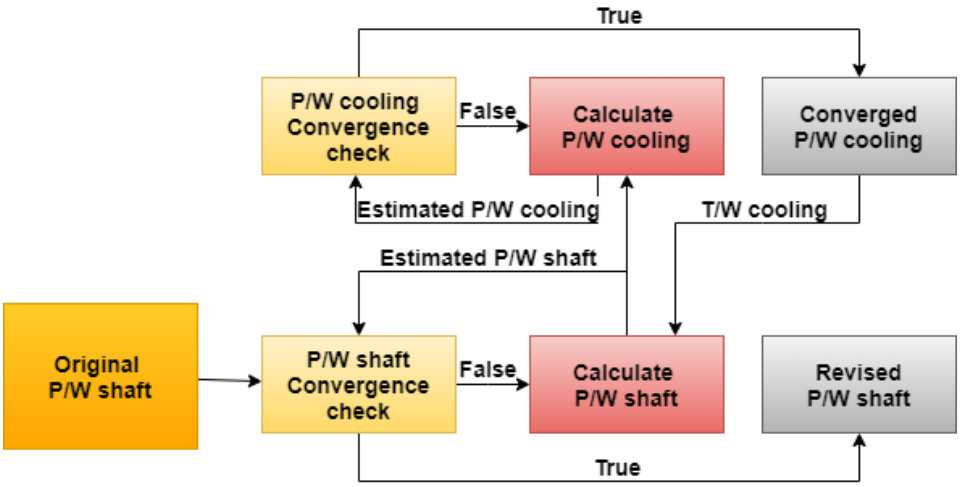


Figure 3.11: Proposed cooling thrust contribution calculation

## 3.8. Overview of the hydrogen fuel cell sizing results

This section provides a short overview of the results this part of the sizing methodology results in. These are roughly split into component and system level results.

### 3.8.1. Component level results

Because of the component sizing performed for several important powertrain and aircraft components, it is possible to extract more detailed component level information. These include:

- Power requirements of components
- Mass of powertrain components
- Geometry of components

### 3.8.2. System level results

The system level results of the sizing methodology include:

- Total aircraft mass
- Aircraft planform geometry
- Payload-Range diagram
- Planform diagram

This concludes the modified class 1 mass estimation routine of the aircraft, which also has resulted in preliminary sized powertrain components, as well as the full aircraft.

# 4

# Implementation

In this chapter, the methodology as presented in Chapter 3 is implemented in the HAPPIE tool (Hydrogen Aircraft Power & Propulsion Initial Estimator), and integrated with the SUAVE (Stanford University Aerospace Vehicle Environment) mission analysis environment [15] [16]. HAPPIE is used for the the sizing of the aircraft, while SUAVE is used for the calculation of the revised aerodynamic estimation. The mission analysis performed in SUAVE also generates mission performance results for the harmonic mission.

## 4.1. HAPPIE

The first 4 steps of the methodology have been integrated into the HAPPIE tool. The HAPPIE tool implements the same steps as described in the methodology, and visualizes them in a graphical user interface. A screenshot of the GUI is shown in Figure 4.1.

The left part of the GUI is dedicated to the inputs, while the right part shows the results. The input parameters have been divided into the same categories as described in Chapter 3. Each of the parameter values can be easily altered using the text input boxes. Once the desired input values have been entered, the analysis can be run. The tool allows for the analysis to the full methodology loop, in which case SUAVE is consulted for the revised aerodynamic estimate. If this is not required, for example if the user wants to manually select the aerodynamic coefficients, it is also possible to do a single analysis without the convergence on the aerodynamic parameters.

The results are shown on the right of the GUI. These include component specifications such as mass, power and geometries, as well as important ratios. The bar chart visually shows the mass breakdown of the aircraft. On the top right the constraint diagram is shown, while the payload range diagram and planform diagrams are shown in the bottom two figures. This visualization of several important results provides useful and convenient feedback to the user of the tool.

The results that are generated using SUAVE, as well as results such as the sensitivity analysis are plotted in a separate window to reduce the clutter of the GUI. It is also possible to import and export the inputs and results that the analysis produces. This is done using an .XML file, with the data being structured according to the input categories and the results. This allows for the quick analysis of multiple concepts and easy access to previous results.

The HAPPIE tool is used to generate the results and validation discussed in the Chapter 5 and Chapter 6.

## 4.2. SUAVE mission analysis

The last part of the methodology consists of a mission analysis using SUAVE (Stanford University Aerospace Vehicle Environment). SUAVE is an open source conceptual design environment, which allows for the analysis of novel aircraft concepts. SUAVE performs an analysis of the harmonic mission, and makes use of several disciplines, including aerodynamics, stability & control and propulsion. A sample mission is flown by the generated design based on the customer mission requirements. An example of a mission analysed in the SUAVE environment is shown in Figure 4.2

To ”fly” the harmonic mission, the sizing results from the HAPPIE tool are used as inputs for the SUAVE mission analysis. These include the wing planform, fuselage geometry, $MTOM$ and powertrain parameters.

SUAVE is used to perform the aerodynamic refinement for $L/D$, $k$ and $C_{D_{min}}$. The procedure of how SUAVE performs these estimations was discussed in Chapter 3. These aerodynamic models are known as the fidelity zero models within the SUAVE package. More information on the exact procedure can be found in the SUAVE documentation [15]. There are a couple of steps that SUAVE performs during the aerodynamic calculation vortex lattice method which lead to a faster calculation.

After the vortex panel distribution has been defined, a surrogate is used. These vortex panels are put through a 'training', at different angles of attack and at different mach numbers.

By preemptively running the vortex lattice method for a set number of mach numbers and angles of attack, a polynomial can be generated and fitted. This polynomial can be referenced during the mission analysis, removing the need to run the full vortex lattice method for each point. This greatly speeds up the calculation. Instead of run times around 3.5 minutes, a single mission can be analysed within 10 seconds on a desktop computer. This allows for much faster calculations to be performed, and reduces the time to run the entire loop to only 10 seconds. as the steps for calculating the constraint diagram and sizing for reference and hydrogen fuel cell aircraft are all significantly faster and require next to no computing time. After the SUAVE mission analysis has been performed, many different mission parameters can be extracted. These include aerodynamic performance, fuel use, and powertrain power throughout the mission.

## 4.3. Overview of the implementation

As explained earlier, two different levels of analysis are performed in the methodology. The sizing is done in the HAPPIE part of the tool, while the aerodynamic estimation and refinement is done in the SUAVE environment. By iterating between these two levels of fidelity, a convergent result is obtained for each aircraft. This iterative procedure is shown in Figure 3.1.

The main difference between the mission analysis in SUAVE and the equations used in the modified mass estimation, is the fact that the mission analysis consists of many points throughout the mission. For example, the mass estimation makes use of the Breguet range equation to estimate the fuel mass required for the mission. Meanwhile, in SUAVE, the power requirements during the flight segments are used in conjunction with the fuel cell model to estimate the fuel mass flow. The total fuel mass is therefore calculated by integrating the fuel mass flow over the entire mission.

A similar story is true for the estimation of the power required for flight. In the first steps of the methodology, the constraint diagram is constructed, which results in a power to weight ratio requirement for several flight segments. A power requirement can be calculated using the mass of the aircraft. In SUAVE, the power required is calculated for each flight segment individually. It is therefore a more in depth analysis.

The results between SUAVE and HAPPIE must be consistent for the results to be valid. A comparison for several important powertrain parameters is shown in Table 4.1, indicating an error between 3 and 21 %. This error range is caused by the two levels of fidelity. HAPPIE only performs single point aircraft performance calculations, while SUAVE performs a full mission analysis with multiple segments and points. This extra mission analysis information generated by the SUAVE mission analysis is used to validate that the assumptions made in the methodology are consistent with higher order methods.

Table 4.1: Example HAPPIE vs SUAVE convergent results

| | **HAPPIE** | **SUAVE** | **Error** [%] |
|---|---|---|---|
| Fuel mass $[kg]$ | 64.1 | 62.1 | 3.31 |
| Max $P_{shaft}$ $[kW]$ | 907.6 | 839.7 | 7.49 |
| Max $P_{FC}$ $[kW]$ | 1389.3 | 1228.6 | 13.08 |
| Max $P_{elec_{net}}$ $[kW]$ | 1120.5 | 1036.6 | 8.09 |
| Max $P_{comp}$ $[kW]$ | 56.2 | 46.6 | 20.75 |
| Max $P_{coolsystem}$ $[kW]$ | 212.6 | 175.5 | 21.11 |

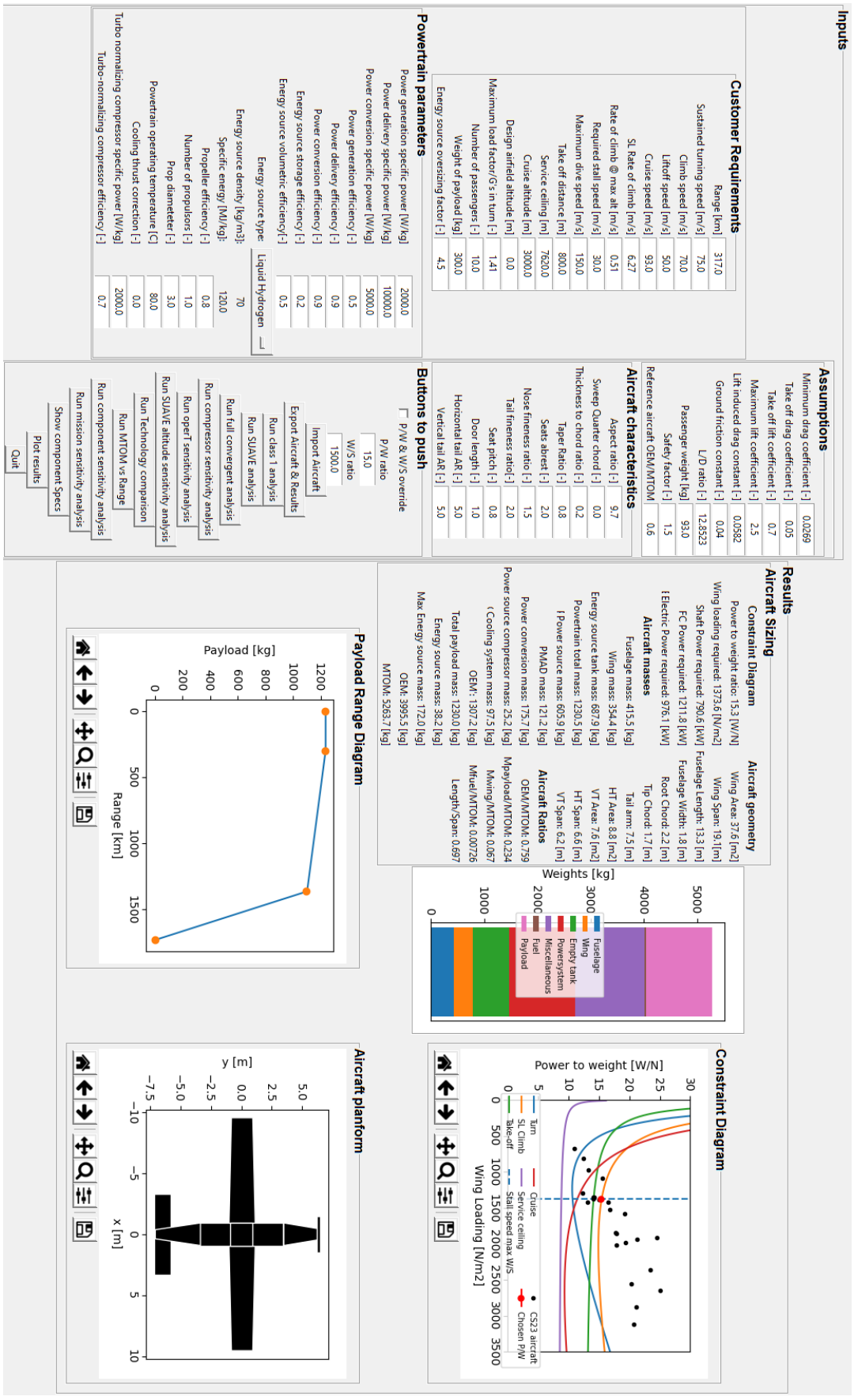


Figure 4.1: HAPPIE GUI

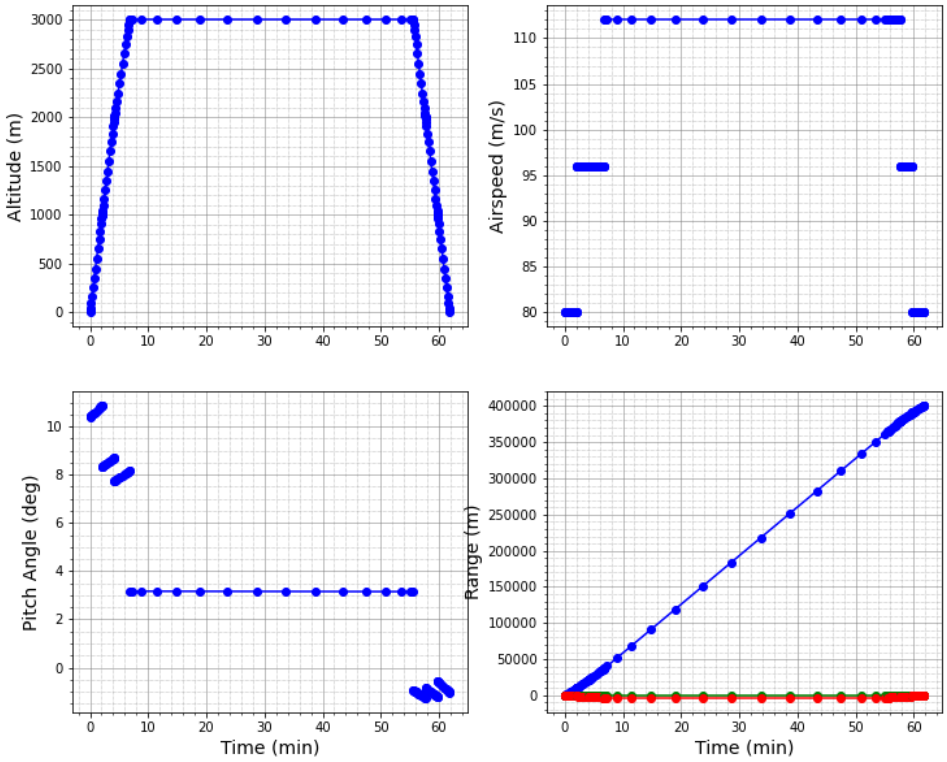


Figure 4.2: Example SUAVE mission results

# 5

# Validation

Before the methodology that has been presented in Chapter 3 is used to generate results, it must first be validated. As the methodology is general enough to allow for the analysis of conventionally powered aircraft, a relevant set of aircraft is used to validate and compare the sizing results produced by the methodology with empirical data. The considered aircraft represent the scope of the CS-23 aircraft category, including small piston engine leisure aircraft as well as commuter class 19-seater aircraft. Representing a leisure aircraft, the Cessna 172 is considered. Representing a medium sized multi purpose aircraft, the Cessna 208 Caravan is chosen. Finally, representing the upper limit of the CS-23 category, the Dornier Do 228 is discussed.

The aircraft are evaluated against several criteria:

1. Masses & Specifications
2. Aircraft Planform
3. Constraint diagram
4. Payload-Range diagram

The results for each aircraft will be discussed and preliminary conclusions on the validity of the methodology are subsequently drawn.

## 5.1. Cessna 172 Skymaster

The Cessna 172 Skymaster is a very popular recreational aircraft which seats 4 people. It is powered by a single piston engine running on aviation fuel. It represents the recreational segment of the CS-23 aircraft category. Figure 5.1 shows the aircraft in question.

Figure 5.1: Cessna 172 [1]

[1] https://cessna.txtav.com/-/media/cessna/images/aircraft/piston/skyhawk/exterior-360/2019-exterior-360/skyhawk-360_16.ashx [Accessed 25-01-2021]

### 5.1.1. Cessna 172 Inputs

The most relevant input parameters are shown in Table 5.1. A full list of the inputs is presented in Appendix A. The inputs are derived from the manufacturers specifications. [2]

Table 5.1: Cessna 172 input parameters

| Parameter | Value |
|---|---|
| Range $R$ $[km]$ | 752 |
| Cruise speed $V_{cruise}$ $[m/s]$ | 62.8 |
| Rate of climb $V_v$ $[m/s]$ | 3.71 |
| Cruise altitude $h_{cruise}$ $[m]$ | 3658.0 |
| Payload mass $m_{payload}$ $[kg]$ | 308 |
| Tank oversizing factor $C_{oversize}$ $[-]$ | 1.3 |
| Maximum lift coefficient $C_{L_{max}}$ $[-]$ | 2 |

Table 5.2 shows the aerodynamic coefficients that have been estimated by SUAVE in the last step of the methodology.

Table 5.2: Cessna 172 aerodynamic parameters

| Parameter | Value |
|---|---|
| $C_{D_{min}}$ | 0.0396 |
| $L/D$ | 10.56 |
| $k$ | 0.072 |

### 5.1.2. Cessna 172 sizing results

Table 5.3 shows the sizing results for several key parameters of the aircraft. These results are compared with publicly available empirical data [40]. Both the $MTOM$ and $OEM$ are predicted within 10%. The maximum fuel mass is a function of the fuel mass required for the harmonic mission and is predicted within 5%. The prediction of the wing loading 5%. The power to weight ratio is slightly overestimated.

Table 5.3: Cessna 172 sizing comparison

| Parameter | Reference | HAPPIE sizing | Difference [%] |
|---|---|---|---|
| $MTOM$ $[kg]$ | 1160.0 | 1250.5 | 7.8 |
| $OEM$ $[kg]$ | 762.0 | 827.7 | 8.62 |
| Max $m_{fuel}$ $[kg]$ | 144.0 | 149.2 | 3.61 |
| $W/S$ $[N/m^2]$ | 703.7 | 744.3 | 5.77 |
| $P/W$ $[W/N]$ | 11.8 | 11.9 | 0.85 |

Figure 5.2 shows the generated planform diagram of the aircraft, with the main geometrical features. Due to the specification of a tube and wing style aircraft, this does not completely match the geometry of the actual aircraft. However, the size of the wing and fuselage are generally similar.

Figure 5.3 shows the generated constraint diagram of the aircraft, with the red point representing the chosen $P/W$ and $W/S$. As can be seen when evaluating the chosen $P/W$ and $W/S$ combination, this Cessna 172 has relatively low wing loading and power to weight ratio requirements when compared to other aircraft in the CS-23 category. This is mainly due to the limited performance requirements for this aircraft, as well as the low stall speed. The chosen point is constrained by the stall speed and climb requirements.

Finally, the payload range diagram comparison is shown in Figure 5.4. The second point, which represents the harmonic mission, lines up closely to the documentation. However, at increasing ranges and reduced payloads, the documentation for the Cessna 172 no longer represents a classic payload-range diagram, and thus the lines diverge.

[2] `https://cessna.txtav.com/en/piston/cessna-skyhawk` [Accessed 02-02-2021]

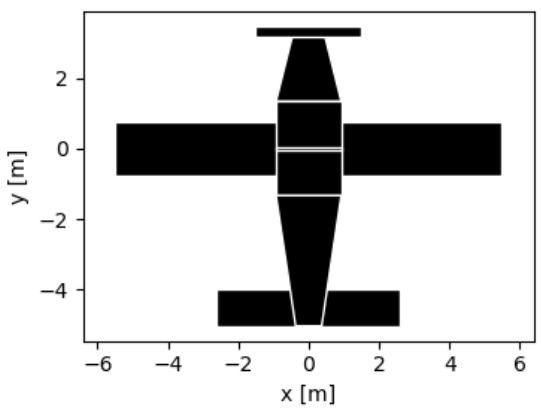


Figure 5.2: Cessna 172 planform diagram

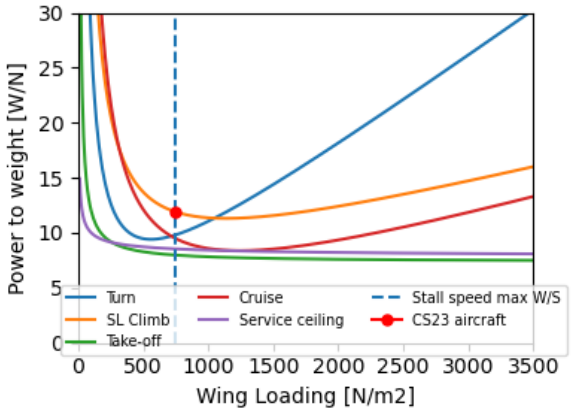


Figure 5.3: Cessna 172 constraint diagram

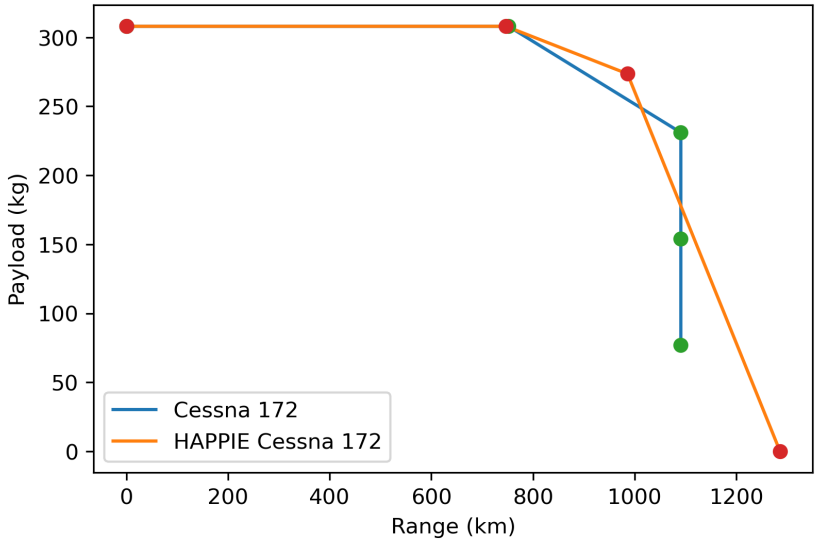


Figure 5.4: Cessna 172 Payload Range diagram comparison

## 5.2. Cessna 208 Caravan

The Cessna 208 Caravan is a representative aircraft for the middle of the CS-23 category. It is a single engine turboprop running on kerosene. It is able to transport 10 passengers or cargo, and is a very versatile platform. There are many types and configurations of the Cessna 208 Caravan. Figure 5.5 shows an example of the configuration that is considered for this analysis.

### 5.2.1. Cessna 208 Inputs

The most relevant input parameters are shown in Table 5.4. These have been obtained or estimated using the manufacturers data sheets [4].

Table 5.5 shows the aerodynamic parameters that have been estimated using the SUAVE step in the methodology for the Cessna 208.

### 5.2.2. Cessna 208 sizing results

First of all, table 5.6 shows several key parameters for the Cessna 208 comparison [41]. The $MTOM$ and $OEM$ are predicted within 10 %. The maximum fuel load is not strongly predicted, but does not

[3] https://cessna.txtav.com/-/media/cessna/images/aircraft/turboprop/caravan/exterior-360/10_2019-exterior-360/caravan-360_16.ashx [Accessed 25-01-2021]

[4] https://cessna.txtav.com/en/turboprop/caravan [Accessed 02-02-2021]

Figure 5.5: Cessna 208 Caravan [3]

Table 5.4: Cessna 208 input parameters

| Parameter | Value |
|---|---|
| Range $R$ $[km]$ | 317 |
| Cruise speed $V_{cruise}$ $[m/s]$ | 95.5 |
| Rate of climb $V_v$ $[m/s]$ | 6.27 |
| Cruise altitude $h_{cruise}$ $[m]$ | 3000 |
| Payload mass $m_{payload}$ $[kg]$ | 1137 |
| Tank oversizing factor $C_{oversize}$ [–] | 4.5 |
| Maximum lift coefficient $C_{L_{max}}$ [–] | 2.2 |

Table 5.5: Cessna 208 aerodynamic parameters

| Parameter | Value |
|---|---|
| $C_{D_{min}}$ | 0.0286 |
| $L/D$ | 10.86 |
| $k$ | 0.0592 |

differ an order of magnitude. Furthermore, the predicted maximum amount of fuel does not exceed the maximum fuel mass volume available for the actual aircraft, which would pose a problem for the validity of the results. The wing loading prediction is accurate within 5%. The power to weight ratio is slightly over predicted by the methodology and the estimated inputs used.

Table 5.6: Cessna 208 sizing comparison

| Parameter | Reference | HAPPIE sizing | Difference [%] |
|---|---|---|---|
| $MTOM$ $[kg]$ | 3645 | 3284.3 | -9.9 |
| $OEM$ $[kg]$ | 2145 | 2025.7 | -5.56 |
| Max $m_{fuel}$ $[kg]$ | 1009 | 561 | -44.4 |
| $W/S$ $[N/m^2]$ | 1377.4 | 1323.7 | -3.9 |
| $P/W$ $[W/N]$ | 14.1 | 15.8 | 12.06 |

Figure 5.6 shows the generated planform diagram of the aircraft, with the main geometrical features.

Figure 5.7 shows the generated constraint diagram of the aircraft, with the red point representing the chosen $P/W$ and $W/S$. The Cessna 208 represents a middle sized CS-23 aircraft, and the wing loading and power to weight ratio both have increased when compared to the Cessna 172. This is due to the higher performance requirements of the aircraft, with the increased rate of climb being the main driving factor. The chosen $P/W$ and $W/S$ are constrained by the stall speed and climb requirements.

Finally, Figure 5.8 shows the payload range comparison between the generated aircraft and the

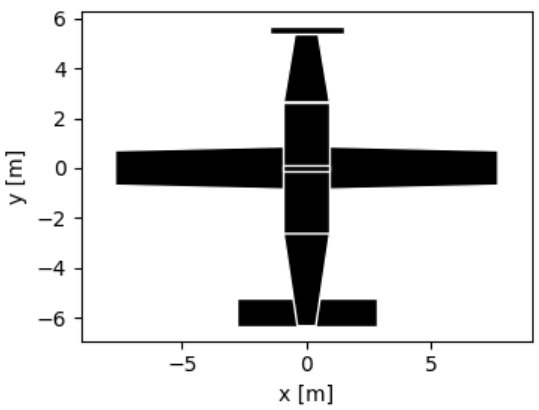


Figure 5.6: Cessna 208 planform diagram

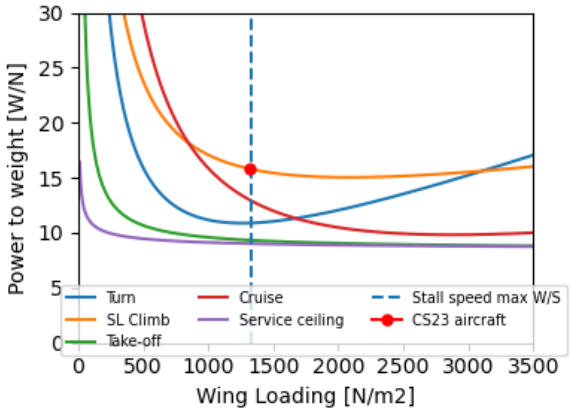


Figure 5.7: Cessna 208 constraint diagram

original 208. The harmonic range point is consistent, however at longer ranges the lines diverge slightly. The ferry range prediction is higher than the empirical data suggests.

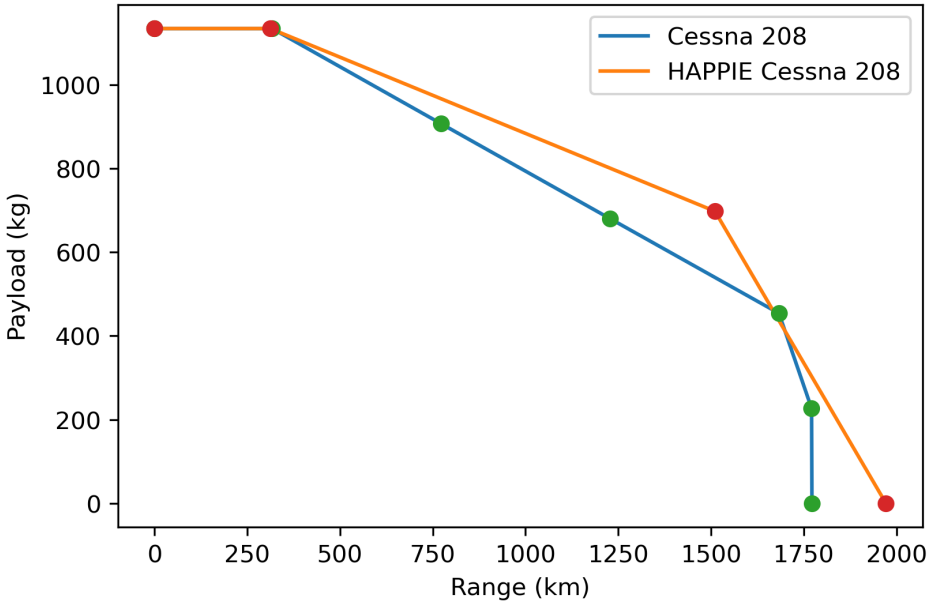


Figure 5.8: Cessna 208 Payload Range diagram comparison

## 5.3. Dornier Do 228

The Dornier Do 228 is a commuter airliner, which also performs cargo duties. It represents the upper limit of the CS-23 category. It is powered by twin turboprops running on kerosene. It is a STOL aircraft (Short Take Off & Landing) with the ability to transport up to 19 passengers. The newest version is considered, the Do 228 NG. Figure 5.9 shows an example of the configuration that is considered for this analysis.

### 5.3.1. Dornier Do 228 Inputs

The relevant inputs are shown in Table 5.7. The inputs have been obtained from official Do 228 documentation [42] [43].

Table 5.8 shows the aerodynamic coefficients predicted using the SUAVE mission analysis step of the methodology.

Figure 5.9: Dornier Do 228 NG [42]

Table 5.7: Dornier Do 228 input parameters

| Parameter | Value |
|---|---|
| Range $R$ $[km]$ | 396.0 |
| Cruise speed $V_{cruise}$ $[m/s]$ | 114.7 |
| Rate of climb $V_v$ $[m/s]$ | 8.0 |
| Cruise altitude $h_{cruise}$ $[m]$ | 3000 |
| Payload mass $m_{payload}$ $[kg]$ | 1960 |
| Tank oversizing factor $C_{oversize}$ $[-]$ | 5.0 |
| Maximum lift coefficient $C_{L_{max}}$ $[-]$ | 2.2 |

Table 5.8: Dornier Do 228 aerodynamic parameters

| Parameter | Value |
|---|---|
| $C_{D_{min}}$ | 0.0288 |
| $L/D$ | 10.98 |
| $k$ | 0.0592 |

### 5.3.2. Dornier Do 228 sizing results

Table 5.9 shows the sizing comparison for the key sizing parameters [42]. The $MTOM$ and $OEM$ are predicted within 10%. The maximum fuel load is not strongly predicted. The wing loading and power to weight ratio are both quite accurate, but slightly underestimated.

Table 5.9: Dornier Do 228 sizing comparison

| Parameter | Reference | HAPPIE sizing | Difference [%] |
|---|---|---|---|
| $MTOM$ $[kg]$ | 6400.0 | 5866.4 | -8.34 |
| $OEM$ $[kg]$ | 3900.0 | 3629.5 | -6.94 |
| Max $m_{fuel}$ $[kg]$ | 1885 | 1384.7 | -26.54 |
| $W/S$ $[N/m^2]$ | 1962 | 1953.1 | -0.45 |
| $P/W$ $[W/N]$ | 18.44 | 18.3 | -0.76 |

Figure 5.10 shows the generated planform diagram of the aircraft, with the main geometrical features. The tube and wing shape is much more applicable to this aircraft, even though the Do 228 features a ”square” fuselage cross section, as opposed to the round cross section assumed by the methodology.

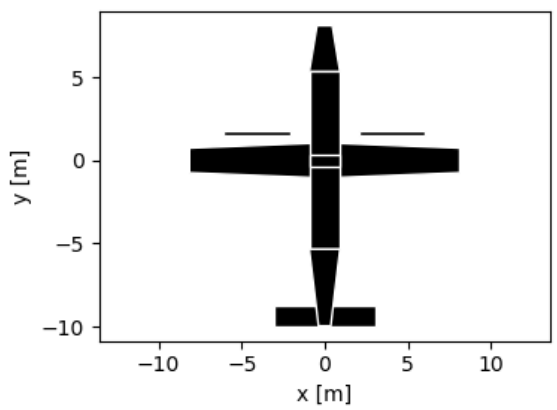


Figure 5.10: Dornier Do 228 planform diagram

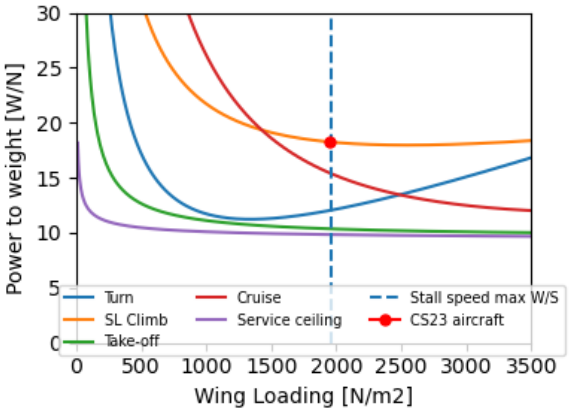


Figure 5.11: Dornier Do 228 constraint diagram

Figure 5.11 shows the generated constraint diagram of the aircraft, with the red point representing the chosen $P/W$ and $W/S$. Both the power to weight ratio and wing loading are higher than the previously discussed aircraft. This is due to the higher performance required of the aircraft, such as the climb rate. The chosen point on the constraint diagram is determined by the stall speed and climb requirements.

Finally, Figure 5.12 shows the payload range comparison between the generated aircraft and the original Do 228. The general shape is similar, however the slopes are slightly divergent at longer ranges and lower payloads.

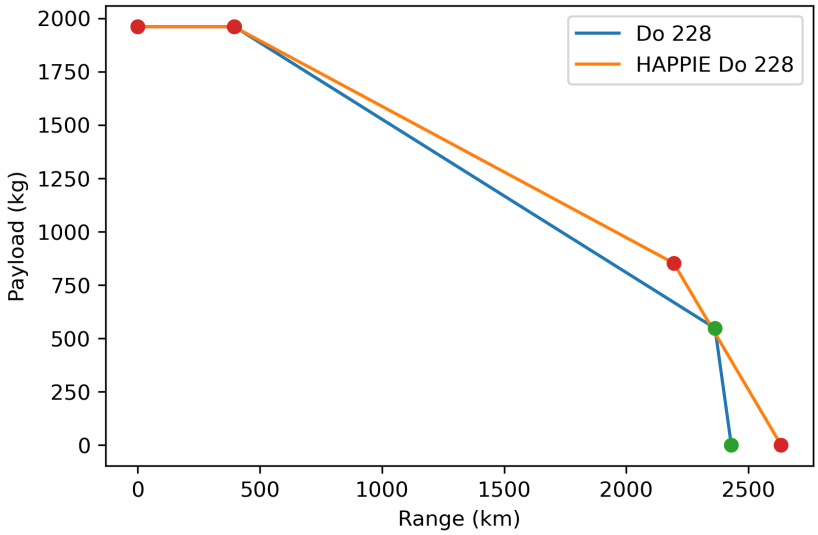


Figure 5.12: Dornier Do 228 Payload-Range comparison

## 5.4. Overview of the validation

The results for each of the aircraft are summarized in this section. An overview of the sizing results is shown in Table 5.10.

The methodology tends to underestimate the mass of the aircraft and associated fuel mass. The sizing results for the $MTOM$ and $OEM$ are accurate to within around 10% of the empirical data. This is sufficiently accurate for the conceptual design phase for which this methodology has been developed.

There are a couple of points that must be discussed in relation the results of the validation.

Table 5.10: Validation overview

| Parameter variation | Cessna 172 | Cessna 208 | Do 228 |
|---|---|---|---|
| $MTOM$ [%] | 7.80 | -9.90 | -8.34 |
| $OEM$ [%] | 8.62 | -5.56 | -6.94 |
| Max $m_{fuel}$ [%] | 3.61 | -44.40 | -26.54 |
| $W/S$ [%] | 5.77 | -3.90 | -0.45 |
| $P/W$ [%] | 0.85 | 12.06 | -0.76 |

### 5.4.1. Divergent payload range diagrams

The payload range diagrams for each of the aircraft do not exactly match the empirical data available [40] [41] [42]. For all three aircraft the slope between the second and third points on the diagram is less steep. This indicates that the powertrain, propulsive or air-frame efficiency of the actual aircraft is lower than is assumed in this validation.

### 5.4.2. Prediction of the drag coefficient/Lift to drag ratio

A possible explanation for the differing payload range diagrams is the estimation of the $L/D$ and $C_{D_{min}}$ parameters. In this methodology they are predicted using the SUAVE mission analysis, which operates on the principles as described earlier in Section 3.5. If the geometry is different from the actual aircraft geometry, differences will arise. For example, the landing gear of the aircraft are not taken into account in the SUAVE mission analysis. The assumption of a round fuselage also results in simplifications. This lower fidelity explains some of the divergent results.

### 5.4.3. Prediction of the maximum fuel load

The maximum fuel load is not predicted strongly for the validation aircraft. The maximum fuel load is determined by the fuel required for the ferry range, and the fuel tank oversizing factor. The oversizing factor is a user tunable parameter, which is used to match the payload range diagrams to the empirical data. It is important that the maximum fuel load assumed does not greatly exceed the actual maximum fuel load of the investigated aircraft. This is not the case in any of the investigated aircraft. The prediction of the maximum fuel load also relies on the fuel prediction of the harmonic mission, which depends on the efficiency of several aspects of the powertrain, as discussed in the previous sections.

# 6

# Results

In this chapter, the methodology presented in Chapter 3 and implemented in Chapter 4 is used to generate meaningful results. The methodology is followed to size several hydrogen fuel cell aircraft, to see the impact of different component technology levels on system level performance.

The results are broadly divided into the following sections:

- Sized hydrogen fuel cell aircraft
- Hydrogen fuel cell Technology comparison
- Powertrain component specifications
- Component and Mission sensitivity analyses

## 6.1. Sized hydrogen fuel cell aircraft

The main result of applying the methodology is the sizing of hydrogen fuel cell powered aircraft. As the methodology is general, it can be applied to any set of aircraft design parameters. To explore the possibilities of the hydrogen fuel cell powertrain, different aircraft in the CS-23 category were sized.

These aircraft are based on the aircraft used for validation in Chapter 5. These are the HFC versions of the Cessna 208 and Dornier Do 228. Two versions of each aircraft will be sized: one for current technology levels and one for expected future technology levels as defined in Chapter 2. In total 4 aircraft shall thus be explored.

Once these aircraft have been sized, they can be used as a baseline for sensitivity analyses in the rest of the results.

### 6.1.1. HFC Cessna 208

This hydrogen fuel cell aircraft is based on the Cessna 208 Caravan. To demonstrate the effects of changing to a hydrogen fuel cell powertrain, the sizing results will be compared with the conventionally sized aircraft. There are two versions of the hydrogen fuel cell aircraft which have been sized. HFC 208 is sized using current estimated technology levels, while HFC 208 fut makes use of estimated future technology levels. HFC 208 will be used as the baseline aircraft for the sensitivity analyses in the rest of the results.

Table 6.1 shows the comparative values for each of the configurations. The most important system level results are shown. Both the $MTOM$ and $OEM$ increase significantly. The empty mass fraction also increases, due to the much lower fuel mass. Due to the high specific energy of hydrogen, combined with the higher efficiency of the fuel cell electric powertrain, a smaller amount of fuel is required for the mission.

To examine the differences in mass for each concept, a mass breakdown is shown in Figure 6.1. The main difference in mass is caused by the heavy tank and powertrain. To highlight these in more detail, Figure 6.2 shows the powertrain mass breakdown for the hydrogen fuel cell powertrains. It can be seen that the fuel cell makes up the bulk of the powertrain mass.

Table 6.1: HFC 208 Sizing Comparison

| Parameter | C 208 | HFC 208 | [%] | HFC 208 fut | [%] |
|---|---|---|---|---|---|
| $MTOM\ [kg]$ | 3284.3 | 4907.2 | 49.41 | 3628.9 | 10.49 |
| $OEM\ [kg]$ | 2025.7 | 3736.3 | 84.44 | 2467.6 | 21.81 |
| Max $m_{fuel}\ [kg]$ | 561 | 166.1 | -70.39 | 123.1 | -78.06 |
| $W/S\ [N/m^2]$ | 1323.7 | 1323.7 | 0.00 | 1323.7 | 0.00 |
| $P/W\ [W/N]$ | 15.8 | 15.2 | -3.80 | 16.1 | 1.90 |

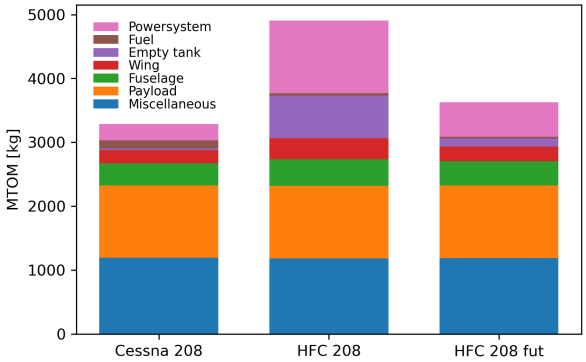


Figure 6.1: HFC 208 mass breakdown comparison

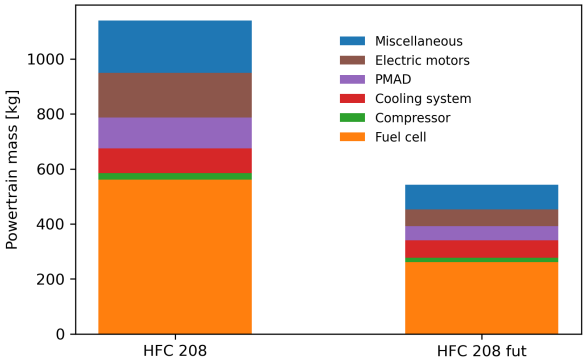


Figure 6.2: HFC 208 powertrain mass breakdown comparison

The power breakdown for the C208 HFC concepts is shown in Figure 6.3. The power breakdown shows that the future concept requires less power, however the fractions required to drive the cooling fan and compressor are the same. This is because they are dictated by cruise altitude and operating temperatures, a parameter that doesn't change between the concepts.

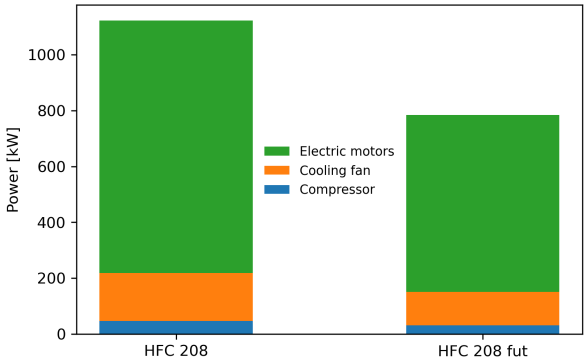


Figure 6.3: HFC 208 power breakdown comparison

Figure 6.4 shows the planform geometry comparison between the original aircraft and both HFC concepts. The main difference visually is the larger tank due to the low density of hydrogen, as well as the larger wing, due to the same wing loading and a higher weight. The difference between HFC 208 fut and the original aircraft is quite small, as the aircraft mass is similar, but the hydrogen tank is still significantly larger than the kerosene one.

Figure 6.5 shows the payload range diagram comparison. As can be seen, there is a large difference in behaviour. Since all aircraft are sized for the harmonic mission, they are the same up until that point. However, both HFC 208 and HFC 208 fut have a much less steep slope between the second and third points when compared to the conventional aircraft. This is due to the higher efficiency of the powertrain, as well as the greatly reduced fuel mass. The difference between both HFC concepts is the increased efficiency and lower fuel mass of the future aircraft.

The behaviour of the takeoff mass (TOM) in the payload range diagram is shown for each of the concepts in Figure 6.6. It can be seen that the takeoff mass for both hydrogen concepts is higher. In

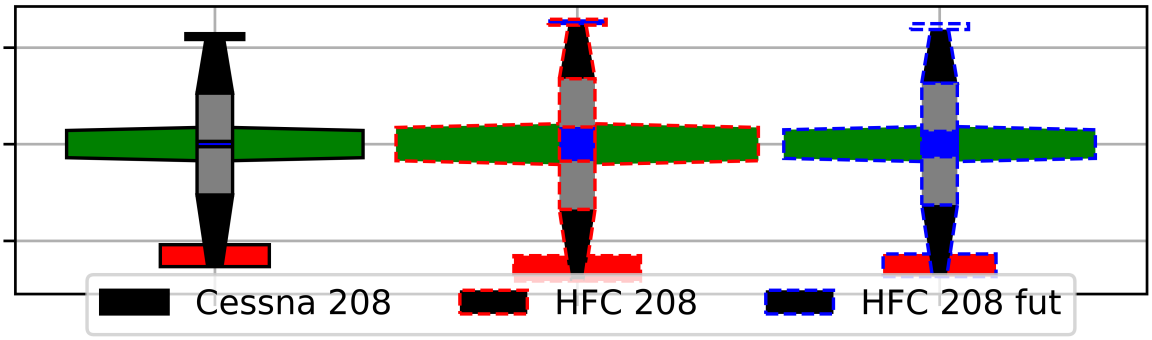


Figure 6.4: HFC 208 planform Comparison

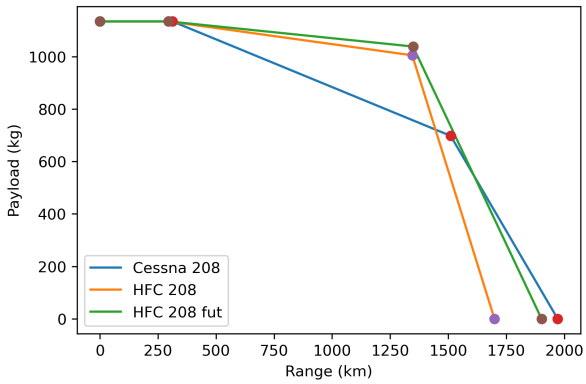


Figure 6.5: HFC 208 Payload Range comparison

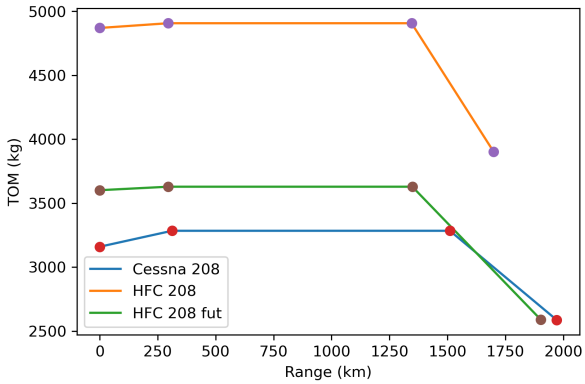


Figure 6.6: HFC 208 TOM Range comparison

addition, due to the low fuel mass, the TOM difference between points 1 and 2 is smaller for the HFC concepts, which represents the harmonic mission fuel mass.

Due to the detailed component sizing which is performed during the aircraft sizing routine, it is possible to determine high level component specifications for a given sized aircraft concept. In the case of the hydrogen electric powertrain, the most relevant components are shown in Table 6.2, with some example results for HFC 208. The parameters that are shown for each component are the specific power $\hat{\rho}$, the power $P$, mass $m$ and volume $V$.

Table 6.2: Example component specifications

| | $\hat{\rho}$ **[W/kg]** | $P$ **[kW]** | $m$ **[kg]** | $V$ **[m3]** |
|---|---|---|---|---|
| Fuel cell | 2000 | 1122.6 | 561.3 | - |
| PMAD | 10000 | 1122.6 | 112.3 | - |
| Electric motors | 5000 | 1010.4 | 162.8 | - |
| FC compressor | 2000 | 46.4 | 23.2 | - |
| Cooling system | 1900 | 171.8 | 90.4 | - |
| $H_2$ tank | - | - | 664.3 | 4.7 |

### 6.1.2. HFC Dornier Do 228

In this section the hydrogen fuel cell versions of the Dornier Do 228 are presented. All the aircraft are sized using the Dornier Do 228 input values as shown in Table 5.7. The most relevant sizing results are shown in Table 6.3. Both the $MTOM$ and $OEM$ increase, especially for the HFC 228 concept. The $MTOM$ of this concept even exceeds the CS-23 maximum allowable mass, and thus would not be able to be certified in this aircraft category.

To examine the differences in mass for each concept, the mass breakdown is shown in Figure 6.7.

Table 6.3: HFC 228 Sizing Comparison

| Parameter | Do 228 | HFC 228 | [%] | HFC 228 fut | [%] |
|---|---|---|---|---|---|
| $MTOM\ [kg]$ | 5866.4 | 10113.1 | 72.39 | 6630.8 | 13.03 |
| $OEM\ [kg]$ | 3629.5 | 8061.2 | 122.10 | 4609.7 | 27.01 |
| Max $m_{fuel}\ [kg]$ | 1384.7 | 459.3 | -66.83 | 305.5 | -77.94 |
| $W/S\ [N/m^2]$ | 1953.1 | 1953.1 | 0.00 | 1323.7 | -32.23 |
| $P/W\ [W/N]$ | 18.3 | 17.6 | -3.83 | 18.3 | 0.00 |

The main difference in mass is caused by the heavy tank and powertrain. The snowball effect is clearly visible in the HFC 228 concept. The miscellaneous and payload masses are the same for all concepts. The main differences are in the mass of the powertrain and tank, which are higher for the hydrogen fuel cell concepts. To highlight these in more detail, Figure 6.8 shows the powertrain mass breakdown for the hydrogen fuel cell powertrains.

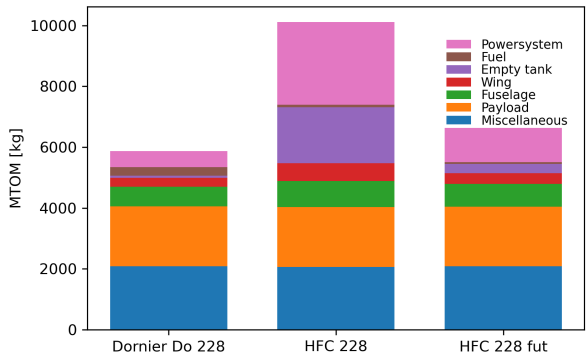


Figure 6.7: HFC 228 mass breakdown comparison

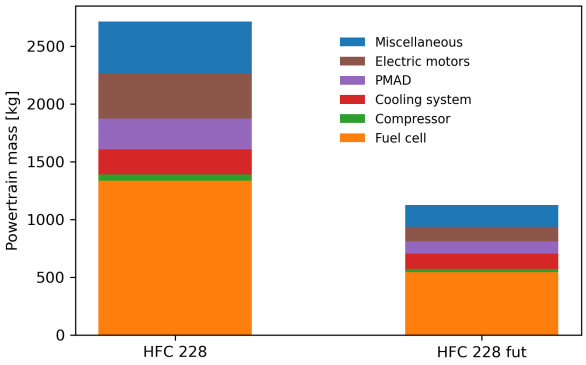


Figure 6.8: HFC 228 powertrain mass breakdown comparison

The power breakdown for the Do 228 HFC concepts is shown in Figure 6.9. The HFC 228 fut concept requires nearly half as much total power as the HFC 228 concept. The power fractions required to drive the electric motors, the cooling fan and compressor are similar. The compressor power is only a small fraction, while the cooling fan is responsible for significant parasitic power. The largest part of the power produced is used to drive the propellers through the electric motors and propel the aircraft.

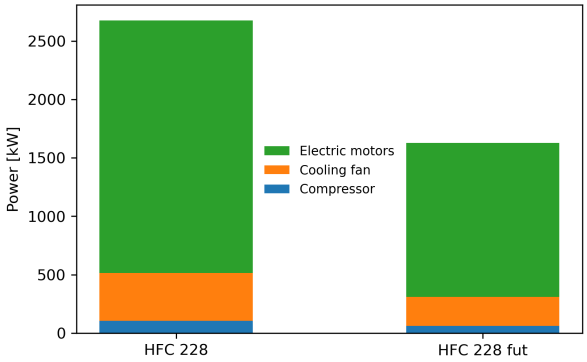


Figure 6.9: HFC 228 power breakdown comparison

Figure 6.10 shows the comparison between the original and HFC planforms. The extremely large hydrogen tank is clearly seen for the HFC 228 concept, while the reduced fuel mass and improved storage efficiency of the HFC 228 fut concept allows for a smaller tank.

The comparison of the capabilities for each of the aircraft concepts is shown in Figure 6.11. The TOM vs the range of the aircraft is also shown, highlighting the differences between the HFC concepts

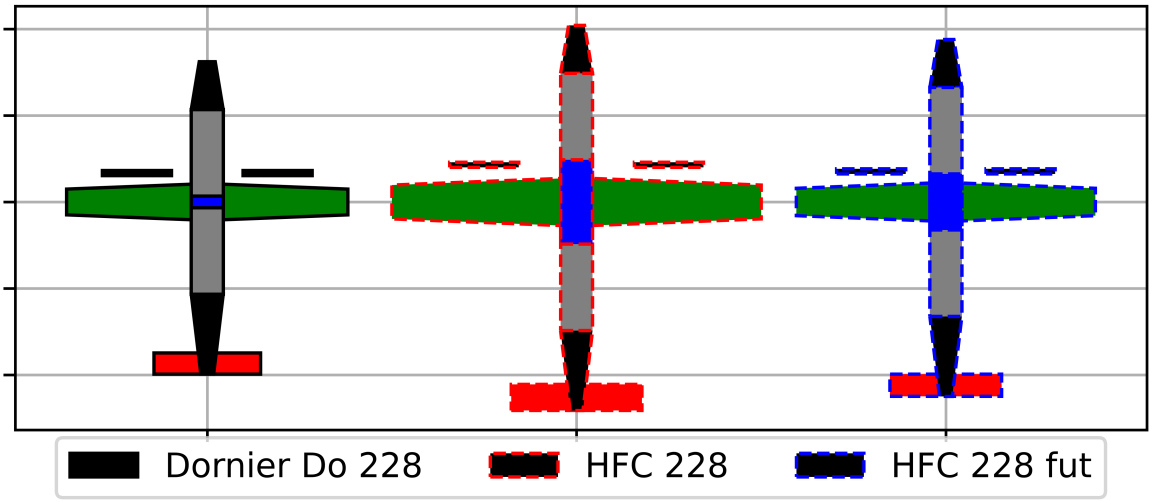


Figure 6.10: HFC 228 planform Comparison

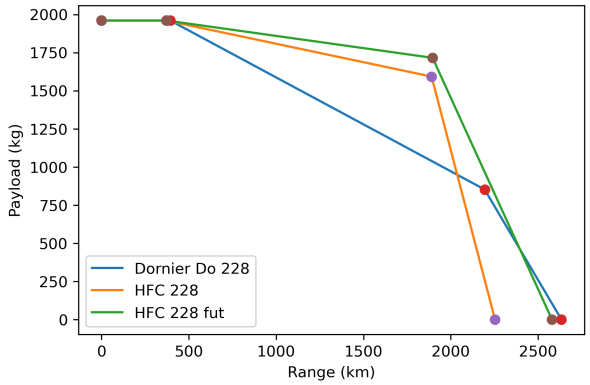


Figure 6.11: HFC 228 Payload Range comparison

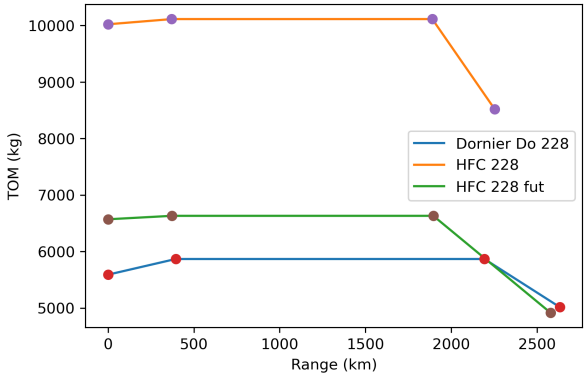


Figure 6.12: HFC 228 TOM Range comparison

and the conventionally powered aircraft. The characteristics are similar to the comparison presented earlier for the HFC 208 concepts.

### 6.1.3. Main differences between hydrogen fuel cell and conventional powertrains

As can be seen in the previous sections, even when sizing for the same harmonic mission, the sizing results are quite different between the original aircraft and the hydrogen fuel cell powered concepts. The main differences between both powertrains are highlighted in the list below:

1. The higher efficiency of the hydrogen fuel cell powertrain, combined with the high energy content of the hydrogen fuel leads to lower fuel mass.
2. The relatively low specific power of the hydrogen fuel cell powertrain components leads to heavy powertrains, which increases the total aircraft mass.
3. Low hydrogen tank storage efficiencies lead to heavy and bulky tanks, increasing the aircraft mass.
4. The empty mass fraction $OEM/MTOM$ is much higher for hydrogen fuel cell aircraft due to the lower fuel mass and increased powertrain mass.
5. The low density of hydrogen, combined with the volumetric storage efficiency of the tank contributes to large volume requirements, increasing the length of the fuselage when the tank is placed in the fuselage

## 6.2. Tank oversizing influence

As can be seen in the previous section, the hydrogen fuel cell concepts are heavier than the conventionally powered aircraft, mainly due to the large mass contribution of the hydrogen tank. This is due to the relatively low storage efficiency of the tank itself. The concepts presented in the previous section used the same fuel tank oversizing factor as the conventional aircraft. It is also possible to size the tank of the aircraft for exactly the harmonic mission, or some point in between. To explore this influence on the sizing of the aircraft, the baseline aircraft was sized for fuel cell oversizing factors from 1 to 4.5 to see their influence on the payload range diagram, as well as the $MTOM$ and $OEM$.

The results are shown in Figure 6.13. As can be seen, the payload range diagrams look completely different. The aircraft which fuel tank is sized for the harmonic mission only ($C_{oversize} = 1$) loses the capability of longer ferry range.

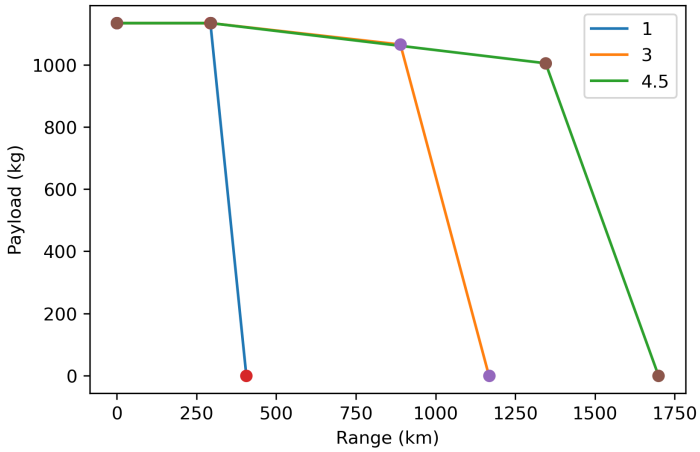


Figure 6.13: HFC payload range comparison

The effect of the oversizing factor on the $MTOM$ and $OEM$ is shown in Table 6.4.

Table 6.4: Fuel tank oversizing comparison

| Fuel tank oversizing | 1 | 3 | 4.5 |
|---|---|---|---|
| $MTOM$ $[kg]$ | 4102.5 | 4528.2 | 4907.2 |
| $OEM$ $[kg]$ | 2936.8 | 3359.7 | 3736.3 |
| Max $m_{fuel}$ $[kg]$ | 31.7 | 103.4 | 166.1 |
| $W/S$ $[N/m^2]$ | 1323.7 | 1323.7 | 1323.7 |
| $P/W$ $[W/N]$ | 15.4 | 15.3 | 15.2 |

As can be seen, the mass of the aircraft increases with increasing fuel tank oversizing. There is thus a trade off between the capabilities of the aircraft and the total mass and efficiency of that aircraft.

## 6.3. Comparison between technologies

For the comparison between different hydrogen fuel cell technologies, a baseline aircraft must be selected. Because the HFC 228 exceeded the certification requirements due to excessive mass, the HFC 208 is chosen as the baseline aircraft. The baseline aircraft will be used to compare the influence of different fuel cells, and hydrogen storage concepts. The different fuel cell types are listed in Table 6.5: LT-PEMFC is a low temperature Proton-Exchange Fuel Cell, HT-PEMFC is a High Temperature Proton-Exchange Fuel Cell, and SOFC is a Solid Oxide Fuel Cell. The defining parameter relevant for this sizing routine between these types of fuel cells is their operating temperature.

The different hydrogen storage options are shown in Table 6.6. The parameters of influence for the storage options are the storage efficiency $\eta_{storage}$, the hydrogen density $\rho_{H_2}$ and the volumetric efficiency $\eta_{vol}$.

Table 6.5: Fuel cell operating temperatures [21]

| Fuel cell type | Operating temperature [C] |
|---|---|
| LT-PEMFC | 80 |
| HT-PEMFC | 200 |
| SOFC | 600 |

Table 6.6: Hydrogen storage comparison

| Hydrogen storage type | $\eta_{storage}$ [%] | $\rho_{H_2}$ [kg/m3] | $\eta_{vol}$ [%] |
|---|---|---|---|
| 300 bar compressed hydrogen | 5 | 20 | 50 |
| 700 bar compressed hydrogen | 10 | 40 | 50 |
| Cryogenic liquid hydrogen | 20 | 70 | 50 |

These different hydrogen storage and conversion options are compared against each other using the baseline kerosene aircraft, to determine the effects of each. The harmonic range is increased, and the corresponding $MTOM$ is determined. The baseline aircraft is the HFC 208. Due to the large amount of points considered, only the HAPPIE part of the methodology was used to generate these results. The results are shown in Figure 6.14

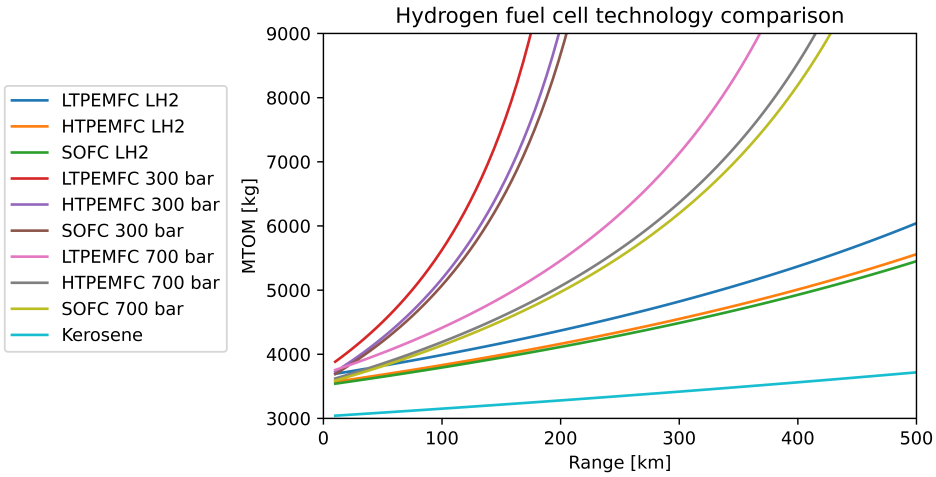


Figure 6.14: Hydrogen fuel cell technology comparison

It can be seen that kerosene results in a lighter aircraft when compared to any of the hydrogen fuel cell technologies, especially at longer ranges. This is due to the lower tank mass of the kerosene aircraft, as well as the lower powertrain mass.

There is also a consistent improvement with increasing operating temperature of the fuel cell from LT-PEMFC to SOFC, because of the smaller required cooling system. The largest effect is the difference in the hydrogen storage technologies. Liquid hydrogen storage mirrors the slope of the kerosene powered aircraft, while the compressed hydrogen storage methods both increase exponentially upwards. This indicates that compressed hydrogen storage methods are suitable for shorter ranges, but fall short at longer ranges. Liquid hydrogen storage is suitable for longer ranges, but at current technology levels cannot compete with kerosene powered aircraft.

## 6.4. Component sensitivity analysis

The HFC 208 as described in section 6.1 will be used to perform a sensitivity analysis on powertrain components. The baseline values for this sensitivity analysis are shown in Table 6.7.

The results of this component sensitivity analysis are shown in Figure 6.15. The chosen component parameters were varied in the range of +- 20%, to characterize their effects on the $MTOM$ of the aircraft.

To quantitatively state which component specification has the largest effect on the $MTOM$, the slopes

Table 6.7: Component sensitivity analysis setup

| Parameter | Baseline value |
|---|---|
| FC specific power $\hat{\rho}_{FC}$ $[W/kg]$ | 2000 |
| FC efficiency $\eta_{FC}$ [-] | 0.5 |
| Hydrogen storage efficiency $\eta_{storage}$ [-] | 0.2 |
| Hydrogen volumetric storage efficiency $\eta_{vol}$ [-] | 0.5 |
| FC operating temperature $T_{oper}$ $[C]$ | 80 |

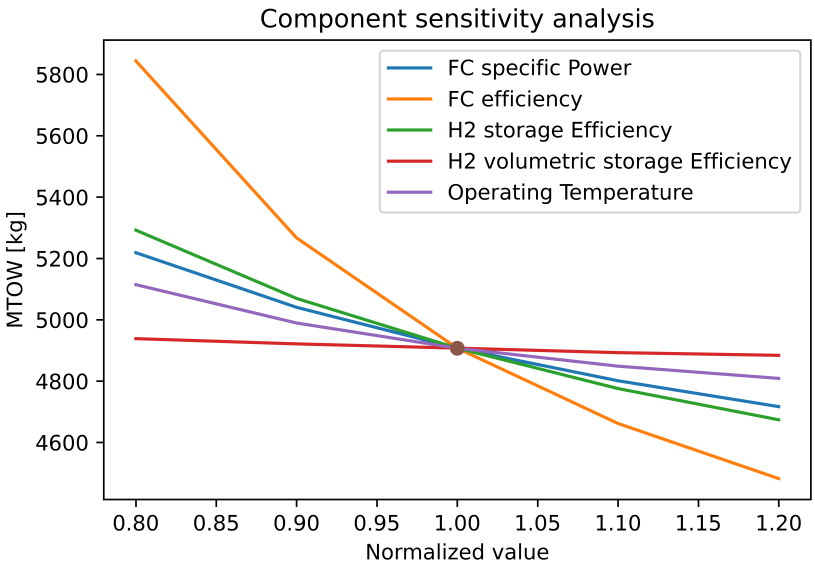


Figure 6.15: HFC 208 component sensitivity analysis

of the curves as they pass through the normalized point are determined and shown in Table 6.8.

Table 6.8: Component sensitivity qualitative analysis

| Parameter | Slope |
|---|---|
| FC specific power $\hat{\rho}_{FC}$ | -1062.2 |
| FC efficiency $\eta_{FC}$ | -2455.2 |
| H2 storage $\eta_{storage}$ | -1316.0 |
| H2 volumetric $\eta_{vol}$ | -147.3 |
| FC operating temperature $T_{oper}$ | -586.3 |

Each of the component performance parameters has a different effect on the $MTOM$ of the aircraft. The FC efficiency has the largest effect, followed by the hydrogen storage efficiency and the FC specific power. The operating temperature has an increasingly large penalty as the difference between the FC operating temperature and the ambient temperature becomes low, as the resulting heat exchanger must be larger to compensate for this. The volumetric storage efficiency has a comparatively small effect on the $MTOM$. This is due to the low fuel mass fraction of the aircraft, as well as the fact that the aircraft length does not increase significantly for the range of the sensitivity analysis considered here.

## 6.5. Mission parameter sensitivity analysis

Apart from the component level performance, it is also possible to vary the mission requirements of the aircraft. For this analysis, the cruise altitude was varied.

**Cruise altitude**

To investigate the influence of cruise altitude on the resulting aircraft design, the design cruise altitude was varied from 1000 meters to 5000 meters. The influence of this variation on the $MTOM$ is shown in Figure 6.16.

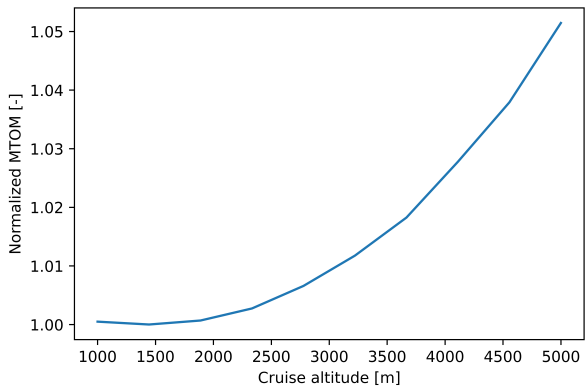


Figure 6.16: HFC 208 Normalized MTOM vs altitude

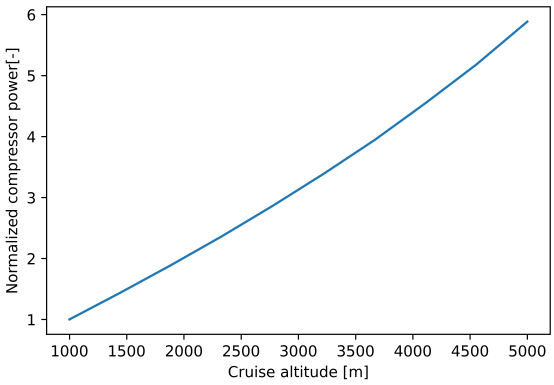


Figure 6.17: HFC 208 Normalized Compressor power vs altitude

In Figure 6.17 it can be seen that flying at higher altitudes necessitates a larger compressor to supply the fuel cell with air. To drive this compressor, a larger fuel cell is also required, as seen in Figure 6.18.

In Figure 6.19 the fuel necessary to fly the harmonic mission is shown as a function of the cruise altitude.

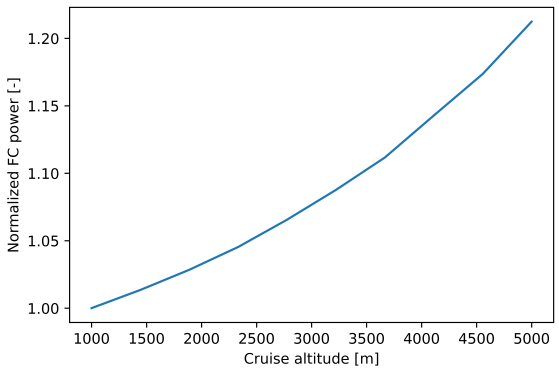


Figure 6.18: HFC 208 Normalized FC power vs altitude

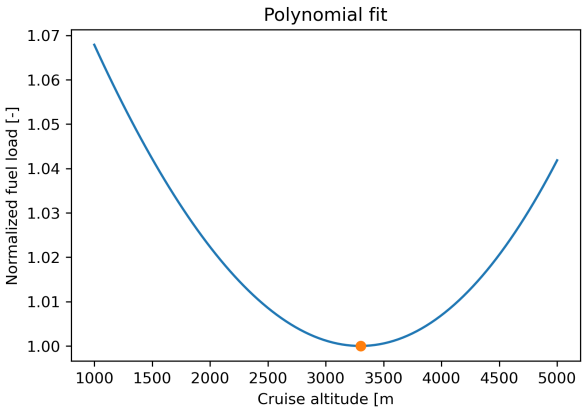


Figure 6.19: HFC 208 normalized fuel vs altitude

From Figure 6.19, it can be seen that the sizing methodology predicts an ideal lowest fuel mass at a moderate altitude of around 3000 meters. This is similar to the cruise altitude for piston powered aircraft.

## 6.6. Cooling thrust influence on constraint diagram

At the end of Chapter 3, the concept of the cooling system producing thrust was introduced. In this section, the influence of this additional cooling thrust on the constraint diagram is explored.

Figure 6.20 shows the influence of the calculated cooling thrust on the constraint diagram of the cruise condition. As can be seen, the $T/W$ requirements for the aircraft remain the same, however the $T/W$ that needs to be produced by the main propulsion system has reduced due to the $T/W$ contribution of the cooling system.

In Figure 6.21, this influence on the resulting $P/W$ ratio required is shown. It can be seen that the cooling thrust influence reduces the required $P/W$ ratio for the powertrain.

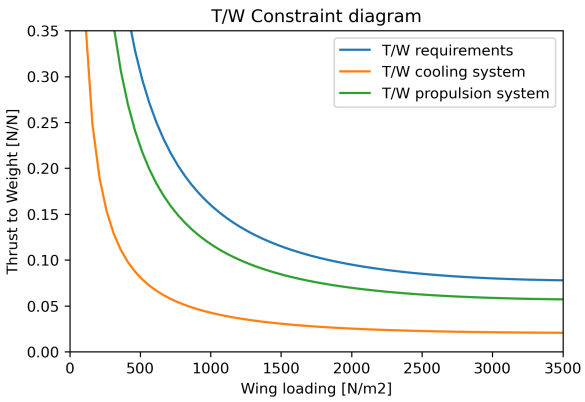


Figure 6.20: Cooling thrust T/W influence

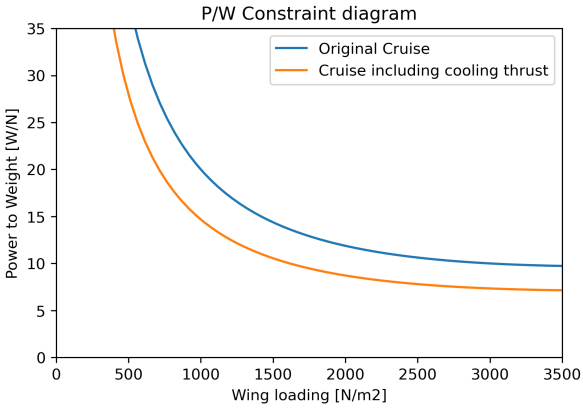


Figure 6.21: Cooling thrust P/W influence

The result of this procedure on the entire constraint diagram is shown in Figure 6.22.

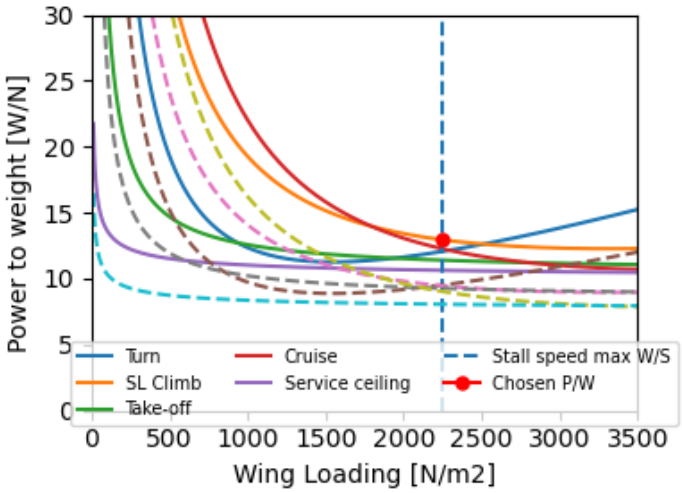


Figure 6.22: Constraint Diagram with Cooling thrust contribution

The solid lines represent the original $P/W$ vs $W/S$, while the dotted lines represent the revised $P/W$ requirements of the aircraft. It is noted that for all flight segments the power to weight requirements are reduced. The results suggest a reduction in $P/W$ and thus power requirements of around 30%, as this corresponds to the thrust contribution by the cooling system. To include this in the full design loop, it is necessary for the thrust results to be validated by performing a full heat exchanger cycle analysis, as is performed in the NASA paper from which these correlations originate [32].

# 7

# Discussion

There are several topics that need to be discussed in relation to the results and the methodology in general.

## 7.1. Model limitations

The main limitation of the methodology is caused by the models used. To be able to model the entire aircraft for the sizing methodology, several simplifications had to be made. These include an empirical fuel cell model, fixed component efficiencies and other simplifying assumptions. The influence of these simplified models can be seen in the different results generated by the methodology and SUAVE. When the sized aircraft is run and converges in SUAVE, the power required for each segment of flight is different than predicted by HAPPIE. This is due to the fact that SUAVE determines power requirements for each flight segment, which influences the efficiencies of the fuel cell for example. The methods used in SUAVE are therefore more elaborate, but are in agreement with the initial specification in HAPPIE.

The effect of operating temperature in this methodology is limited, possibly due to the use of over-simplified models for the cooling system. Operating temperature has small effect on performance, smaller than is expected. Due to the low operating temperature of fuel cells when compared to combustion powered engines, it was expected that the cooling system would cause a significant mass and aerodynamic penalty on the aircraft. However, using the NASA paper correlations [32], mass and aerodynamic penalty were not very significant compared to the other powertrain performance parameters. This is unexpected, and should be validated using a more detailed cooling system mode.

The aerodynamic model that has been used, based primarily on the vortex lattice method, is suitable for the conceptual design phases. However, it is not suitable to perform more detailed aerodynamic analysis. The influence of different parts of the aircraft geometry such as fuselage and nacelles is not taken into account. For example, when considering a more detailed distributed propulsion concept, it will be necessary to have a more rigorous aerodynamic estimation method, as the backwash of the propellers change the behaviour of the wing aerodynamics.

## 7.2. Inputs

The inputs to the analysis largely determine the relevance and accuracy of the outputs of this methodology. For the aircraft considered, all of the relevant data was gathered from publicly available sources. However, some assumptions such as the $C_{L_{max}}$ still must be made, since data on this is not available. This extends even stronger to the inputs for the hydrogen fuel cell powered aircraft, since empirical data on these powertrains is even more scarce. For example, the parameter value of the fuel cell specific power or the hydrogen storage efficiency have a large impact on the sizing results of the aircraft. Thus, the results that are shown represent the input variables chosen. If more refined inputs are available for these assumptions and powertrain technology levels, the methodology would be able to describe these and lead to more refined results.

## 7.3. Description of aircraft

The geometrical specification of the aircraft at this conceptual design phase is basic, which in turn places limitations on the accuracy of the aerodynamic analysis performed in SUAVE. The aircraft is modeled as a tube & wing aircraft, with a circular fuselage. Especially for smaller aircraft (such as the Cessna 172), the fuselage shape is quite different. This difference carries over into the aerodynamic and mass analysis performed in the methodology. For higher fidelity results, the geometrical description of the aircraft must also be refined. This can be done by determining the aircraft fuselage and wing geometries in more detail, as well as taking into account landing gear and other aircraft structures.

## 7.4. Net zero drag for the cooling system

One of the main research topics for hydrogen fuel cell powered aircraft is the behaviour of the cooling system. Adding a heat exchanger to reject heat to the ambient air adds mass and drag. However, in this methodology the cooling system is assumed to produce a net zero drag, due to the action of the cooling fan which ensures airflow through the radiator. This is based on the NASA paper described in Section 3.4.1 [32]. The assumption of zero drag for the cooling system must be verified, as well as the cooling thrust contribution.

## 7.5. Range of sensitivity analysis

For the component sensitivity analysis, the range of variation does not have the same effect on each parameter considered. For example, a 20% increase in fuel cell efficiency is a very large increase, approaching the maximum theoretical efficiencies. Meanwhile, a 20% increase in operating temperature is realistic and already surpassed by switching to a higher operating temperature fuel cell. Thus, not all the parameters, as discussed in the sensitivity analysis, are similarly sensitive to the range of sensitivity analysis values. This means that for identifying the most suitable research direction as a result of the sensitivity analysis, one must not simply look at the most sensitive parameter, but also at the parameter that can be improved upon the most.

## 7.6. Feasibility of the presented aircraft

For the current sizing methodology, there is no explicit point at which an aircraft design is considered unfeasible. This is due to the simplified definitions use to describe the aircraft. For example, it is possible for the hydrogen tank to make up the bulk of the aircraft total mass without running into problems in this methodology. However, when considering such a configuration for a practical aircraft, the resulting aircraft would not be realistic due to bracing and structure limitations. An example of such a configuration might be the HFC 228, which fuel tank makes up a significant portion of the mass breakdown and planform geometry.

In addition, the current methodology does not include detailed practical considerations in relation to passenger and payload placement. The hydrogen tank is assumed to be in the middle of the fuselage to satisfy the mass and balance of the aircraft. For a practical aircraft, the splitting of the passenger cabin is not preferable and might not be adequate. For further design steps, the exact placement of the hydrogen tank in the aircraft should be considered in more detail.

The limitations of the methodology that have been presented here result in the fact that it is most suitable for the conceptual design phase, in which a certain degree of uncertainty and variation is to be expected and accepted. For further design iterations and the preliminary and detailed design phases, more detailed models and assumptions should be used.

# 8

# Conclusions

The developed methodology for the sizing and validation of hydrogen fuel cell powered aircraft can be used to size a conceptual aircraft, including wing areas, component specifications and performance requirements. The methodology permits the analysis of conventional kerosene powered aircraft as well, which allows for validation. The design methodology has been validated for the CS-23 category, and as such is applicable within these limits. However, the methods used can also be applied to larger aircraft to study their performance and viability.

## 8.1. Conceptual design methodology

A feasible hydrogen fuel cell design can be obtained by following the developed methodology. The methodology has been validated using conventional CS-23 category aircraft. The validated methodology has been implemented in the HAPPIE software tool, which allows for convenient access to the methodology and its results.

Following the methodology that has been developed, hydrogen fuel cell aircraft are found to be generally heavier than conventional aircraft for current technology levels, when designed for the same mission and performance requirements. The empty mass fraction of the hydrogen fuel cell aircraft is increased, due to the low fuel mass and high powertrain and tank mass.

## 8.2. Performance of hydrogen fuel cell powered aircraft

Regarding the performance of hydrogen fuel cell powered aircraft, several aspects are highlighted.

### 8.2.1. Payload range diagram

The payload range diagrams for hydrogen fuel cell aircraft are markedly different from kerosene powered aircraft. The shape and thus operational capabilities of the specific aircraft are dependant on the hydrogen tank design choices made. The different shape is caused by the lower fuel mass of hydrogen, which only displaces a small amount of payload. Furthermore, the higher powertrain efficiency of the fuel cell powertrain reduces the slope of the lines. This allows the hydrogen fuel cell aircraft to be superior for certain long range and high payload missions. The hydrogen tank may also be sized for the harmonic range, which reduces the weight penalty of a heavy tank. However, this design choice leads to a greatly diminished ferry range.

### 8.2.2. Hydrogen fuel cell technology comparison

A comparison was made on the influence of different hydrogen fuel cell technologies. These included the most relevant types of fuel cells and hydrogen storage methods. The technologies were compared by their influence on the $MTOM$ at increasing harmonic mission ranges.

It was found that the operating temperature of the fuel cell had a relatively minor effect on the $MTOM$ of the aircraft, and no strong correlation at increased ranges. The effect of operating temperature in this methodology is limited, possibly due to the use of oversimplified models for the cooling system.

Meanwhile, the hydrogen storage methods were found to have a large influence on the aircraft mass, especially at longer ranges. The defining parameter influencing this behaviour was the storage efficiency of the hydrogen storage option, and not the volume taken up by the tank.

Cryogenic liquid hydrogen was found to be the most suitable hydrogen storage method, however compressed hydrogen storage concepts are also viable, even though they are heavier due to the heavier and bulkier compressed hydrogen tanks.

### 8.2.3. Sensitivity analysis

In the thesis, to explore the influence of different parameters on the performance and design of the hydrogen fuel cell aircraft, sensitivity analyses were performed on mission and component performance parameters.

**Component performance**

The component level performance parameters that were explored were the fuel cell specific power, fuel cell efficiency, fuel cell operating temperature, hydrogen storage efficiency and hydrogen volumetric efficiency.

The fuel cell was found to be the most essential component, with the fuel cell efficiency having the largest effect on aircraft mass. Fuel cell specific power and hydrogen storage efficiency are both essential aspects to improve upon, and may be more relevant for the research direction, as there is more room for improvement.

**Mission parameters**

The best cruise altitude was found to be at an intermediate altitude, around 3 km. This is comparable to piston powered aircraft. Gas turbine powered aircraft are generally more efficient at higher altitudes. The trade-off is between increased aerodynamic efficiency at higher altitudes, and the increased power required for the climb segment, as well as the increased power demand for the fuel cell compressor supplying the fuel cell with ambient pressure air.

### 8.2.4. Cooling thrust

The considered cooling system model predicts a cooling thrust, which can be used to assist in aircraft propulsion. The influence of thrust produced by the cooling system has the effect of lowering the wing loading and power to weight ratio required for a given performance specification. The cooling thrust contribution must be verified using more detailed component models for the cooling system. The methodology presented predicts that the cooling thrust can lead to reduced powertrain, fuel and tank masses, and thus lighter and higher performance aircraft.

# 9

# Recommendations

In this chapter directions for further research are presented. Four main recommendations have been identified.

## 9.1. More detailed component models

The accuracy of the system model is only as good as the component models that make up the entire system model. More detailed component models will increase the reliability and validity of the results. The most important subsystems that should be explored further are the cooling system, the fuel cell system, and the hydrogen tank.

The cooling model in the current methodology is based on optimized correlations obtained from thermal analysis papers by NASA. While these do provide an indication of relationships between the operating temperature, heat rejection power and the size/mass and drag of the cooling system, they are in a sense ”oversimplified”, not taking into account important effects such as airspeed, density, etc. Thus, a more detailed, physically based cooling model should be developed. This will also address the assumption of zero drag/thrust for the radiator design, or perhaps even the ability to size the radiator without any need for a puller fan.

The fuel cell model is similarly based on empirical fuel cell performance data, which is a simplified version, not taking into account the physical processes which happen inside the fuel cell itself. A physically based model would provide more realistic behaviour, as well as the possibility of exploring the influence of different operating temperatures and pressures on fuel cell stack performance, whereas in the current methodology, the fuel cell is always supplied with 1 bar atmospheric pressure air. This model would be especially useful for the SUAVE mission analysis, to more accurately represent the behaviour of the fuel cell in every flight condition during the mission.

The hydrogen storage model in this methodology is assumed to be static, and is not modeled past its influence on the aircraft mass and geometry. However, as explained earlier, liquid hydrogen is not able to be stored indefinitely due to boil off effects. By creating a hydrogen tank component, the behaviour of the liquid hydrogen can be characterized. This is particularly relevant for liquid hydrogen due to its very low storage temperature, and because liquid hydrogen is the best hydrogen storage option. The thermal effects of cryogenic fuel can furthermore offer a benefit by reducing the heat power that must be rejected through the cooling system, through the heating up of the hydrogen before it is led into the fuel cell.

## 9.2. Hybrid electric powertrain

Due to the electric nature of the powertrain, it is also possible to combine the fuel cell with a battery. The battery would be able to provide peak power, power smoothing and increased system redundancy.

The battery can be used to provide peak power for demanding flight conditions, such as takeoff and climb. This can allow for the fuel cell to be sized for the cruise condition only, which may save mass when compared to sizing the fuel cell to provide power in all situations.

Secondly, the dynamic response of current fuel cell stacks is quite poor. This delay in power delivery can be detrimental to the performance of the aircraft, especially for unexpected maneuvers. Therefore,

the use of a battery to provide power during these transients can allow for more flexibility and performance for dynamic maneuvers requiring different power inputs.

Another advantage is increased system redundancy, which can improve the safety of the entire aircraft. For example. if the fuel cell stops working, a battery on board could provide enough energy to power the flight systems, as well as flight propulsive power to allow for a controlled descent and landing.

## 9.3. Benefits of electric powertrain

Currently, the methodology uses the fuel cell to drive main propellers similar to conventional aircraft. However, the use of an electric powertrain can also allow for novel propulsion integrations with the air frame. Some examples include distributed electric propulsion and propulsive fuselages. These propulsion system integrations can provide an additional boost in performance and redundancy when compared to conventional aircraft.

For example, using distributed propulsion, the wing loading of the aircraft can be increased, as the distributed propulsion can provide adequate lift for the takeoff and landing segments of the flight. Additionally, the use of multiple independent propulsion units increases the redundancy of the concept, as the loss of one unit only leads to a small decrease in total available thrust.

The use of electric propulsion can also be integrated in the control system of the aircraft, providing differential thrust when required. This can lead to the reduction in control surface size, further leading to increased efficiency of the entire aircraft.

Only when taking into account these aspects, can the full benefit of the hydrogen fuel cell electric powertrain be determined and compared against conventional aircraft.

## 9.4. Optimization of components

The results obtained in this report have been obtained without performing a optimization for the powertrain. An optimization could be performed on several aspects of the powertrain. The most important ones are the fuel cell sizing, and the hydrogen tank insulation thickness.

When the fuel cell is used as the primary power source of the aircraft, the choice can be made for the fuel cell to be sized to provide a higher power than required during the flight. This is known as the fuel cell oversizing factor, which reflects how much more powerful the fuel cell is. The larger fuel cell will be heavier, but also more efficient at the lower power requirements. This can lead to a reduction in hydrogen fuel required. This trade off can lead to an ideal fuel cell size.

The optimal tank insulation thickness is another aspect which can benefit from an optimization routine. In the current methodology, the hydrogen storage efficiency is a user inputted variable, which is thus tied to the thickness and mass of the insulation. If instead, the hydrogen tank is defined according to the insulation thickness and performance, its behaviour can be modeled closer to a physical model. A thicker tank insulation will lead to less boil off/less hydrogen potentially lost, but more volume and mass taken up by the tank. Determining the ideal hydrogen tank insulation would be an interesting result for a given mission, and might lead to higher performance aircraft than those considered here.

By optimizing both these parameters, the aircraft may be lighter and consume less fuel, which leads to the better optimized and higher performing aircraft.

# References


[1] R. Berger, “Hydrogen | a future fuel for aviation?” Roland Berger GMBH, Tech. Rep., 2020.

[2] Airbus, “Airbus global market forecast 2019-2038,” Airbus, Tech. Rep., 2019.

[3] T. Stalnaker, G. Alport, A. Buchanan, and A. Taylor, “Airline economic analysis 2018-2010 edition,” Oliver Wyman, Tech. Rep., 2019.

[4] M. Dareki and et al., “Flightpath 2050,” European Commission, Tech. Rep., 2011.

[5] McKinsey and Company, “Hydrogen-powered aviation | a fact-based study of hydrogen technology, economics and climate impact by 2050,” McKinsey and Company, Tech. Rep., 2020.

[6] L. Wilcox, K. Shine, and B. Hoskins, “Radiative forcing due to aviation water vapour emissions,” *Atmospheric Environment*, vol. 63, pp. 1–13, 2012, ISSN: 1352-2310. DOI: https://doi.org/10.1016/j.atmosenv.2012.08.072. [Online]. Available: http://www.sciencedirect.com/science/article/pii/S135223101200859X.

[7] G. Romero, F. Borello, E. Cestino, and G. Correa, “All electric intercity-aircraft design based on fuel cell energy system,” Tech. Rep.

[8] T. Koehler, “Boeing frontiers: A green machine,” Tech. Rep. DOI: https://www.boeing.com/news/frontiers/archive/2008/may/ts_sf04.pdf.

[9] S. Nicolay, Y. Liu, and A. Elham, “Conceptual design and optimization of a general aviation aircraft with fuel cells and hydrogen,” Tech. Rep.

[10] ZeroAvia, *Zero avia*. DOI: https://www.zeroavia.com/.

[11] H2FLY. DOI: https://h2fly.de/.

[12] S. Gudmundsson, *General Aviation Aircraft Design*. Elsevier, 2014.

[13] D. Raymer, *Aircraft Design: A Conceptual Approach*. AIAA Education Series, 1996.

[14] EASA, “Certification specifications for normal-category aeroplances cs-23,” Tech. Rep.

[15] T. MacDonald, M. Clarke, E. M. Botero, J. M. Vegh, and J. J. Alonso, “Suave: An open-source environment enabling multi-fidelity vehicle optimization,” in *18th AIAA/ISSMO Multidisciplinary Analysis and Optimization Conference*. DOI: 10.2514/6.2017-4437. eprint: https://arc.aiaa.org/doi/pdf/10.2514/6.2017-4437. [Online]. Available: https://arc.aiaa.org/doi/abs/10.2514/6.2017-4437.

[16] A. Wendorff, A. Variyar, C. Ilario, E. Botero, F. Capristan, J. Smart, J. Alonso, L. Kulik, M. Clarke, M. Colonno, M. Kruger, J. M. Vegh, P. Goncalves, R. Erhard, R. Fenrich, T. Orra, T. St. Francis, T. MacDonald, T. Momose, T. Economon, T. Lukaczyk, and W. Maier, *Suave: An aerospace vehicle environment for designing future aircraft*, version 2.1, 2020. [Online]. Available: https://github.com/suavecode/SUAVE.

[17] F. Barbier, H. Barthelemy, and M. Weber, “Hydrogen storage: Recent improvements and industrial perspectives,” *International Journal of Hydrogen Energy*, no. 42, pp. 7254–7262, 2017.

[18] M. Gardiner, “Energy requirements for hydrogen gas compression and liquefaction as related to vehicle storage needs,” Tech. Rep., 2009.

[19] C. Winnefeld, T. Kadyk, B. Bensmann, U. Krewer, and R. Hanke-Rauschenbach, “Modelling and designing cryogenic hydrogen tanks for future aircraft applications,” *Energies*, vol. 11, p. 105, Jan. 2018. DOI: 10.3390/en11010105.

[20] E. Rivard, M. Trudeau, and K. Zaghib, “Hydrogen storage for mobility: A review,” *Materials*, vol. 12, p. 1973, Jun. 2019. DOI: 10.3390/ma12121973.

[21] A. L. Dicks and D. A. Rand, *Fuel Cell Systems Explained*. Wiley, 2018.

[22] O. Z. Sharaf and M. F. Orhan, “An overview of fuel cell technology: Fundamentals and applications,” *Renewable and Sustainable Energy Reviews*, vol. 32, pp. 810–853, 2014, ISSN: 1364-0321. DOI: https://doi.org/10.1016/j.rser.2014.01.012. [Online]. Available: http://www.sciencedirect.com/science/article/pii/S1364032114000227.

[23] J. Banke, *Technology readiness levels demystified*, Aug. 2010. [Online]. Available: https://www.nasa.gov/topics/aeronautics/features/trl%5C_demystified.html.

[24] R. Rosli, A. Sulong, W. Daud, M. Zulkifley, T. Husaini, M. Rosli, E. Majlan, and M. Haque, “A review of high-temperature proton exchange membrane fuel cell (ht-pemfc) system,” *International Journal of Hydrogen Energy*, vol. 42, no. 14, pp. 9293–9314, 2017, Special Issue on Sustainable Fuel Cell and Hydrogen Technologies: The 5th International Conference on Fuel Cell and Hydrogen Technology (ICFCHT 2015), 1-3 September 2015, Kuala Lumpur, Malaysia, ISSN: 0360-3199. DOI: https://doi.org/10.1016/j.ijhydene.2016.06.211. [Online]. Available: http://www.sciencedirect.com/science/article/pii/S0360319915313069.

[25] A. Beney, “Investigation into the heat up time for solid oxide fuel cells in automotive applications,” 2018.

[26] F. Barbir, *PEM Fuel Cells Theory and Practice*, Second. Amsterdam: Academic Press, 2013, pp. viii+529, Translated from the Polish by the author, ISBN: 978-0-12-387710-9.

[27] D. Hao, J. Shen, Y. Hou, Y. Zhou, and H. Wang, “An improved empirical fuel cell polarization curve model based on review analysis,” Tech. Rep., 2016.

[28] J. W. Pratt, J. Brouwer, and G. S. Samuelsen, “Performance of proton exchange membrane fuel cell at high-altitude conditions,” *Journal of Propulsion and Power*, vol. 23, no. 2, pp. 437–444, 2007. DOI: 10.2514/1.20535. [Online]. Available: https://doi.org/10.2514/1.20535.

[29] A. Fly and R. Thring, “A comparison of evaporative and liquid cooling methods for fuel cell vehicles,” *International Journal of Hydrogen Energy*, vol. 41, no. 32, pp. 14 217–14 229, 2016, ISSN: 0360-3199. DOI: https://doi.org/10.1016/j.ijhydene.2016.06.089. [Online]. Available: http://www.sciencedirect.com/science/article/pii/S0360319916318444.

[30] J. Barroso, J. Renau, A. Lozano, J. Miralles, J. Martín, F. Sánchez, and F. Barreras, “Experimental determination of the heat transfer coefficient for the optimal design of the cooling system of a pem fuel cell placed inside the fuselage of an uav,” *Applied Thermal Engineering*, vol. 89, pp. 1–10, 2015, ISSN: 1359-4311. DOI: https://doi.org/10.1016/j.applthermaleng.2015.06.003. [Online]. Available: http://www.sciencedirect.com/science/article/pii/S1359431115005529.

[31] J. Renau, J. Barroso, A. Lozano, A. Nueno, F. Sánchez, J. Martín, and F. Barreras, “Design and manufacture of a high-temperature pemfc and its cooling system to power a lightweight uav for a high altitude mission,” *International Journal of Hydrogen Energy*, vol. 41, no. 43, pp. 19 702–19 712, 2016, The 5th Iberian Symposium on Hydrogen, Fuel Cells and Advanced Batteries (HYCELTEC 2015), 5-8 July 2015, Tenerife, Spain, ISSN: 0360-3199. DOI: https://doi.org/10.1016/j.ijhydene.2015.12.209. [Online]. Available: http://www.sciencedirect.com/science/article/pii/S0360319915307552.

[32] J. W. Chapman, S. L. Schnulo, and M. P. Nitzsche, “Development of a thermal management system for electrified aircraft,” NASA Glenn Research Center, Tech. Rep., 2020.

[33] T. Kadyk, C. Winnefeld, R. Hanke-Rauschenbach, and U. Krewer, “Analysis and design of fuel cell systems for aviation,” *Energies*, vol. 11, no. 2, 2018, ISSN: 1996-1073. DOI: 10.3390/en11020375. [Online]. Available: https://www.mdpi.com/1996-1073/11/2/375.

[34] R. de Vries, M. Hoogreef, and R. Vos, “Preliminary sizing of a hybrid-electric passenger aircraft featuring over-the-wing distributed-propulsion,” Tech. Rep., 2016.

[35] R. de Vries, M. Brown, and R. Vos, “Preliminary sizing method for hybrid-electric distributed-propulsion aircraft,” *Journal of Aircraft*, vol. 56, no. 6, 2019. DOI: https://doi.org/10.2514/1.C035388.

[36] M. D. Gosálvez, J. van Ham, S. Joosten, D. Juschus, G. Nieuwerth, T. van Pelt, L. Smit, M. Takken, Y. Wang, and T. Ziere, “Green flying final report,” Tech. Rep., 2018.

[37] J. Katz and A. Plotkin, *Low-Speed Aerodynamics*, 2nd ed., ser. Cambridge Aerospace Series. Cambridge University Press, 2001. DOI: 10.1017/CBO9780511810329.

[38] J. J. Bertin and R. M. Cummings, *Aerodynamics for engineers*, 5th ed. Pearson Education International, 2009.

[39] M. Yahyaoui, "Generalized vortex lattice method for predicting characteristics of wings with flap and aileron deflection," *International Journal of Aerospace and Mechanical Engineering*, vol. 8, no. 10, pp. 1690–1698, 2014, ISSN: eISSN: 1307-6892. [Online]. Available: https://publications.waset.org/vol/94.

[40] J. McIver, "Cessna skyhawk ii / 100 performance assessment," Tech. Rep., 2003.

[41] T. Aviation, *Cessna caravan specifications*. DOI: https://cessna.txtav.com/en/turboprop/caravan#_model-specs.

[42] RUAG, "Dornier 228 advanced commuter (ac) facts and figures," RUAG Aerospace Services GmbH, Tech. Rep., 2017.

[43] EASA, "Easa type-certificate data sheet dornier 228 series," Tech. Rep., 2017.

]

# A

# Full inputs to the methodology

In this appendix, the full list of inputs used for the validation aircraft, as well as for the baseline hydrogen fuel cell aircraft are presented.

- Cessna 172, Section A.1
- Cessna 208, Section A.2
- Dornier Do 228, Section A.3
- Baseline HFC 208 aircraft, Section A.4

## A.1. Cessna 172 full inputs

The full list of inputs for the Cessna 172 is shown in Tables A.1 to A.4.

Table A.1: Cessna 172 Customer Requirements

| Parameter | Value |
|---|---|
| Harmonic range: $R$ $[km]$ | 752.0 |
| Sustained turning speed: $V_{turn}$ $[m/s]$ | 50.0 |
| Climb speed: $V_{climb}$ $[m/s]$ | 50.0 |
| Takeoff speed: $V_{TO}$ $[m/s]$ | 30.0 |
| Cruise speed: $V_{cruise}$ $[m/s]$ | 62.8 |
| Sea Level rate of climb: $V_v$ $[m/s]$ | 3.71 |
| Service ceiling rate of climb: $V_{v_{ceiling}}$ $[m/s]$ | 0.51 |
| Stall speed: $V_{stall}$ $[m/s]$ | 24.7 |
| Maximum dive speed: $V_{dive}$ $[m/s]$ | 83.9 |
| Takeoff ground roll distance: $S_G$ $[m]$ | 293.0 |
| Service ceiling: $h_{ceiling}$ $[m]$ | 4267.0 |
| Cruise altitude: $h_{cruise}$ $[m]$ | 3658.0 |
| Design airfield altitude: $h_{TO}$ $[m]$ | 0.0 |
| Load factor/Sustained G's in turn: $n$ [-] | 1.41 |
| Number of passengers: $N_{pass}$ [-] | 4 |
| Payload mass: $m_{payload}$ $[kg]$ | 0 |
| Energy source oversizing factor: $C_{oversize}$ [-] | 1.3 |

## A.2. Cessna 208 full inputs

The full list of inputs is shown in Tables A.5 to A.8.

## A.3. Dornier Do 228 full inputs

The full list of inputs is shown in Tables A.9 to A.12.

Table A.2: Cessna 172 Assumptions

| Parameter | Value |
|---|---|
| **Minimum drag coefficient:** $C_{D_{min}}$ [-] | 0.0396 |
| Takeoff drag coefficient: $C_{D_{TO}}$ [-] | 0.05 |
| Takeoff lift coefficient: $C_{L_{TO}}$ [-] | 0.7 |
| Maximum lift coefficient: $C_{L_{max}}$ [-] | 2.0 |
| **Lift induced drag constant:** $k$ [-] | 0.072 |
| Ground friction constant: $\mu$ [-] | 0.04 |
| **Lift to Drag ratio:** $L/D$ [-] | 10.59 |
| Passenger mass: $m_{pass}$ [kg] | 77.0 |
| Safety factor: $C_{safety}$ [-] | 1.5 |
| Reference empty mass fraction: $(OEM/MTOM)_{ref}$ [-] | 0.6 |

Table A.3: Cessna 172 Powertrain parameters

| Parameter | Value |
|---|---|
| Power generation specific power: $\hat{\rho}_{FC}$ $[W/kg]$ | 1000.0 |
| Power delivery specific power: $\hat{\rho}_{PMAD}$ $[W/kg]$ | 100000.0 |
| Power conversion specific power: $\hat{\rho}_{em}$ $[W/kg]$ | 100000.0 |
| Power generation efficiency: $\eta_{FC}$ [-] | 0.25 |
| Power delivery efficiency: $\eta_{PMAD}$ [-] | 0.95 |
| Power conversion efficiency: $\eta_{em}$ [-] | 0.95 |
| Energy source storage efficiency: $\eta_{storage}$ [-] | 0.95 |
| Energy source volumetric efficiency: $\eta_{volumetric}$ [-] | 0.95 |
| Energy source density: $\rho_{fuel}$ $[kg/m^3]$ | 800.0 |
| Specific energy: $LHV_{fuel}$ $[MJ/kg]$ | 43.0 |
| Propulsive efficiency: $\eta_{prop}$ [-] | 0.8 |
| Number of propellers: $N_{props}$ [-] | 1 |
| Propeller diameter: $D_{prop}$ $[m]$ | 3.0 |
| Powertrain operating temperature: $T_{oper}$ $[C]$ | 800.0 |
| Cooling thrust correction: $C_{coolthrust}$ [-] | 0.0 |
| Compressor specific power: $\hat{\rho}_{comp}$ $[W/kg]$ | 100000.0 |
| Compressor efficiency: $\eta_{comp}$ [-] | 1.0 |

Table A.4: Cessna 172 Aircraft Characteristics

| Parameter | Value |
|---|---|
| Wing aspect ratio: $AR_{wing}$ [-] | 7.32 |
| Sweep Quarter chord: $\Lambda_{C/4}$ [-] | 0.0 |
| Thickness to chord ratio: $t/c$ [-] | 0.2 |
| Taper Ratio: $\lambda$ [-] | 1.0 |
| Seats abreast: $N_{seat,abreast}$ [-] | 2 |
| Nose fineness ratio: $F_{nose}$ [-] | 1.0 |
| Tail fineness ratio: $F_{tail}$ [-] | 2.0 |
| Seat pitch: $l_{seat}$ [m] | 0.8 |
| Door length: $l_{door}$ [m] | 1.0 |
| Horizontal tail Aspect Ratio: $AR_{HT}$ [-] | 5.0 |
| Vertical tail Aspect Ratio: $AR_{VT}$ [-] | 5.0 |

## A.4. HFC 208 aircraft full inputs

The full list of inputs for the HFC 208 is shown in Tables A.13 to A.16.

Table A.5: Cessna 208 Customer Requirements

| Parameter | Value |
|---|---|
| Harmonic range: $R$ $[km]$ | 317.0 |
| Sustained turning speed: $V_{turn}$ $[m/s]$ | 75.0 |
| Climb speed: $V_{climb}$ $[m/s]$ | 70.0 |
| Takeoff speed: $V_{TO}$ $[m/s]$ | 40.0 |
| Cruise speed: $V_{cruise}$ $[m/s]$ | 95.5 |
| Sea Level rate of climb: $V_v$ $[m/s]$ | 6.27 |
| Service ceiling rate of climb: $V_{v_{ceiling}}$ $[m/s]$ | 0.51 |
| Stall speed: $V_{stall}$ $[m/s]$ | 31.4 |
| Maximum dive speed: $V_{dive}$ $[m/s]$ | 150.0 |
| Takeoff ground roll distance: $S_G$ $[m]$ | 626.0 |
| Service ceiling: $h_{ceiling}$ $[m]$ | 7620.0 |
| Cruise altitude: $h_{cruise}$ $[m]$ | 3000.0 |
| Design airfield altitude: $h_{TO}$ $[m]$ | 0.0 |
| Load factor/Sustained G's in turn: $n$ [-] | 1.41 |
| Number of passengers: $N_{pass}$ [-] | 10 |
| Payload mass: $m_{payload}$ $[kg]$ | 204.0 |
| Energy source oversizing factor: $C_{oversize}$ [-] | 4.5 |

Table A.6: Cessna 208 Assumptions

| Parameter | Value |
|---|---|
| **Minimum drag coefficient:** $C_{D_{min}}$ [-] | 0.0286 |
| Takeoff drag coefficient: $C_{D_{TO}}$ [-] | 0.05 |
| Takeoff lift coefficient: $C_{L_{TO}}$ [-] | 0.7 |
| Maximum lift coefficient: $C_{L_{max}}$ [-] | 2.2 |
| **Lift induced drag constant:** $k$ [-] | 0.0592 |
| Ground friction constant: $\mu$ [-] | 0.04 |
| **Lift to Drag ratio:** $L/D$ [-] | 10.86 |
| Passenger mass: $m_{pass}$ [kg] | 93.0 |
| Safety factor: $C_{safety}$ [-] | 1.5 |
| Reference empty mass fraction: $(OEM/MTOM)_{ref}$ [-] | 0.6 |

Table A.7: Cessna 208 Powertrain parameters

| Parameter | Value |
|---|---|
| Power generation specific power: $\hat{\rho}_{FC}$ $[W/kg]$ | 3000.0 |
| Power delivery specific power: $\hat{\rho}_{PMAD}$ $[W/kg]$ | 100000.0 |
| Power conversion specific power: $\hat{\rho}_{em}$ $[W/kg]$ | 100000.0 |
| Power generation efficiency: $\eta_{FC}$ [-] | 0.25 |
| Power delivery efficiency: $\eta_{PMAD}$ [-] | 0.95 |
| Power conversion efficiency: $\eta_{em}$ [-] | 0.95 |
| Energy source storage efficiency: $\eta_{storage}$ [-] | 0.95 |
| Energy source volumetric efficiency: $\eta_{volumetric}$ [-] | 0.95 |
| Energy source density: $\rho_{fuel}$ $[kg/m^3]$ | 800.0 |
| Specific energy: $LHV_{fuel}$ $[MJ/kg]$ | 43.0 |
| Propulsive efficiency: $\eta_{prop}$ [-] | 0.8 |
| Number of propellers: $N_{props}$ [-] | 1 |
| Propeller diameter: $D_{prop}$ $[m]$ | 3.0 |
| Powertrain operating temperature: $T_{oper}$ $[C]$ | 800.0 |
| Cooling thrust correction: $C_{coolthrust}$ [-] | 0.0 |
| Compressor specific power: $\hat{\rho}_{comp}$ $[W/kg]$ | 100000.0 |
| Compressor efficiency: $\eta_{comp}$ [-] | 1.0 |

Table A.8: Cessna 208 Aircraft Characteristics

| Parameter | Value |
|---|---|
| Wing aspect ratio: $AR_{wing}$ [-] | 9.7 |
| Sweep Quarter chord: $\Lambda_{C/4}$ [-] | 0.0 |
| Thickness to chord ratio: $t/c$ [-] | 0.2 |
| Taper Ratio: $\lambda$ [-] | 0.8 |
| Seats abreast: $N_{seat,abreast}$ [-] | 2 |
| Nose fineness ratio: $F_{nose}$ [-] | 1.5 |
| Tail fineness ratio: $F_{tail}$ [-] | 2.0 |
| Seat pitch: $l_{seat}$ [m] | 0.8 |
| Door length: $l_{door}$ [m] | 1.0 |
| Horizontal tail Aspect Ratio: $AR_{HT}$ [-] | 5.0 |
| Vertical tail Aspect Ratio: $AR_{VT}$ [-] | 5.0 |

Table A.9: Dornier Do 228 Customer Requirements

| Parameter | Value |
|---|---|
| Harmonic range: $R$ $[km]$ | 396.0 |
| Sustained turning speed: $V_{turn}$ $[m/s]$ | 77.2 |
| Climb speed: $V_{climb}$ $[m/s]$ | 77.2 |
| Takeoff speed: $V_{TO}$ $[m/s]$ | 45.0 |
| Cruise speed: $V_{cruise}$ $[m/s]$ | 114.7 |
| Sea Level rate of climb: $V_v$ $[m/s]$ | 8.0 |
| Service ceiling rate of climb: $V_{v_{ceiling}}$ $[m/s]$ | 0.51 |
| Stall speed: $V_{stall}$ $[m/s]$ | 38.1 |
| Maximum dive speed: $V_{dive}$ $[m/s]$ | 150.0 |
| Takeoff ground roll distance: $S_G$ $[m]$ | 792.0 |
| Service ceiling: $h_{ceiling}$ $[m]$ | 7620.0 |
| Cruise altitude: $h_{cruise}$ $[m]$ | 3000.0 |
| Design airfield altitude: $h_{TO}$ $[m]$ | 0.0 |
| Load factor/Sustained G's in turn: $n$ [-] | 1.41 |
| Number of passengers: $N_{pass}$ [-] | 18 |
| Payload mass: $m_{payload}$ $[kg]$ | 0 |
| Energy source oversizing factor: $C_{oversize}$ [-] | 5.0 |

Table A.10: Dornier Do 228 Assumptions

| Parameter | Value |
|---|---|
| **Minimum drag coefficient:** $C_{D_{min}}$ [-] | 0.0288 |
| Takeoff drag coefficient: $C_{D_{TO}}$ [-] | 0.05 |
| Takeoff lift coefficient: $C_{L_{TO}}$ [-] | 0.7 |
| Maximum lift coefficient: $C_{L_{max}}$ [-] | 2.2 |
| **Lift induced drag constant:** $k$ [-] | 0.0592 |
| Ground friction constant: $\mu$ [-] | 0.04 |
| **Lift to Drag ratio:** $L/D$ [-] | 10.98 |
| Passenger mass: $m_{pass}$ [kg] | 93.0 |
| Safety factor: $C_{safety}$ [-] | 1.5 |
| Reference empty mass fraction: $(OEM/MTOM)_{ref}$ [-] | 0.6 |

Table A.11: Dornier Do 228 Powertrain parameters

| Parameter | Value |
|---|---|
| Power generation specific power: $\hat{\rho}_{FC}$ $[W/kg]$ | 3000.0 |
| Power delivery specific power: $\hat{\rho}_{PMAD}$ $[W/kg]$ | 100000.0 |
| Power conversion specific power: $\hat{\rho}_{em}$ $[W/kg]$ | 100000.0 |
| Power generation efficiency: $\eta_{FC}$ [-] | 0.25 |
| Power delivery efficiency: $\eta_{PMAD}$ [-] | 0.95 |
| Power conversion efficiency: $\eta_{em}$ [-] | 0.95 |
| Energy source storage efficiency: $\eta_{storage}$ [-] | 0.95 |
| Energy source volumetric efficiency: $\eta_{volumetric}$ [-] | 0.95 |
| Energy source density: $\rho_{fuel}$ $[kg/m^3]$ | 800.0 |
| Specific energy: $LHV_{fuel}$ $[MJ/kg]$ | 43.0 |
| Propulsive efficiency: $\eta_{prop}$ [-] | 0.8 |
| Number of propellers: $N_{props}$ [-] | 2 |
| Propeller diameter: $D_{prop}$ $[m]$ | 4.0 |
| Powertrain operating temperature: $T_{oper}$ $[C]$ | 800.0 |
| Cooling thrust correction: $C_{coolthrust}$ [-] | 0.0 |
| Compressor specific power: $\hat{\rho}_{comp}$ $[W/kg]$ | 100000.0 |
| Compressor efficiency: $\eta_{comp}$ [-] | 1.0 |

Table A.12: Dornier Do 228 Aircraft Characteristics

| Parameter | Value |
|---|---|
| Wing aspect ratio: $AR_{wing}$ [-] | 9.0 |
| Sweep Quarter chord: $\Lambda_{C/4}$ [-] | 0.0 |
| Thickness to chord ratio: $t/c$ [-] | 0.2 |
| Taper Ratio: $\lambda$ [-] | 0.7 |
| Seats abreast: $N_{seat,abreast}$ [-] | 2 |
| Nose fineness ratio: $F_{nose}$ [-] | 1.0 |
| Tail fineness ratio: $F_{tail}$ [-] | 2.0 |
| Seat pitch: $l_{seat}$ [m] | 0.8 |
| Door length: $l_{door}$ [m] | 1.0 |
| Horizontal tail Aspect Ratio: $AR_{HT}$ [-] | 5.0 |
| Vertical tail Aspect Ratio: $AR_{VT}$ [-] | 5.0 |

Table A.13: HFC 208 Customer Requirements

| Parameter | Value |
|---|---|
| Harmonic range: $R$ $[km]$ | 317.0 |
| Sustained turning speed: $V_{turn}$ $[m/s]$ | 75.0 |
| Climb speed: $V_{climb}$ $[m/s]$ | 70.0 |
| Takeoff speed: $V_{TO}$ $[m/s]$ | 50.0 |
| Cruise speed: $V_{cruise}$ $[m/s]$ | 93.0 |
| Sea Level rate of climb: $V_v$ $[m/s]$ | 6.27 |
| Service ceiling rate of climb: $V_{v_{ceiling}}$ $[m/s]$ | 0.51 |
| Stall speed: $V_{stall}$ $[m/s]$ | 30.0 |
| Maximum dive speed: $V_{dive}$ $[m/s]$ | 150.0 |
| Takeoff ground roll distance: $S_G$ $[m]$ | 800.0 |
| Service ceiling: $h_{ceiling}$ $[m]$ | 7620.0 |
| Cruise altitude: $h_{cruise}$ $[m]$ | 3000.0 |
| Design airfield altitude: $h_{TO}$ $[m]$ | 0.0 |
| Load factor/Sustained G's in turn: $n$ [-] | 1.41 |
| Number of passengers: $N_{pass}$ [-] | 10 |
| Payload mass: $m_{payload}$ $[kg]$ | 300.0 |
| Energy source oversizing factor: $C_{oversize}$ [-] | 4.5 |

Table A.14: HFC 208 Assumptions

| Parameter | Value |
|---|---|
| **Minimum drag coefficient:** $C_{D_{min}}$ [-] | 0.028 |
| Takeoff drag coefficient: $C_{D_{TO}}$ [-] | 0.05 |
| Takeoff lift coefficient: $C_{L_{TO}}$ [-] | 0.7 |
| Maximum lift coefficient: $C_{L_{max}}$ [-] | 2.2 |
| **Lift induced drag constant:** $k$ [-] | 0.058 |
| Ground friction constant: $\mu$ [-] | 0.04 |
| **Lift to Drag ratio:** $L/D$ [-] | 12.38 |
| Passenger mass: $m_{pass}$ [kg] | 93 |
| Safety factor: $C_{safety}$ [-] | 1.5 |
| Reference empty mass fraction: $(OEM/MTOM)_{ref}$ [-] | 0.6 |

Table A.15: HFC 208 Powertrain parameters

| Parameter | Value |
|---|---|
| Power generation specific power: $\hat{\rho}_{FC}$ $[W/kg]$ | 2000.0 |
| Power delivery specific power: $\hat{\rho}_{PMAD}$ $[W/kg]$ | 10000.0 |
| Power conversion specific power: $\hat{\rho}_{em}$ $[W/kg]$ | 5000.0 |
| Power generation efficiency: $\eta_{FC}$ [-] | 0.5 |
| Power delivery efficiency: $\eta_{PMAD}$ [-] | 0.9 |
| Power conversion efficiency: $\eta_{em}$ [-] | 0.9 |
| Energy source storage efficiency: $\eta_{storage}$ [-] | 0.2 |
| Energy source volumetric efficiency: $\eta_{volumetric}$ [-] | 0.5 |
| Energy source density: $\rho_{fuel}$ $[kg/m^3]$ | 70.0 |
| Specific energy: $LHV_{fuel}$ $[MJ/kg]$ | 120.0 |
| Propulsive efficiency: $\eta_{prop}$ [-] | 0.8 |
| Number of propellers: $N_{props}$ [-] | 1 |
| Propeller diameter: $D_{prop}$ $[m]$ | 3.0 |
| Powertrain operating temperature: $T_{oper}$ $[C]$ | 80.0 |
| Cooling thrust correction: $C_{coolthrust}$ [-] | 0.0 |
| Compressor specific power: $\hat{\rho}_{comp}$ $[W/kg]$ | 2000.0 |
| Compressor efficiency: $\eta_{comp}$ [-] | 0.7 |

Table A.16: HFC 208 Aircraft Characteristics

| **Parameter** | **Value** |
|---|---|
| Wing aspect ratio: $AR_{wing}$ [-] | 9.7 |
| Sweep Quarter chord: $\Lambda_{C/4}$ [-] | 0.0 |
| Thickness to chord ratio: $t/c$ [-] | 0.2 |
| Taper Ratio: $\lambda$ [-] | 0.8 |
| Seats abreast: $N_{seat,abreast}$ [-] | 2 |
| Nose fineness ratio: $F_{nose}$ [-] | 1.5 |
| Tail fineness ratio: $F_{tail}$ [-] | 2.0 |
| Seat pitch: $l_{seat}$ [m] | 0.8 |
| Door length: $l_{door}$ [m] | 1.0 |
| Horizontal tail Aspect Ratio: $AR_{HT}$ [-] | 5.0 |
| Vertical tail Aspect Ratio: $AR_{VT}$ [-] | 5.0 |